FEDERAL UNIVERSITY OF RIO GRANDE DO SUL BRAZIL

POSTGRADUATE PROGRAM IN PHYSICS

DOCTORAL THESIS

Metal (Zn and W) doped $BiVO_4$ decorated with $FeMnO_x$ and $FeNiO_x$ cocatalysts for photocatalytic applications

Author

Niqab Khan

Supervisor: Prof. Sherdil Khan

Co-Supervisor: Prof. Renato Vitalino Gonçalves

September 2023

UNIVERSIDADE FEDERAL DO RIO GRANDE DO SUL BRASIL

PROGRAMA DE PÓS-GRADUAÇÃO EM FÍSICA

TESE DE DOUTORADO

$BiVO_4$ dopado com metal (Zn e W) decorado com cocatalisadores $FeMnO_x$ e $FeNiO_x$ para aplicações fotocatalíticas

Autor

Niqab Khan

Orientador: Prof. Sherdil Khan

Co- Orientador: Prof. Renato Vitalino Gonçalves

Septembro de 2023

STATEMENT OF ORIGINALITY

I hereby declare that the work presented in this thesis entitled **"Metal (Zn and W) doped $BiVO_4$ decorated with $FeMnO_x$ and $FeNiO_x$ cocatalysts for photocatalytic applications"** submitted, to the department of physics, UFRGS, for the award of Ph.D degree in the field of Physics, is a record of original work performed by me with sources and complete references under the supervision of **Prof.Sherdil Khan** (institute of physics UFRS) and Co-supervisors **Prof. Renato Vitalino Gonçalves** (institute of physics USP). Furthermore, this work has not been previously carried out by others for the award of a degree/fellowship.

NIQAB KHAN

ACKNOWLEDGMENT

I would like to convey my sincere gratitude to my supervisor **Dr. Sherdil Khan,** and co-supervisor **Dr. Renato Vitalino Gonçalves** for their devoted supervision, sympathetic attitude, enormous support, and help throughout my research work. They are a source of great motivation and encouragement to me.

I am also thankful to the national center for the scientific and technological development Brazil CNPq, CAPES, FAPERGS, FAPESP, and institute of Physics UFRGS for the financial support.

I express my sincere salutations to all members of the Laboratory of the Artificial Photosynthesis and Renewable Energy (NanoREAP), Department and Institute of Physics UFRGS and Laboratory of the Artificial Photosynthesis & Nanomaterials (LAPNANO), Department and Institute of Physics Sao Carlos, USP, for helping me in the experimental work.

Last but not least, I express my very special thanks to my family members and my friends for their constant support and encouragement.

Above All, I am thankful to the **ALMIGHTY ALLAH**, who gave me strength to complete this research study.

NIQAB KHAN

CONTENTS

Chapter 01

1.1 General Context 16

1.2 Photocatalysis 17

1.2.1 Photoelectrochemical (PEC) water splitting 18

1.2.2 Photocatalytic Water Splitting 20

1.3 Choice of Photocatalysts 21

1.4 Bismuth Vanadate ($BiVO_4$) 23

1.4.1 Historical Background of $BiVO_4$ 23

1.4.2 Crystal Polytypes and Optical Properties 24

1.4.3 Electronic Structure of $BiVO_4$ 25

1.4.4 Limitations of the monoclinic $BiVO_4$ 26

1.4.5 Photocatalytic process in the perspective of metal-doped $BiVO_4$ 27

1.4.6 Substitutional/ interstitial doping 28

1.4.7 Heterojunction 30

1.4.8 Bimetallic Cocatalysts Loading 32

1.5 Research Objectives 35

2.1 Materials and Methods 37

2.1.1 Chemicals 37

2.2 Hydrothermal Synthesis 37

2.2.1 Preparation of pure bismuth vanadate ($BiVO_4$) powder via hydrothermal technique 37

2.2.2 Preparation of tungsten (W) and zinc (Zn) doped bismuth vanadate ($BiVO_4$) powder via hydrothermal technique. 38

2.2.3 Loading of $FeMnO_x$ and $FeNiO_x$ bimetallic cocatalysts on pure BVO, 2% tungsten (W), and 2% zinc (Zn) doped bismuth vanadate ($BiVO_4$) powder via RF magnetron sputtering. 39

2.3 Synthesis of films 41

2.3.1 Cleaning of FTO 41

2.3.2 Synthesis of W:BVO, W:BVO/$FeNiO_x$ and W:BVO/$FeMnO_x$ films 41

2.3.3 Synthesis of pure $FeNiO_x$ and $FeMnO_x$ films 42

2.4 Characterization 42

2.4.1 X-ray Diffraction (XRD) of Powder Samples 42

2.4.2 Scanning Electron Microscopy (SEM) 43
2.4.3 Ultraviolet-Visible (UV-vis) Spectroscopy 43
2.4.4 Brunner–Emmett–Teller (BET) analysis 43
2.4.5 Raman Spectroscopy 43
2.4.6 X-ray Photoelectron Spectroscopy (XPS) 44
2.4.7 Transmission Electron Microscopy (TEM) 44
2.5 Gas chromatography 47
2.6 Photocatalytic Oxygen Evolution 47
2.7 Mott- Schottky analysis 48
2.8 Band Bending Model for p-n Heterojunction 49
2.9 Computational details 51
3.1 X-ray diffraction (XRD) pattern of Powder Samples 52
3.1.1 X-ray diffraction (XRD) pattern of W-doped $BiVO_4$ 52
3.1.2 X-ray diffraction (XRD) pattern of pure $BiVO_4$ loaded with $FeMnO_x$ and $FeNiO_x$ cocatalysts 54
3.1.3 X-ray diffraction (XRD) pattern of 2% tungsten (W) $BiVO_4$ loaded with $FeMnO_x$ and $FeNiO_x$ cocatalysts 55
3.2 Raman spectroscopy 56
3.2.1 Raman spectroscopy of W-doped $BiVO_4$ 57
3.2.2 Raman spectroscopy of pure $BiVO_4$ loaded with $FeMnO_x$ and $FeNiO_x$ cocatalysts 58
3.2.3 Raman spectroscopy of 2%W-doped $BiVO_4$ loaded with $FeMnO_x$ and $FeNiO_x$ cocatalysts 59
3.3 Scanning electron microscopy (SEM) of pure and W-doped $BiVO_4$ 60
3.3.1 Scanning electron microscopy (SEM) of pure and 2% W-doped $BiVO_4$ loaded with $FeMnO_x$ and $FeNiO_x$ cocatalysts. 62
3.4 UV-vis diffuse reflectance spectra 63
3.4.1 UV-vis diffuse reflectance spectra of W-doped $BiVO_4$ 63
3.4.2 UV-vis diffuse reflectance spectra of pure and W-doped $BiVO_4$ loaded with $FeMnO_x$ and $FeNiO_x$ cocatalysts 64
3.5 X-ray photoelectron spectroscopy (XPS) of pure and W-doped $BiVO_4$ 65
3.5.1 X-ray photoelectron spectroscopy of 2 %W-doped $BiVO_4$ loaded with $FeMnO_x$ and $FeNiO_x$ cocatalysts. 69
3.6 High resolution transmission electron microscopy (HRTEM) of the W-doped BiVO4 loaded with FeMnOx 71

3.7 Atomic Absorption Spectrometry (FAAS) and Graphite Furnace Atomic Absorption Spectrometry (GFAAS) 73

3.8 Photocatalytic oxygen evolution 73

3.9 Band alignment and charge transport properties. 77

4.1 X-ray diffraction pattern of pure and Zn-doped $BiVO_4$ 83

4.1.1 X-ray diffraction pattern of Zn-doped $BiVO_4$ loaded with $FeMnO_x$ and $FeNiO_x$ cocatalysts 85

4.2 Raman spectroscopy of pure, 1%, 2%, and 3%Zn doped $BiVO_4$, and 2%Zn doped $BiVO_4$ loaded with $FeMnO_x$ and $FeNiO_x$ 85

4.3 Ultraviolet-visible (UV-vis) spectroscopy 87

4.5 Scanning electron microscopy (SEM) 89

4.6 X-ray photoelectron spectroscopy (XPS) of Zn-doped $BiVO_4$ 90

4.6.1 X-ray photoelectron spectroscopy (XPS) of Zn doped $BiVO_4$ loaded with $FeMnO_x$ cocatalyst 92

4.7 High Resolution Transmission Electron Microscopy (HRTEM) 93

4.8 Photocatalytic Oxygen (O_2) Evolution 95

5.1 Conclusion 101

5.2 Future Recommendations 102

References 104

LIST OF FIGURES

Figure 1. 1 Steps involved in the photocatalysis reaction process [15]. 18
Figure 1. 2 Scheme showing the photoelectrochemical water splitting reactions and electron flow [22]. 20
Figure 1. 3. Solar hydrogen and oxygen production from water using powder photocatalyst..... 21
Figure 1. 4.Representing the relationship of band structure and redox potential of different photocatalytic semiconductors [31]..... 22
Figure 1.5. Crystal structure of $BiVO_4$: (a) Pucherite, (b) tetragonal zircon, (c) monoclinic scheelite [3], (d) band structures of monoclinic scheelite and tetragonal zircon $BiVO_4$ [7] and ,(e) absorption of monoclinic $BiVO_4$ [51]..... 25
Figure 1. 6. XRD pattern of tetragonal, and monoclinic $BiVO_4$ [52]..... 26
Figure 1.7 Scheme diagram showing the band structure and optical curves of (a) pure semiconductor, (b) doping-induced shallow-level and deep-level states and (c) induced band gap narrowing [72]. 29
Figure 1.8. Band alignment in type-I, type-II, and type-III heterojunctions..... 31
Figure 1.9. Schematic diagram, representing $BiVO_4$ photocatalyst loaded with bimetallic cocatalysts. ... 35

Figure 2. 1. Schematic diagram, representing different steps involved in the hydrothermal synthesis process. 38
Figure 2. 2. Schematic diagram, representing hydrothermal synthesis process of W and Zn doped $BiVO_4$. 39
Figure 2. 3. RF magnetron sputtering deposition setup for powder and films: (1) Spray deposition system, (2) deposition gun, (3) high vacuum camera, (4) mechanical pump, (5) turbo molecular vacuum pump, and (6) control system..... 40
Figure 2. 4. Synthesis process of W:BVO, W:BVO/$FeNiO_x$ and W:BVO/$FeMnO_x$ films..... 41
Figure 2. 5. Sample preparation map, showing different steps involve in the synthesis process..... 42
Figure 2. 6. Flame Atomic Absorption Spectrometry..... 45
Figure 2. 7. Graphite Furnace Atomic Absorption Spectrometry. 46
Figure 2. 8. Gas chromatograph (GC) equipped with thermal conductivity detector. 47
Figure 2. 9. Photocatalytic oxygen evolution, irradiating the sample with 300 W Xe lamp with an AM 1.5 G filter..... 48

Figure 3. 1. XRD pattern of all $BiVO_4$ powder samples doped with 1%, 2%, and 3% tungsten (W) showing a trend towards 040 direction. 52
Figure 3. 2. XRD pattern of all $BiVO_4$ powder samples doped with 2%, tungsten (W) showing a shift toward lower angle..... 53
Figure 3. 3. XRD pattern of $BiVO_4$ loaded with cocatalysts i.e. (a) $FeMnO_x$ and (b) $FeNiO_x$ via RF magnetron sputtering deposition for 5,10, and 20 min. 55
Figure 3. 4 XRD pattern of 2% tungsten (W) doped $BiVO_4$ loaded with $FeMnO_x$ and $FeNiO_x$ cocatalysts via RF magnetron sputtering deposition for 10 min. 56
Figure 3. 5. Raman spectra of all $BiVO_4$ powder samples doped with 1%, 2%, and 3% tungsten (W). ... 57
Figure 3. 6. Raman spectra of all $BiVO_4$ powder samples loaded with $FeMnO_x$ and $FeNiO_x$. 58

Figure 3. 7. Raman spectra of W-doped $BiVO_4$ powder samples loaded with $FeMnO_x$ and $FeNiO_x$. 59
Figure 3. 8. Scanning electron microscopy images of (a) pure (b) 1%W (c) 2%W, and (d) 3%W doped $BiVO_4$, representing different morphology with reduced particle sizes. The inset in Figure 1a and 1b displays the high resolution SEM images of BVO and W:BVO, respectively. 60
Figure 3. 9. Elemental mapping of W-doped $BiVO_4$, showing uniform distribution of Bi, V, O, and tungsten (W). 61
Figure 3. 10. EDS of 2% W doped $BiVO_4$ showing Bi, V, and W peaks. 61
Figure 3. 11. Scanning electron microscopy images of the (a) pure BVO loaded with $FeMnO_x$ (b) 2%W doped BVO loaded with $FeMnO_x$, (c) pure loaded with $FeNiO_x$, and (d) 2%W doped BVO loaded with $FeNiO_x$ cocatalysts. 62
Figure 3. 12. (a) UV-vis diffuse reflectance spectra and (b) Bandgap energies of 1%W, 2%W, and 3%W doped $BiVO_4$ powder sample is compared to pure $BiVO_4$, which were obtained using the Kubelka-Munk transformation of defused reflectance spectra of the samples. The reflectance spectra of the W doped $BiVO_4$ samples correspond to higher wavelengths which leads to the redshift in the band gap energies. . 63
Figure 3. 13. UV-vis diffuse reflectance spectra of pure and W-doped $BiVO_4$ loaded with $FeMnO_x$ and $FeNiO_x$ cocatalysts via sputtering deposition for 10 min, where cocatalysts deposit on pure $BiVO_4$ shows no change in the reflectance spectra and for the W doped $BiVO_4$ reflectance correspond to higher wavelengths which is because of the W dopants. 64
Figure 3. 14. XPS survey spectra of 1%, 2 %, and 3% W doped $BiVO_4$ and 2% W doped $BiVO_4$ loaded with $FeMnO_x$ and $FeNiO_x$ cocatalysts. 66
Figure 3. 15. XPS spectra of tungsten 1%W,2%W, and 3%W doped BVO samples compared to pure BVO, representing a shift towards higher binding energies (a) Bi4f (b) V2p, (c) O1s, and (d) tungsten (W) peaks intensity increased with concentration. 68
Figure 3. 16. XPS spectra of W:BVO loaded with $FeMnO_x$ and $FeNiO_x$ cocatalysts, representing a shift in B.E towards lower values for (a) Bi4f, (b) O1s, and (c) V2p. 70
Figure 3. 17. XPS plots represent different Fe, Mn, and Ni peaks for the deposition of $FeMnO_x$ and $FeNiO_x$ cocatalysts on Si substrate. 71
Figure 3. 18. (a) HRTEM image of the edge of W:BVO nanoparticle with the corresponding FFT inset, (b) HAADF (high angle annular dark field) image of the edges of three W:BVO nanoparticles and correspondent , and (c) EDS map , representing Bi, V, O, W, Fe, Mn, where Fe, and Mn have particle size of 5 nm. 72
Figure 3. 19. Photocatalytic O_2 evolution test of (a) Pure and W (1%, 2%, and 3%) doped $BiVO_4$ (b) $FeNiO_x$ cocatalysts loaded on pure BVO, (c) $FeMnO_x$ cocatalysts loaded on pure BVO, (d) $FeMnO_x$, and $FeNiO_x$ cocatalysts loaded on tungsten doped BVO (W:BVO), over 3 h exposure to 300 W Xe lamp with an AM 1.5 G filter. 75
Figure 3. 20. Recycling test of the W:BVO/$FeMnO_x$ over four cycles (each cycle 3 h) exposure to 300 W Xe lamp with an AM 1.5 G filter for four cycles. 76
Figure 3. 21 Mott-Schottky curves for (a) n-type W:BVO film, (b) p-type $FeNiO_x$ film, and (c) p-type $FeMnO_x$ film; (d) energy band diagrams for pure W:BVO, $FeNiO_x$, and $FeMnO_x$ semiconductors; and (e) Mott-Schottky curves for the W:BVO/$FeNiO_x$ and W:BVO/$FeMnO_x$ 78
Figure 3. 22. (Direct) optical bandgap energy for pure (a) $FeNiO_x$ and (b) $FeMnO_x$ films. 80
Figure 3. 23. Interfacial band alignment for the (a) W:BVO/$FeNiO_x$ and (b) W:BVO/$FeMnO_x$ heterojunctions. 82

Figure 4. 1. XRD pattern of (a) pure BVO and Zn doped (1%, 2%, and 3%) BVO and (b) Zn doped BVO loaded with $FeMnO_x$ and $FeNiO_x$ cocatalysts. 83
Figure 4. 2. XRD pattern of 2% Zn doping to V and Bi sites respectively; resulting in improved crystallinity. 84
Figure 4. 3. (a) Raman spectra of pure and Zn (1%, 2%, & 3%) doped $BiVO_4$, (b) corresponding Raman shift, and (c) Raman spectra of Zn doped BVO with cocatalysts. 86
Figure 4. 4. UV-vis diffuse reflectance spectra of (a) Zn-doped $BiVO_4$, and (b) Zn-doped $BiVO_4$ loaded with $FeMnO_x$ and $FeNiO_x$ cocatalysts. 88
Figure 4. 5. BET surface area of the pristine compared to 2% Zn doped $BiVO_4$, where the Zn doped displays a high surface area than pristine..... 89
Figure 4. 6. SEM images of (a) pure, (b) 1% Zn-doped $BiVO_4$, (c) 2% Zn-doped $BiVO_4$, and (d) 3% Zn-doped $BiVO_4$. 90
Figure 4. 7. XPS survey spectra of 1%, 2%, and 3% Zn doped $BiVO_4$ 91
Figure 4. 8. XPS plot of (a) Bi, (b) V, (c) Zn, and (d) O1s for pure and 1%, 2%, and 3% Zn doped $BiVO_4$, representing a shift towards lower binding energies. 92
Figure 4. 9. XPS spectra of Zn doped $BiVO_4$ loaded with $FeMnO_x$ (a) Bi, (b) V, and (c) O1s, showing a shift towards higher binding energies with respect to 2 % Zn doped $BiVO_4$. 93
Figure 4. 10. TEM image of pure $BiVO_4$ (a), HRTEM image of $BiVO_4$ (b), Zn:$BiVO_4$ (c) and the insets corresponding the SAED patterns of the characteristic monoclinic $BiVO_4$ structure of the [112] planes. HRTEM image of Zn:$BiVO_4$/$FeMnO_x$ (d) and the insets show the area of FFT pattern indicates the [004] plane of the $FeMnO_3$. HAADF-STEM image (e) and the corresponding EDS mapping of the Zn:$BiVO_4$/$FeMnO_x$ sample (f-h). 94
Figure 4. 11. Oxygen evolution of (a) pure Zn-doped $BiVO_4$, and (b) the Zn-doped $BiVO_4$ loaded with $FeMnO_x$ and $FeNiO_x$ cocatalysts. The 2%Zn doped $BiVO_4$ loaded with $FeMnO_x$ (Zn:BVO/$FeMnO_x$) showing higher oxygen evolution than the rest of samples. 96
Figure 4. 12 (a) Band structure of pure $BiVO_4$ showing indirect band gap at X and R high symmetry points (b) band structure of Zn doped $BiVO_4$ reveals a direct band gap at X, (c) PDOS of pure $BiVO_4$, (d) PDOS of Zn $BiVO_4$. 97
Figure 4. 13. Total density of states (TDOS) of BVO, Zn:BVO, and Zn:BVO/$FeMnO_x$. 98
Figure 4. 14. (a) Before the adsorption of $FeMnO_x$ on Zn doped $BiVO_4$, and (b) after the adsorption of $FeMnO_x$ on Zn doped $BiVO_4$ 99
Figure 4. 15. Electron localization function (ELF) for (a) pure, (b) Zn doped $BiVO_4$, and (c) Zn doped $BiVO_4$ loaded with $FeMnO_x$ cocatalysts 100

LIST OF TABLES

Table 1.1. Several $BiVO_4$ photocatalysts in the form of powder for photocatalytic oxygen evolution……....29

Table 3.1. Crystalline (based on XRD analyses) and morphological (based on SEM images) properties of pure $BiVO_4$ and W-doped $BiVO_4$. ……54

Table 3.2. Crystalline (based on XRD analyses) and morphological (based on SEM images) properties of W-doped $BiVO_4$ loaded with FeMnOx and $FeNiO_x$ cocatalysts……....55

Table 3.3. Raman shift, bond length, and bandgap based on Raman and UV-vis analysis……...57

Table 3.4. Photocatalytic oxygen evolution, irradiated with visible light with 1.5G filter for 3 hours……...74

Table 4.1. Crystalline (based on XRD analyses) and morphological (based on SEM images) properties of pure $BiVO_4$ and Zn-doped $BiVO_4$……....84

Table 4.2. Raman shift, bond length, and bandgap based on Raman and UV-vis analysis……..86

Table 4.3. Photocatalytic oxygen evolution, irradiated with visible light with AM 1.5 G filter for 3 hours.....95

ABBREVIATIONS

Acronym	Definition of Acronym
Ar	Argon
Au	Gold
Bi	Bismuth
$Bi(NO_3)_3.5H_2O$	Bismuth nitrate penda hydrate
$Bi2O_3$	Bismuth oxide
BiOI	Bismuth oxyiodide
$BiVO_4$	Bismuth vanadate
RF	Radio Frequency
VB	Valence band
CB	Conduction band
m-s	Monoclinic scheelite
CdS	Cadmium sulfide
CO_2	Carbon dioxide
Cu	Copper
W	Tungsten
Zn	Zinc
D	Crystallite size
DFT	Density functional theory
EDAX	Energy dispersive analysis of X-rays
Eg	Band gap
TEM	Transmission electron microscopy
eV	Electron volt
Fe_2O_3	Ferric oxide
FE-SEM	Filed emission scanning electron microscopy
FFT	Fast Fourier Transform
FT-IR	Fourier transform infrared
FWHM	Full width half maximum
GaAs	Gallium arsenide

h	Hour
HNO_3	Nitric acid
HR-TEM	High resolution transmission electron microscopy
XRD	X-ray diffraction
JCPDS	Joint committee on powder diffraction standards
MB	Methylene blue
MO	Methyl orange
N	Nitrogen
NH_4VO_3	Ammonium metavanadate
nm	Nanometer
NP	Nanoparticles
^oC	Degree celcius
Pt	Platinum
TiO_2	Titanium oxide
PEC	Photoelectrochemical
UV-VIS	Ultraviolet visible
V	Vanadium
V_2O_5	Vanadium oxide
VBM	Valence band maximum
VO_4	Vanadate
ZnO	Zinc oxide
BVO	Bismuth vanadate
O_V	Oxygen vacancies
μmol	Micromol

Abstract

Bismuth vanadate ($BiVO_4$) has been considered as an efficient photocatalysts for water splitting in both photocatalytic and photoelectrochemical process, but still the as prepared $BiVO_4$ suffers high charge recombination and low charge transfer efficiency. The efficient photogenerated charge transfer at solid-liquid interface for improving the photoactivity is a key to the device performance for solar energy applications. The metallic dopants and loading co-catalysts are potential processes to suppress the electron-hole recombination. Particularly, site selective co-catalysts have a strong potential to scavenge the holes from $BiVO_4$ surface. However, uniform incorporation of the co-catalyst on the semiconductor surface is also challenging. This study describes simple one step RF-magnetron sputtering deposition of new bimetallic p-type $FeMnO_x$ and $FeNiO_x$ hole selective cocatalysts over the as prepared, Zn and W doped $BiVO_4$. The loading of bimetallic co-catalysts over as prepared, Zn and W doped $BiVO_4$ have shown a remarkable improvement in photocatalytic O_2 evolution. The photocatalytic O_2 evolution of the Zn and W doped $BiVO_4$ samples increased as compared to the pristine $BiVO_4$ (93 μmol), where for the Zn doped $BiVO_4$, the oxygen evolution was enhanced to 134 μmol while for W doped $BiVO_4$ it was boosted to 160 μmol under solar irradiation condition (1.5 G) for 3 h. Loading $FeMnO_x$ and $FeNiO_x$ cocatalysts over Zn and W doped $BiVO_4$ further enhanced the photocatalytic activity to 181 μmol for W doped $BiVO_4$ loaded with $FeMnO_x$. The $FeMnO_x$ and $FeNiO_x$ bimetallic cocatalysts are p-type in nature, combining with n-type $BiVO_4$ making a p-n junction. Formation of p-n junction is a key to improve the charge transfer and suppress the charge recombination. Our study offers a facile way to boost the photocatalytic activity of $BiVO_4$ by loading a bimetallic cocatalysts via magnetron sputtering as a hole scavenger which can be applied to many other materials for energy applications.

Keywords: Hydrothermal synthesis, metal (Zn and W), $BiVO_4$, photocatalysis, $FeMnO_x$ and $FeNiO_x$ cocatalysts RF-magnetron sputtering, and oxygen evolution.

Resumo

O vanadato de bismuto ($BiVO_4$) tem sido considerado um fotocatalisador eficiente na quebra da molécula de água em processos fotocatalíticos e fotoeletroquímicos, mas, ainda assim, amostras desse material em sua forma pura demonstram alta recombinação de carga e baixa eficiência na transferência de carga. Um transporte de cargas fotogeradas eficiente na interface sólido-líquido, que resulta em uma maior fotoatividade, é crucial para o desempenho do dispositivo para aplicações em energia solar. A adição de dopantes metálicos e co-catalisadores são processos com potencial de suprimir a recombinação elétron-buraco. Particularmente, os co-catalisadores seletivos ao sítio ativo têm um grande potencial para suprimir os buracos da superfície do $BiVO_4$. No entanto, a incorporação uniforme do cocatalisador na superfície do semicondutor também é desafiadora. Este estudo demonstra a deposição em uma etapa dos co-catalisadores bimetálicos seletivos do tipo *p* $FeMnO_x$ e $FeNiO_x$ pela técnica de *RF-magnetron sputtering* sobre o $BiVO_4$ dopado com Zn e W. A adição dos co-catalisadores sobre o $BiVO_4$ dopado resultou em um notável aumento na evolução fotocatalítica de O_2. A evolução fotocatalítica de O_2 das amostras de $BiVO_4$ dopadas com Zn e W aumentou em comparação ao $BiVO_4$ puro (93 μmol), sendo para o $BiVO_4$ dopado com Zn de 134 μmol, enquanto para o $BiVO_4$ dopado com W de 160 μmol, sob condições de irradiação solar (1.5 G) pelo período de 3 h. A adição dos co-catalisadores de $FeMnO_x$ e $FeNiO_x$ sobre o $BiVO_4$ dopado com Zn e W aumentou ainda mais a atividade fotocatalítica, sendo de 181 μmol para $BiVO_4$ dopado com W com adição de $FeMnO_x$. A natureza do tipo p dos co-catalisadores bimetálicos $FeMnO_x$ e $FeNiO_x$ combinadas com o $BiVO_4$, um material do tipo n, formam uma junção p-n, que é considerada importante para uma melhor transferência de carga e supressão da recombinação de carga. Este estudo oferece uma maneira fácil de aumentar a atividade fotocatalítica do $BiVO_4$ pela adição de co-catalisadores bimetálicos depositados por *RF-magnetron sputtering* que atuam como supressores de buracos da estrutura de bandas, e que pode ser aplicado a muitos outros materiais para aplicações de energia.

Palavras-chave: Síntese hidrotermal, metal (Zn e W), $BiVO_4$, fotocatálise, co-catalisadores $FeMnO_x$ e $FeNiO_x$, *RF-magnetron sputtering*, evolução de oxigênio.

Chapter 1

Introduction

1.1 General Context

The energy crisis and environmental pollution are the main challenges worldwide. The world is mostly dependent on energy from fossil fuels. People across the globe consume approximately 80 % of their energy from fossil fuels and the burning of fossil fuels emits CO_2 gas into the environment which leads to serious environmental issues like the greenhouse effect [1,2]. According to the Intergovernmental Panel on Climate Change (IPCC) prediction, the average CO_2 emission will rise to 590 ppm by the year 2100 which may lead to a rise in the average temperature of the earth by 1.9 °C and affect the world badly by increasing sea level, frequent drought, heavy rain, and storm [3–5]. Therefore, environmentally friendly and alternative energy sources are highly desirable.

Solar energy conversion into other forms like hydrogen energy is a promising pathway for a sustainable future. Solar energy is one of the richest natural sources of energy available on Earth. The energy consumed by humans in a year is less than the solar energy striking the earth's surface in one hour [6]. Therefore, it is important to develop photocatalysts that can directly convert solar energy into another form of energy. So far, many photocatalytic semiconducting materials such as metal oxides, ternary oxides, nitrides, halides, and sulfides have been developed due to their extraordinary photocatalytic activity and non-toxicity. Among these photocatalysts, monoclinic scheelite bismuth vanadate (m-s $BiVO_4$) is of great importance due to its outstanding properties, such as low band gap (~2.4 eV), maximum photocurrent density of 7.5 mA/cm^2, about 9% solar-to-hydrogen efficiency, excellent dispersion, a non-toxic, highly resistant to corrosion under visible light illumination, and photocatalytic activity. However, the pure m-s $BiVO_4$ presents some drawbacks such as low electron mobility, high charge recombination, slow water oxidation, and short hole diffusion length. Many strategies have been adapted to improve sluggish charge kinetics such as morphological control, doping, heterojunction, and cocatalyst deposition [7].

In this work, we adopted doping and cocatalyst deposition strategies to improve the slow charge dynamics of m-s $BiVO_4$. Tungsten (W) and zinc (Zn) were used as dopants because they have shown greater improvement in photocatalytic activity based on previous literature. W^{6+} has a

higher oxidation number while Zn^{2+} has lower oxidation number. Therefore V^{5+} substituents with high and low oxidation states contribute differently to the $BiVO_4$ structure, where W^{6+} forms a sub-energy level at the top of the conduction (C.B) band while Zn^{2+} forms a sub-energy level at the top of the valence band (V.B) [8]. In both cases, the dopants reduce the band gap, and enhance the visible light absorption. Thus, leading to suppression of charge recombination and enhancement of the photocatalytic activity of $BiVO_4$. Furthermore, for the first time we have deposited *p*-type $FeMnO_x$ and $FeNiO_x$ cocatalysts on pure and W and Zn doped $BiVO_4$ powder using RF-magnetron sputtering. *P*-type cocatalysts combine with *n*-type $BiVO_4$ form a p-n junction that provides an additional built-in electric field, active sites and enhances stability to further promote photocatalytic activity.

1.2 Photocatalysis

Photocatalysis has received considerable attention in the last two decades for environmental applications. Photocatalysis is a low cost approach that utilizes solid-liquid interface to harvest energy under sunlight irradiation. The working principle of photocatalysis is based on the direct use of sunlight and its conversion into another form of energy [9–11]. In a homogenous system, a photocatalytic process involves the generation, migration, and separation of electron-hole pairs. Major applications of photocatalysis are photocatalytic (PC) or photoelectrochemical (PEC) water splitting, and environmental remediation known as photodegradation. [12]. The first application is related to water splitting which is a non-toxic and environmentally friendly method to split water into hydrogen and oxygen [12]. The second application is related to environmental remediation, which is also known as an advanced oxidation process for cleaning water, oil, and soil [13].

The working principle of photocatalysis may be described completely in four steps as shown in Figure 1.1: (1) absorption of incoming light to produce electron-hole pairs when its energy is equal or greater than the bandgap energy of the photocatalysts; (2) separation of excited electron-hole; (3) transfer of charges (electron-hole) to the surface of photocatalysts; and (4) redox surface reaction by electron-hole. In the third step, a large portion of electron-hole pairs recombine on the surface site. The recombination of electron-hole pairs dissipates energy in the form of heat or light emission and the long-lived photogenerated charges have the potential to participate in the surface redox reaction which depends on the donor and the accepter properties of the surface adsorbed species [14].

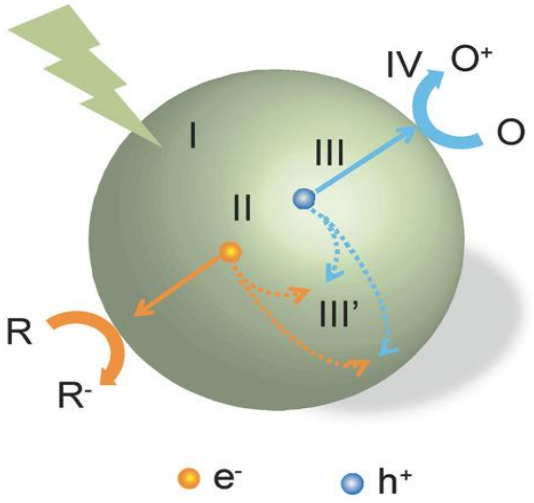

Figure 1. 1 Steps involved in the photocatalysis reaction process [15].

1.2.1 Photoelectrochemical (PEC) water splitting

Photoelectrochemical (PEC) is a form of artificial photosynthesis, which was first studied by Fujishima and Honda when they used TiO_2 as a photocatalyst under UV illumination [16]. It is an alternative way that directly produces hydrogen and oxygen (solar fuels) from water under solar light illumination. The PEC process often uses photoanodes to convert solar energy to chemical energy, thus enabling abundant solar energy to be stored, and converted to other forms. Additionally, PEC provides a zero-emission pathway for hydrogen production and involves two kinds of reaction i.e. oxygen evolution reaction (OER) and hydrogen evolution reaction (HER). OER takes place at the photoelectrode while HER is at the counter electrode [17]. Three types of arrangements of the photoelectrodes exist in photoelectrochemical setup i.e. photo-anode made of *n*-type semiconductor and metal cathode, photocathode made of *p*-type semiconductor and photo-anode made of *n*-type semiconductor, and photo-cathode made of *p*-type semiconductor and photo-anode made of metal. There are several requirements to split water efficiently into hydrogen and oxygen: (1) appropriate band alignment and the photovoltage generated by photoelectrode > 1.23 V, (2) absorption of a large portion of the visible light spectrum, (3) charge transport between the electrolyte solution and semiconductor [18]. The bottleneck of this process lies in the water oxidation half reaction (Equation 1-3), which produces oxygen. In other words, the OER reaction is a complex proton-coupled process that involves four electrons and four protons, with slow

kinetics in the cleavage of four O-H bonds and formation of two O-O bonds [19]. On the other hand, HER could occur easily due to the hydrogen (H) production by direct H-H association. Photocatalytic water splitting reactions are given below, where the overall photocatalytic reaction can be expressed as:

$$2H_2O \rightarrow 2H_2 + O_2 \quad (1)$$

Which can be considered as two half reaction equation 1 and equation 2:

$$4H^+ + 4e^- \rightarrow 2H_2 \quad \text{(HER)} \quad (2)$$

$$2H_2O \rightarrow O_2 + 4H^+ + 4e^- \quad \text{(OER)} \quad (3)$$

The PEC process starts from the absorption of photons with energy equal to or greater than the bandgap of semiconductor photocatalysts, which generate electrons in the conduction band (CB) and holes in the valance band (VB). The electrons in the conduction band (CB) with an energy level above 0.0 V vs RHE diffuse to the surface of the hydrogen evolution cocatalyst and produce hydrogen (H) (equation 2) [20]. Likewise, holes in the VB with an energy level lower than 1.23 V vs RHE diffuse to the surface of oxygen evolution cocatalysts and produce oxygen (equation 3). This process results in an overall water-splitting reaction and produces hydrogen from water under solar irradiation. The minimum voltage of 1.23 V at room temperature is required to successfully drive the OER and HER reactions. Besides the voltage, an additional energy (activation energy) is also required to run the reaction at an appreciable rate. The rate of water splitting is related to the current densities which are directly related to the activation energy; the faster the water splitting greater the activation energy that must be supplied [21]. A typical PEC setup is shown in Figure 1.2.

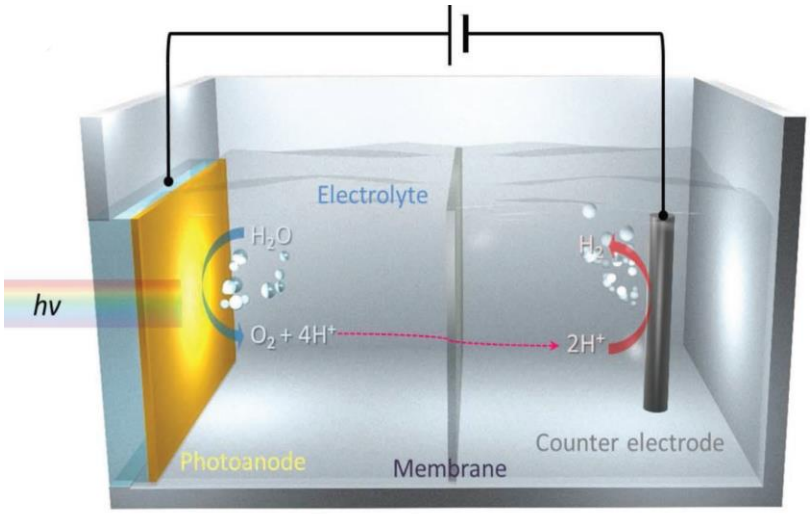

Figure 1. 2 Scheme showing the photoelectrochemical water splitting reactions and electron flow [22].

1.2.2 Photocatalytic Water Splitting

Recently, photocatalytic water splitting has attracted much attention due to its simplicity, and environmental friendly. A photocatalytic process consists of solid (powder) and liquid interfaces that directly harvest energy under sunlight illumination [12]. The photocatalytic water splitting process to hydrogen (H_2) and oxygen (O_2) is shown in Figure 1.3, where a semiconductor powder is dispersed in a pool under sunlight illumination. This kind of water-splitting system is very beneficial for large-scale production of H_2 and O_2. There are several steps involved in the photocatalytic water splitting:

Step 1st: in this step, a photon is absorbed by the semiconductor photocatalyst depending on the band gap of the semiconductor to form electron-hole pairs. To absorb a large portion of visible light, the band gap energy of the visible light driven photocatalyst should be less than 3 eV. Therefore a suitable band gap engineering is necessary to design a photocatalyst that could absorb a large portion of the visible spectrum [23].

Step 2nd: This step involves charge separation and migration of the photogenerated charge carriers, which are strongly dependent on the crystallinity, particle size, and crystal structures. Materials with high crystalline quality have less defects and most of the defects act as trapping and

recombination centers between photogenerated electrons and holes, thus it reduces the photocatalytic activity. The smaller particle size is also an important factor in charge recombination and migration. When particle size decreases the distance becomes shorter for photogenerated electron-hole to migrate easily to the reaction sites, resulting in a decrease in the probability of charge recombination.

Step 3rd: The final step, is a surface chemical reaction that depends on the active sites and surface area of the photocatalyst. The photogenerated electrons and holes will recombine if the active sites for the redox reaction do not exist on the surface of the photocatalyst. It is worth noting that the recombination of photogenerated electrons and holes occurs even if they have sufficient thermodynamic potential for water splitting [23].

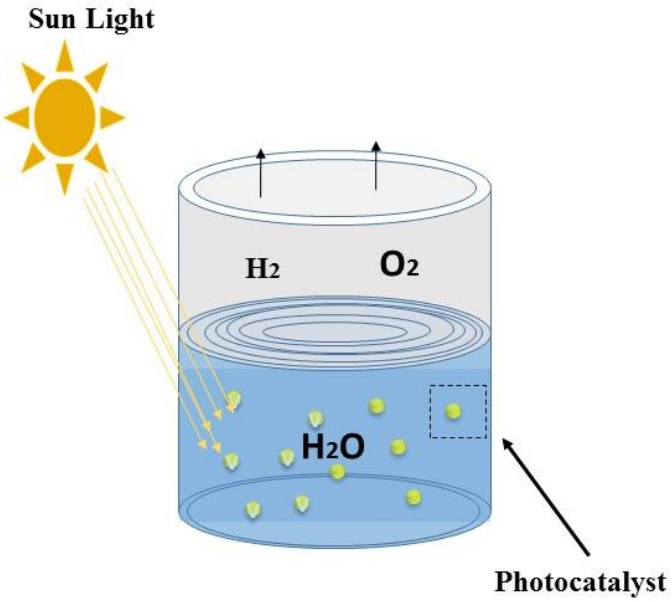

Figure 1. 3. Solar hydrogen and oxygen production from water using powder photocatalyst.

1.3 Choice of Photocatalysts

In the past few decades, semiconductor materials have attracted much attention for their environmental applications due to their electrical, optical, magnetic, electrical, mechanical, and photocatalytic properties. The ideal semiconductor in the photocatalytic setup should have the following properties which are listed below [24],

- Favorable optical band gap energies of a semiconductor that can absorb the visible region of the solar spectrum.
- Valence and conduction band edges straddle with water redox potential.
- Excellent electronic properties like higher charge separation and higher life time of photogenerated charge carries.
- Rich in producing high oxidizing and reducing species at the semiconductor/medium interface
- Chemical and photostability or photoelectrochemical stability in the aqueous solution.

The band gap distributions of many semiconductors are shown in Figure 1.4, which are likely semiconductors for photocatalytic applications. The photocatalysts include TiO_2 [25], ZnO [26], SnO_2 [27], Cu_2O [28], WO_3 [29], Fe_2O_3 [30], $SrTiO_3$, ZrO_2, $KTaO_3$, and $BiVO_4$ [31].

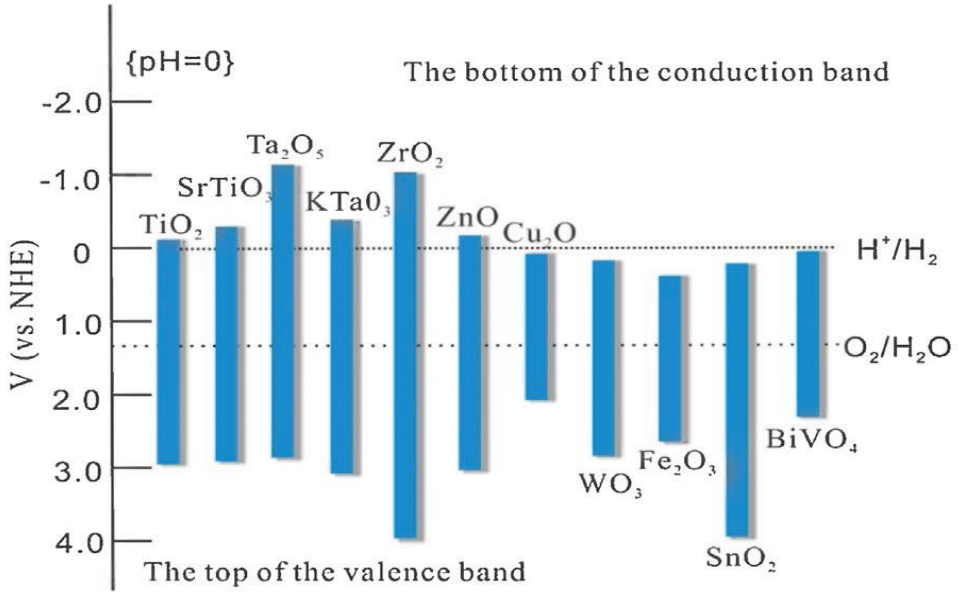

Figure 1. 4. Representing the relationship of band structure and redox potential of different photocatalytic semiconductors [31].

TiO_2 has already been used for photocatalytic water splitting by Fujishima and Honda, and has proved that it is responsible for diverting attention toward solar cells [32], photocatalysis [33], and sensing applications [34].

The photocatalysts like TiO_2, ZnO, and SnO_2 are not capable of absorbing a large portion of the solar spectrum because of their wide band gap~ 3.3 to 3.4 eV. These photocatalytic semiconductors are only responsive to the ultraviolet spectrum, absorbing 5 to 7% intensity of the solar spectrum. On the other hand bismuth vanadate ($BiVO_4$) with a narrow band gap is capable of absorbing a large portion of the solar spectrum and is responsive to visible light. Apart from these properties, $BiVO_4$ has attracted much attention due to its unique features such as non-toxicity, oxygen evolution by water splitting, photodegradation of harmful pollutants, ionic conductivity, environmental friendliness, and high charge transfer capability [35]. In many semiconductor oxide photocatalysts, the valence bands are formed by O2p orbital which is a key factor in tuning the band gap. It is crucial to use other elements to alter the band gap of semiconductor oxide instead of O2p; therefore, utilization of the visible region which constitutes ~43% of the solar spectrum, can play a vital role in enhancing photocatalytic performance. Kudo et al reported that the bandgap of $BiVO_4$ can be tuned easily by controlling the valence band element (O2p)[36].

1.4 Bismuth Vanadate ($BiVO_4$)

$BiVO_4$ is one of the potential candidates in photocatalysis because of its structural features, a tremendous work has been made to synthesize $BiVO_4$ for environmental applications since 1925 (first report) [37].

1.4.1 Historical Background of $BiVO_4$

Bismuth vanadate ($BiVO_4$) is an inorganic compound that is almost twice as abundant as gold in the earth's crust. The bismuth vanadate ($BiVO_4$) was synthesized via solid state and melting reaction by Roth and Waring in 1963 using the V_2O_5 and Bi_2O_3 as vanadium and bismuth precursors [38]. In 1975, the ferroelectric properties of the $BiVO_4$ were reported by J.D. Bierlien et al [39]. In 1980, Monolikas et al. also studied $BiVO_4$ and found that it is a promising material for acousto-optical properties [40]. Subsequently, $BiVO_4$ has attracted much interest due to its ferroelastic properties, acoustic-optical properties, ionic conductivity [41], and non-toxic pigment [42]. $BiVO_4$ has gained importance steadily over the past two decades and today it is manufactured across the globe for the use of pigment. $BiVO_4$ has wide applications despite its nontoxic yellow pigment for high-performance lead-free paints. There are many other applications of $BiVO_4$ such

as gas sensors, posistors (It's a thermal resistor like thermistor, but with positive resistance temperature factor), solid-state electrolytes, and positive electrode materials for lithium rechargeable batteries.

Since 1986, Kudo et al. have studied many materials for photocatalytic applications where they found that $BiVO_4$ is an excellent material for photocatalytic oxygen evolution and pollutant degradation using the aqueous solution of $AgNO_3$ under visible light illumination [43]. Lately, in 1999, a series of synthesis techniques were carried out to synthesize high crystalline $BiVO_4$ microparticles [44].

1.4.2 Crystal Polytypes and Optical Properties

The $BiVO_4$ semiconductor mainly exists in three-phase: monoclinic scheelite (distorted scheelite clinobisvanite), tetragonal scheelite (dreyerite), and tetragonal zircon (pucherite) as shown in Figure 1.5a-c [45]. The irreversible transition from the tetragonal zircon-type structure to the monoclinic scheelite structure occurs at the calcination temperature range from 400 °C to 500 °C. Furthermore, the monoclinic scheelite phase can be converted to a tetragonal scheelite phase at a temperature of 255 °C, and the tetragonal scheelite phase can be converted to a monoclinic scheelite phase using the same temperature. It has also been reported that the mechanical grinding (agate mortar and pestle) of tetragonal phase $BiVO_4$ can be converted to a monoclinic scheelite phase at room temperature [46] The XRD pattern of tetragonal and monoclinic $BiVO_4$ structures is shown in the Figure 1.6 which can better explain the differences between different transformed phases. Tetragonal $BiVO_4$ with a band gap of ~2.9 eV is only responsive to ultraviolet (UV) and the monoclinic $BiVO_4$ has a band gap of ~2.4 eV which is capable of absorbing both UV and visible spectrums. The UV absorption in tetragonal and monoclinic $BiVO_4$ is related to the band transition from O2p to V3d and visible absorption of the monoclinic $BiVO_4$ is related to the transition from Bi6s or hybrid of O2p and Bi6s to the conduction band (CB) of V3d [47]. The absorption coefficient of the m-s $BiVO_4$ is shown in Figure 1.5e, which increases from $1 \times 10^4\ cm^{-1}$at the band edge absorption onset of 500 nm to $1 \times 10^5\ cm^{-1}$ at 460 nm. Additionally, plateau can be observed in between 430 nm and 390 nm. The absorption coefficient increases when the wavelengths shorter than 390 nm. The yellow color of the $BiVO_4$ is related to the strong absorption of green to ultraviolet photons in visible region and transmission of yellow to infrared photons in visible region.

1.4.3 Electronic Structure of $BiVO_4$

$BiVO_4$ exists in three phases as discussed previously, where in all these three structures the vanadium (V) ions are bonded to four oxygen (O) atoms on the tetrahedron side and Bi ions are bonded to eight O atoms. Scheelite and tetragonal structures are different because of the Bi ions bound to VO_4 tetrahedron i.e. in scheelite Bi ions are surrounded by eight VO_4 tetrahedrons and Bi ions in tetragonal zircon structure surrounded by six VO_4 tetrahedra. Similarly, considering the scheelite phases of the $BiVO_4$, the tetragonal scheelite structure consists of a V-O bond length of 1.72 A° and monoclinic of consists of different V-O bond lengths of 1.77 A° and 1.69 A° [48]. Furthermore, there are four lattice sites in the basic monoclinic structure Bi (4e), V (4e), O1 (8f), and O2 (8f). [49] The electronic properties of the monoclinic scheelite $BiVO_4$ phase have been studied and found that the photocatalytic response of the m-s $BiVO_4$ under visible light illumination is much better than the tetragonal zircon $BiVO_4$.

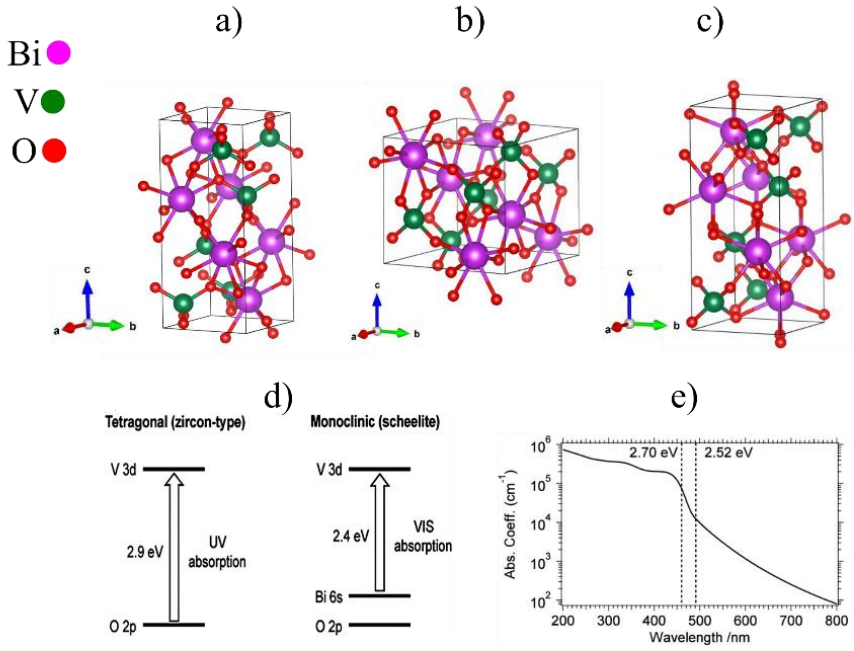

Figure 1.5. Crystal structure of $BiVO_4$: (a) Pucherite, (b) tetragonal zircon, (c) monoclinic scheelite [3], (d) band structures of monoclinic scheelite and tetragonal zircon $BiVO_4$ [7] and,(e) absorption of monoclinic $BiVO_4$ [50].

The better photocatalytic response of the monoclinic $BiVO_4$ was found because of the additional states formed by the Bi 6s and O 2p orbitals above the valence band, causing shifts up the valence band as compared to other crystal phases. The upshifts cause a lowering of the bandgap, which further helps to increase the photoabsorption as shown in Figure 1.5d [44]. The DFT calculations also demonstrated that m-s $BiVO_4$ is an indirect bandgap semiconductor material whereby the top of the valence band was estimated to consist of Bi 6s and O $2p_\pi$ states and the estimated conduction band consists of V $3dx^2\text{-}y^2$ and dz^2 states. These Bi 6s and O $2p_\pi$ states help in decreasing the bandgap [51].

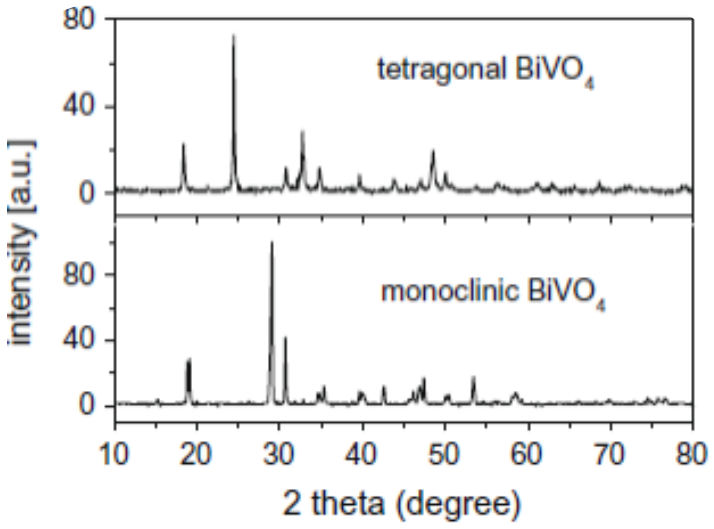

Figure 1. 6. XRD pattern of tetragonal, and monoclinic $BiVO_4$ [52].

1.4.4 Limitations of the monoclinic $BiVO_4$

$BiVO_4$ is a photocatalyst used in the degradation of organic pollutants, oxygen production, and CO_2 reduction, where in the case of O_2 evolution the photogenerated holes of the $BiVO_4$ are consumed by the water to produce O_2. The monoclinic phase of $BiVO_4$ is one of the best phases with an excellent photocatalytic response because of the Bi 6s and O 2p orbital. The valence band (VB) edges of the monoclinic $BiVO_4$ are located at ca. 2.4 eV vs. reversible hydrogen electrode (RHE). The lower bandgap of monoclinic $BiVO_4$ makes it capable of absorbing a large portion of visible light resulting in the theoretical photocurrent density of 7.5 mA/cm^2. Furthermore, assuming that all the photons having energies greater than the bandgap of $BiVO_4$

are absorbed would result in 9% Solar-to-Hydrogen efficiency under AM 1.5 G solar illumination. [53]. However, the practical solar to hydrogen efficiency of the monoclinic $BiVO_4$ is still far apart from an ideal photocatalyst due to some limitations:

- Low mobility of the photogenerated charge carriers in the bulk leads to the recombination of electron-hole before reaching the interfaces [54].
- Polaron formations in the $BiVO_4$ delay the charge separation which further leads to a reduction in the carrier diffusion length to 70 nm.
- The oxygen evolution kinetics of $BiVO_4$ is very slow as compared to the oxidation of sulfite because it takes place with an extremely fast oxidation process; therefore, neglecting the surface recombination.
- The conduction (CB) band position is lower than the reduction potential of water (normal hydrogen electrode (RHE) level).
- Limited surface reactions due to weak surface absorption [55].

Many methodologies have been used for the improvement of the photocatalytic activity of $BiVO_4$ such, as shallow-level doping, novel nanostructures, loading cocatalysts, heterojunction, and morphological control (surface modification). Doping, in general, modifies the electrical properties of semiconductors; for example, doping of metallic ions in semiconductor oxide improves carrier concentrations and conductivity which is probably due to the presence of a high valence state of metal ions dopants. The doping of transition metals in $BiVO_4$ can induce intermediate levels in between the valence and conduction band which reduces the band gap energies. The electrons can easily excite from these intermediate levels to the conduction band in the doped $BiVO_4$ as compared to un-doped $BiVO_4$ because of utilizing lower photon energy.

1.4.5 Photocatalytic process in the perspective of metal-doped $BiVO_4$

The charge migration, recombination, separation, light absorption, and the driving force for photocatalytic chemical reactions of semiconductors are governed by the electronic band structure of a semiconductor. Metal doping is an effective method that can modify the electronic structure of semiconductor photocatalysts to further enhance the intrinsic electronic conductivity and introduce polarons; thus, improving the charge carrier concentration. $BiVO_4$ doped by metals can result in improved photoinduced charge migration to reduce charge recombination, narrow the

band gap by forming sub-energy levels that enhance the photon absorption, and create oxygen vacancies that work as an electron trapping center to enhance charge separation [49,56]. As a result, metallic doping improves the photocatalytic performance of a semiconductor [57].

$BiVO_4$ has been doped with some non-metals, transition metals ions, rare earth metals, and noble atoms, where the non-metals ions include B, C, F, N, S, and P [58–60], and noble atoms include Ag, Au, Pd, and Pt. The transition metal and the rare earth metals dopants include Mo, W, Cr, Ta, Zr, Si, Ti, Zr, Hf, Sn, Fe, Sr, Zn and La, Eu, Er, Y, Ho, Yb, Sm, Nd and Gd [61–63]. Generally, the doping changes electronic structure it may contribute to improving photocatalytic activity. However, the changes in the electronic structure of a semiconductor depend on the atomic radii of the dopants and the doping sites in the semiconductors [64]. As an example, a $BiVO_4$ semiconductor has two doping sites i.e. Bi^{+3} and V^{+5}, therefore doping of metals to these sites can result in different structures depending on the type of dopants [65].

There are two possibilities for occurring doping in semiconductor photocatalysts, i.e. substitutional/ interstitial doping and cluster loading.

1.4.6 Substitutional/ interstitial doping

The doping atoms can be inserted into the crystalline site by replacing the host atom in the crystallite site. Foreign atoms can be added to the interstitial sites of a crystal without replacing the host atoms, which is called interstitial doping. Both doping methods are important in boosting photocatalytic activities by generating more charges [49].

Several studies have been devoted to the impact of the metallic ion dopants such as Mo^{6+}, W^{6+}, Cr^{6+}, Ta^{5+}, Zr^{5+}, Si^{4+}, Ti^{4+},Zr^{4+}, Hf^{4+}, Sn^{4+}, La^{3+}, Fe^{3+}, Sr^{3+}, Cu^{2+}, Zn^{2+} and Ag+ on the photoelectrochemical (PEC) and photocatalytic (PC) applications. The $BiVO_4$ material has two dopant sites i.e. Bi^{3+} and V^{5+} Z. Zhao et al. have studied the impact of metal dopants on the Bi^{3+} and V^{5+} sites in $BiVO_4$ by using density function theory (DFT) [66]. Mo^{6+}, W^{6+}, and Cr^{6+} were chosen as substitutional elements for the V^{5+} site, and Ti^{4+},Zr^{4+}, Hf^{4+}, and Sn^{4+} were chosen as substitutional elements for Bi^{3+} sites of the $BiVO_4$. It was also shown experimentally and theoretically, that only Mo^{6+} and W^{6+} have a greater impact on the improvement of the photocatalytic activity of the $BiVO_4$ [67,68]. Mo^{6+} and W^{6+} can increase the photocatalytic activity of the $BiVO_4$ photocatalyst due to the higher donor density. The high donor densities may shift the

Mo^{6+} and W^{6+} fermi levels towards the conduction band which helps further in accelerating charge separation by band bending, therefore enhancing photocatalytic activity. The boost in the photocatalytic activity of $BiVO_4$ by the metallic dopants (Mo^{6+} and W^{6+}) can also be attributed to the increase in the charge carriers mobility and diffusion length [65,69].

Non-metals dopants i.e. B, C, N, F, P, and S in $BiVO_4$ semiconductors were also studied for photocatalytic applications. In the study, three major issues i.e. band gap narrowing, impurity energy level, and oxygen vacancy were addressed. The photocatalytic oxygen evolution activity of the doped $BiVO_4$ photocatalysts is shown in Table 1.1.

Band gap narrowing: M.Wang et al. doped m-s $BiVO_4$ with nitrogen (N) and thus found that the band gap of N-$BiVO_4$ is narrowed up to 2.23 eV and able to absorb visible light until 600 nm [70]. Likewise, in another study by Y. Li et al, it was found that the B substituted in V sites can form localized defect levels just above the valence band (VB) of $BiVO_4$ [71].

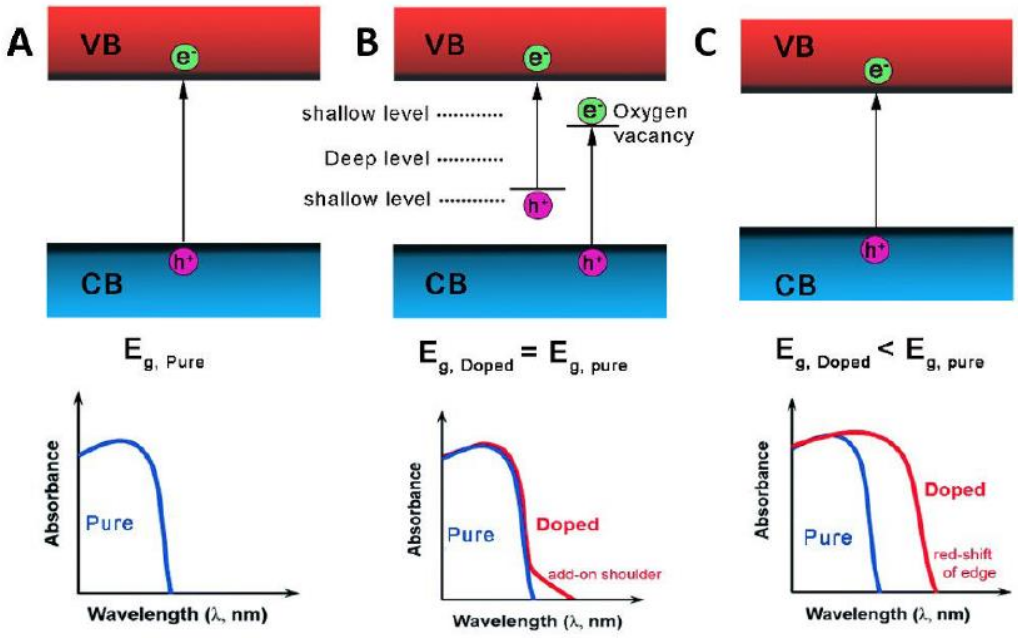

Figure 1.7 Scheme diagram showing the band structure and optical curves of (a) pure semiconductor, (b) doping-induced shallow-level and deep-level states, and (c) induced band gap narrowing [72].

Impurities energy level: in one study Z. Zhao et al. suggested that sulfur impurities can reduce the band gap energy of the $BiVO_4$. They further suggest that mixing S 3p with Bi 6s as well as with O 2p in the VB of $BiVO_4$ could be the main factor in decreasing band gap energies. As a result, the Sulphur may form impurities above the valence band [59].

Oxygen vacancies: Nitrogen was substituted in the place of oxygen vacancies as pointed out by M.Wang et al. Additional oxygen vacancies and V sites would become active sites for $BiVO_4$ and are beneficial for the enhancement of the photocatalytic activity of N-$BiVO_4$ (Figure 1.7b) [71].

Substitutional doping can affect the band gap of a semiconductor by creating an intermediate state above the valance band. These intermediate states result from the hybridization of the valence band (VB) and conduction band (CB) states by the dopants, thereby narrowing the band gap and extending the absorption spectral range to higher wavelengths [73]. The shallow or intermediate states could promote charge carrier mobility and increase the minority charge carrier diffusion length. Substitutional doping can change the electronic structure of the semiconductor, depending on the dopant concentrations. Also, substitutional doping causes variations in cell parameters depending on the substitution sites [74]. Taking Mo dopant is an example in the $BiVO_4$ structure which improves the conductivity when replacing V^{5+} atoms with Mo^{6+} atoms and contributes one extra electron in photocatalytic reactions [55,75].

1.4.7 Heterojunction

Heterojunction or heterostructures is a well-known technique consisting of two or more semiconductors which is beneficial for light absorption, and charge separation in photocatalytic systems. It is worth mentioning that only a few photocatalysts fulfill the minimal required thermodynamic criteria, while most of them only absorb ultraviolet (UV) light [3].

Heterostructures have three main types. i.e. type-I (straddling gap), type-II (staggered gap), and type-III (broken gap). These heterostructure types depend on the valence (VB) and conduction (CB) band energy positions of the individual semiconductors [76,77]. The band diagram of type-I, type-II, and type-III heterojunction is given in Figure 1.8.

Type-I heterojunction*:* It consists of two semiconductors i.e. semiconductor 1 (SC-I), and semiconductor 2 (SC-II), where they can be either *n*-type or *p*-type. In the type-I heterojunction setup, the conduction band of SC-II is higher than the conduction band of SC-I, while the valence band of SC-I is higher than the valence band of SC-II. Therefore, electrons and holes will transfer and accumulate on SC-I [76].

Type-II heterojunction*:* It also consists of two semiconductors i.e. SC-I, and SC-II, where the conduction band of the SC-II is more negative while the valence band of the SC-I is more positive. The photoexcited electrons can transfer from the conduction band of SC-II to the conduction band of SC-I due to the more negative conduction band of the SC-II. On the other hand, the hole can transfer from the valence band of the SC-I to the valence band of the SC-II because of the more positive valance band of the SC-I. These kinds of charge transfer mechanism leads to efficient charge separations and enhanced photocatalytic activity.

Type-III heterojunction*:* As shown in Figure 1.8, the structure of the type-III heterojunction is identical to that of the type-II heterojunction except that the staggered gap becomes so extreme that the bandgap does not overlap. Therefore, the electron-hole separation and migration cannot occur between SC-I and SC-II, making it unsuitable for improving charge separation and migration [78].

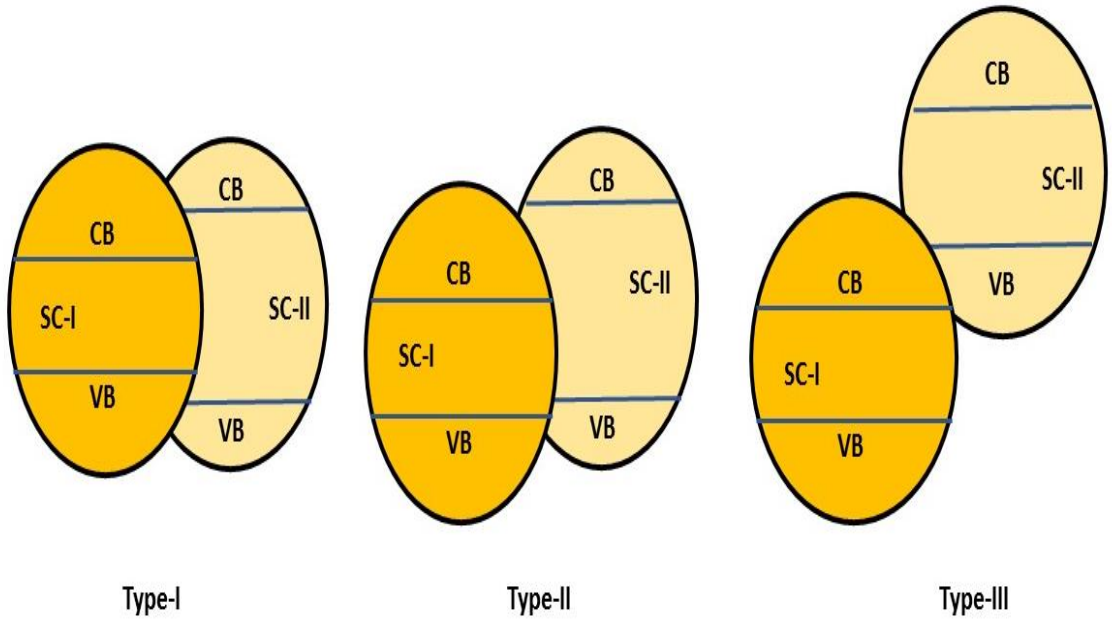

Figure 1.8. Band alignment in type-I, type-II, and type-III heterojunctions.

Type-II heterojunctions are considered more valuable than other heterojunctions due to their unique charge transfer and separation capabilities. Hence it is considered more favorable for photocatalysis [79]. There are two possibilities for the charge transfer in type-II heterostructures i.e. electron transfer, and hole transfer. In the first case, the electron moves from a material with

a more negative conduction band (CB) to another material with a more positive conduction band (CB). The holes follow an opposite trend to that of electrons, transferring from a material having a more positive valence band (VB) to a material with a more negative valence band potential.

Recently heterojunctions between two materials have attracted much attention, which include semiconductor-semiconductor, semiconductor-metal, and semiconductor-carbon heterojunction structures [79]. By far the most commonly used heterojunction is the semiconductor-semiconductor heterojunction, which is mostly formed by close contact between *p*-type and *n*-type semiconductors. The result is a space charge region at the interface and an electric field is added as a result of charge diffusion. This can enable a direct flow of electrons to the conduction band of the *n*-type semiconductor material while the hole to the valence band of the *p*-type semiconductor material; thus, enabling efficient charge separation, longer charge carrier lifetime, and higher reaction rate[76].

1.4.8 Bimetallic Cocatalysts Loading

The method in which metal nanoparticles (NPs) are added to the surface of a semiconductor is called metal loading. Metal oxide cocatalysts are attached to the photocatalysts which can improve the local photocatalytic rate and charge separation by creating a built-in electric field [80]. Sparsely attaching metallic cocatalysts at the surface of a photocatalyst induces barrier heights which as a result change the surface charge density, forming a lateral electric field [81]. $BiVO_4$ has been investigated for loading transition metals such as Cu, Co, Ni, Fe, and Mn and found beneficial to improving photocatalytic activity [62,82]. The photocatalytic activity of the m-s $BiVO_4$, as well as doped m-s $BiVO_4$, can be further improved by depositing cocatalysts like FeNi, FeOOH, Co-Pi, CoO, NiO, Co-Bi, Ni-Bi, and Fe-Ce as a surface catalyst [83]. $FeCoO_x$ was used as a surface co-catalyst on the m-s $BiVO_4$, which helped in suppressing charge recombination at the surface of $BiVO_4$; thus, better improvements were observed in the photocatalytic activity of the photocatalysts [84]. The scheme diagram of the $BiVO_4$ photocatalyst loaded with cocatalysts is shown in Figure 1.9 where the $BiVO_4$ photocatalyst and cocatalyst fermi levels aligned with each. Therefore, these cocatalysts will work as electron-trapping agents. Many strategies have been developed to deposit co-catalysts on the $BiVO_4$ but magnetron sputtering is one of the best methods to deposit surface co-catalyst on $BiVO_4$. Magnetron sputtering deposition is a coating technique at a high vacuum that allows the deposition of many types of materials i.e. ceramics and metals, on

different kinds of the substrate by the use of a magnetic field applied to a sputtering target. It is considered one of the green synthesis techniques for the production of different metallic nanoparticles [85]. The main advantage of using magnetron sputtering for the deposition of nanoparticles (NPs) is that it is a contamination-free, scalable, and controllable technique that can be applied to produce limitless NPs by choosing an appropriate sputtering target and gas composition inside the sputtering chamber [86]. The magnetron sputtering can produce NPs in different solid and liquid substrates that allows to control size, concentration and shape of NPs. Furthermore, in a magnetron sputtering deposition process, the powder continuously moving by the use of agitating resonant mechanical apparatus which further ensure the homogenous deposition of NPs over particulate system. [87].

Table 1.1. Several $BiVO_4$ photocatalysts in the form of powder for photocatalytic oxygen evolution.

S.NO	**Sample**	**Photocatalytic Application**	**Intensity and lamp**	**O_2 Evolution**	**References**
1	W:BVO/$FeMnO_x$ and W:BVO/$FeNiO_x$	Oxygen evolution	300 W Xe lamp (AM 1.5 G)	181 μmol = 2413 μmol $g^{-1}h^{-1}$ and 175 μmol = 2333 μmol $g^{-1}h^{-1}$	**This work**
2	$BiVO_4$	Oxygen evolution	300 W Xe lamp with cut-off filter	90 μmol.g^{-1}	[88]
3	$BiVO_4$	Oxygen evolution	300 W Xe lamp with cut-off filter	253 μmol $g^{-1}h^{-1}$	[89]

4	Mo:$BiVO_4$	Oxygen evolution	300 W Xe lamp with cut-off filter	600 μmol g^{-1} h^{-1}	[55]
5	Ce:doped $BiVO_4$	Oxygen evolution	300 W Xe lamp 285 mW/cm^{-2}	800 μmol g^{-1} h^{-1}	[90]
6	$BiVO_4$	Oxygen evolution	300 W Xe lamp with cut-off filter	500 μmol g^{-1} h^{-1}	[91]
7	W-doped $BiVO_4$	Oxygen evolution	Mercury lamp 125W, light output 7 x 10^{18} photons/sec	739 μmol g^{-1} h^{-1}	[92]
8	Zr-doped $BiVO_4$	Oxygen evolution	300 W Xe lamp with cut-off filter	1108 μmol g^{-1} h^{-1}	[92]
9	W-doped $BiVO_4$	Oxygen evolution	Plasma lamp, 100 W/cm^{-2}	686 μmol $g^{-1}h^{-1}$	[65]
10	Mo-doped $BiVO_4$	Oxygen evolution	Plasma lamp, 100 W/cm^{-2}	942 μmol $g^{-1}h^{-1}$	[65]
11	Zr-Doped $BiVO_4$	Oxygen evolution	300 W Xe lamp	550 μmol g^{-1} h^{-1}	[93]
12	Cu-Doped $BiVO_4$	Oxygen evolution	300 W Xe lamp	350 μmol g^{-1}	[94]

13	$NiO_x(OH)_y/BiVO_4$ and $CoO_x(OH)_y/BiVO_4$	Oxygen evolution	300 W Xe lamp with cut-off filter	1538 $\mu mol\ g^{-1}h^{-1}$	[95]
14	$CoOx/BiVO_4$	Oxygen evolution	300 W Xe lamp with cut-off filter	1733 $\mu mol\ g^{-1}h^{-1}$	[96]

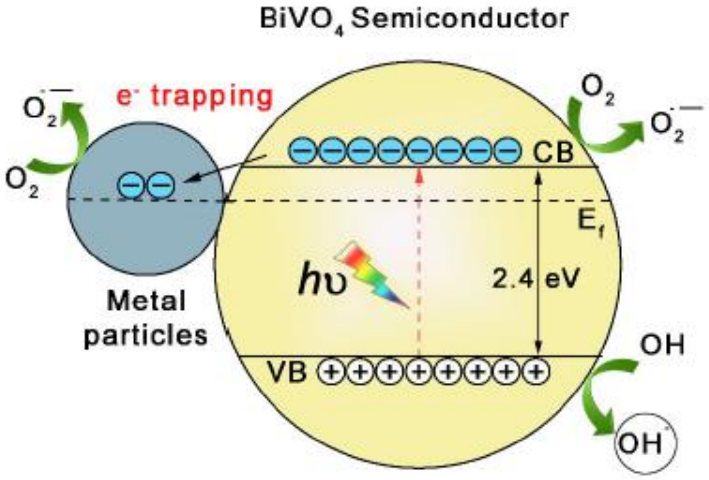

Figure 1.9. Schematic diagram, representing $BiVO_4$ photocatalyst loaded with bimetallic cocatalysts.

1.5 Research Objectives

Producing tungsten (W) and zinc (Zn) doped $BiVO_4$ photocatalysts by hydrothermal synthesis method and then loading a bimetallic oxide cocatalysts i.e. $FeMnO_x$, and $FeNiO_x$ as surface cocatalysts for improved photocatalytic oxygen evolution. The purpose of metallic doping is to change the electronic structure of the $BiVO_4$ photocatalysts by creating an energy (sub-energy level) level above the valence band to reduce the bandgap and increase absorption spectra which may improve the charge separation in the bulk. On the other hand loading of $FeMnO_x$, and $FeNiO_x$

metallic cocatalysts to improve the surface charge separation of the pure and doped $BiVO_4$ by forming a p-n heterojunction (typically type-II) by p-type $FeMnO_x$ and $FeNiO_x$ cocatalysts and n-type $BiVO_4$.

***Specific objectives*:**

- Producing W and Zn doped $BiVO_4$ powder via hydrothermal synthesis.
- To use RF-magnetron sputtering for the deposition of $FeMnO_x$ and $FeNiO_x$ bimetallic cocatalysts on $BiVO_4$.
- Evaluating photocatalytic activity of the photocatalysts through photocatalytic oxygen (O_2) evolution reaction under AM1.5 G solar irradiations.
- Understanding different properties of $BiVO_4$ through X-ray diffraction spectroscopy (XRD), X-ray photoelectron spectroscopy (XPS), Scanning electron spectroscopy (SEM), UV-vis spectroscopy, Raman spectroscopy, and high-resolution transmission electron microscopy (HRTEM).

$BiVO_4$ photocatalyst doped with W and Zn will improve the photocatalytic activity for O_2 evolution which will be discussed in upcoming chapters. $BiVO_4$ nanoparticles achieved through the hydrothermal process were loaded with novel $FeMnO_x$, and $FeNiO_x$ bimetallic cocatalysts which can further improve the photocatalytic oxygen evolution.

Chapter 2

2. Synthesis and characterization techniques

2.1 Materials and Methods

2.1.1 Chemicals

All reagents were purchased from Sigma-Aldrich and used without further purification. Bismuth(III) nitride-pentahydrate (99% purity) and ammonium methavandate (99% purity) were used as Bismuth (Bi) and vanadium (V) precursors. Sodium tungstate dihydrate ($Na WO_4. 2H_2O$, 99% purity) and Zinc nitrate hexahydrate ($Zn(NO_3)_3.6H_2O$, 99% purity) were used as W and Zn precursors. All the solutions were prepared in nitric acid (≥70%), ammonium hydroxide (28.0-30.0% NH_3 basis), and deionized water.

2.2 Hydrothermal Synthesis

2.2.1 Preparation of pure bismuth vanadate ($BiVO_4$) powder via hydrothermal technique

Bismuth vanadate ($BiVO_4$) powder was synthesized via a hydrothermal process as shown in Figure 2.1. Bismuth nitride pentahydrate ($Bi(NO_3)_3.5H_2O$) and ammonium metavanadate (NH_4VO_3) are used in a 2 mmol ratio as bismuth and vanadium precursors. Initially, $Bi(NO_3)_3.5H_2O$ was dissolved in 8 ml of HNO_3 (2 M) and stirred magnetically for 30 min which was named solution A. Further, NH_4VO_3 was dissolved in 22 ml of $NH_3.H_2O$ (2 M) and stirred magnetically for 30 min which was named solution B. Solution B was added dropwise to solution A and adjusted the pH of the solution to 7.5, using $NH_3.H_2O$ and HNO_3 and stirred magnetically for 2 h. The entire solution was shifted to a 100 ml Teflon-lined stainless steel autoclave and then the autoclave was kept inside the heating furnace at 200 °C with a heating rate of 10°C/min for 24 h. The autoclave was removed from the furnace after 24 hours and kept at room temperature for 3 h. After cooling down the reactor at room temperature, the precipitant was collected through centrifugation with 5000 r.p.m for 15 min and then washed with water and ethanol three times repeatedly. Finally, the yellow $BiVO_4$ precipitants were dried at 80°C for 6 h and labeled as BVO [97].

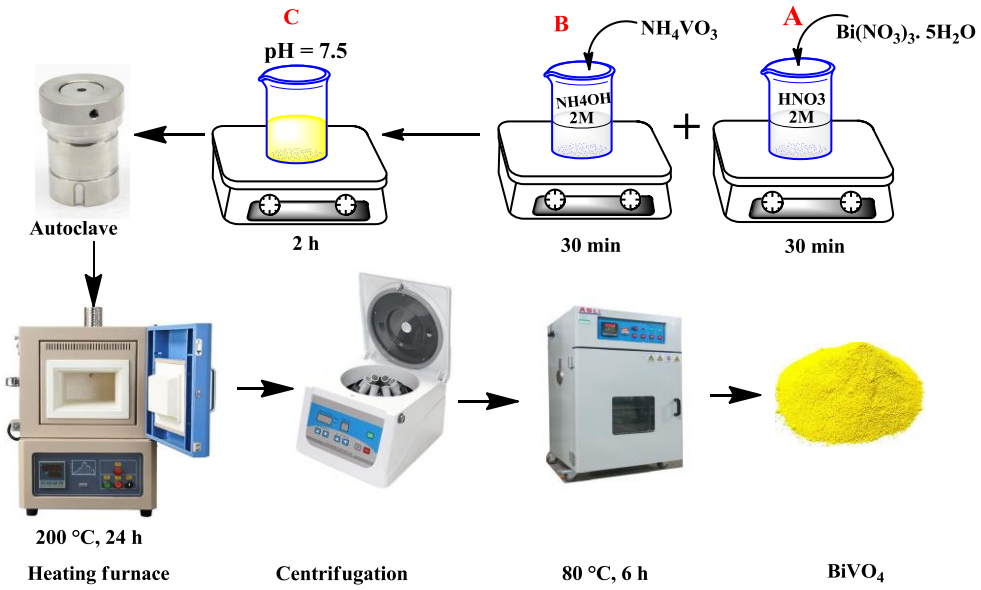

Figure 2. 1. Schematic diagram, representing different steps involved in the hydrothermal synthesis process.

2.2.2 Preparation of tungsten (W) and zinc (Zn) doped bismuth vanadate ($BiVO_4$) powder via hydrothermal technique.

The same procedure was used for the preparation of W-doped and Zn-doped $BiVO_4$ as shown in Figure 2.2. Initially, 2 mmol of $Bi(NO_3)_3.5H_2O$ was dissolved in 8 ml of HNO_3 (2M) and stirred magnetically for 30 min which was named solution A. Further, 2 mmol of NH_4VO_3 was dissolved in 22 ml of $NH_3.H_2O$ (2 M) and then 1%, 2%, and 3% molar ratio of sodium tungstate dihydrate ($Na\,WO_4.\,2H_2O$) were added to the same container (NH_4VO_3 was reduced according to the molar ratio of $Na\,WO_4.\,2H_2O$) and stirred magnetically for 30 min which named solution B. Solution B was added dropwise to solution A and adjusted the pH to 7.5. The entire solution was shifted to a 100 ml Teflon-lined stainless steel autoclave and kept inside the heating furnace at 200 °C with a heating rate of 10°C/min for 24 h. Finally, yellow precipitants were collected through centrifugation, washed three times with water and ethanol respectively, and dried at 80°C for 6 h. These samples were named 1%W:BVO, 2%W:BVO and 3%W:BVO where W, stands for tungsten and BVO for the $BiVO_4$.

The same procedure was followed for the Zn doped $BiVO_4$ synthesis where $Bi(NO_3)_3.5H_2O$ was initially dissolved in 8ml of 2M HNO_3 and stirred for 30 min at room temperature until a transparent solution was obtained which was named solution A. Further, NH_4VO_3 was dissolved

in 22 ml of 2M $NH_3.H_2O$, and then added 1%, 2%, and 3% molar ratio of $Zn(NO_3)_3.6H_2O$ and stirred for 30 min at room temperature which was named solution B . Solution B was added dropwise to solution A and adjusted the pH value to 7.5 using HNO_3 and $NH_3.H_2O$ solutions following by stirring for 2 h. After 2 h vigorously stirring, the entire yellow solution was shifted to 100 ml Teflon-lined stainless steel autoclave and then kept in the heating furnace at 200 °C with a heating rate of 10°C/min for 24 h. Finally, yellow precipitants were collected through centrifugation, washed three times with water and ethanol respectively, and dried at 80°C for 6 h This way we obtained three other samples named BVO:Zn1%, BVO:Zn2%, and BVO:Zn3% (Figure 2.2).

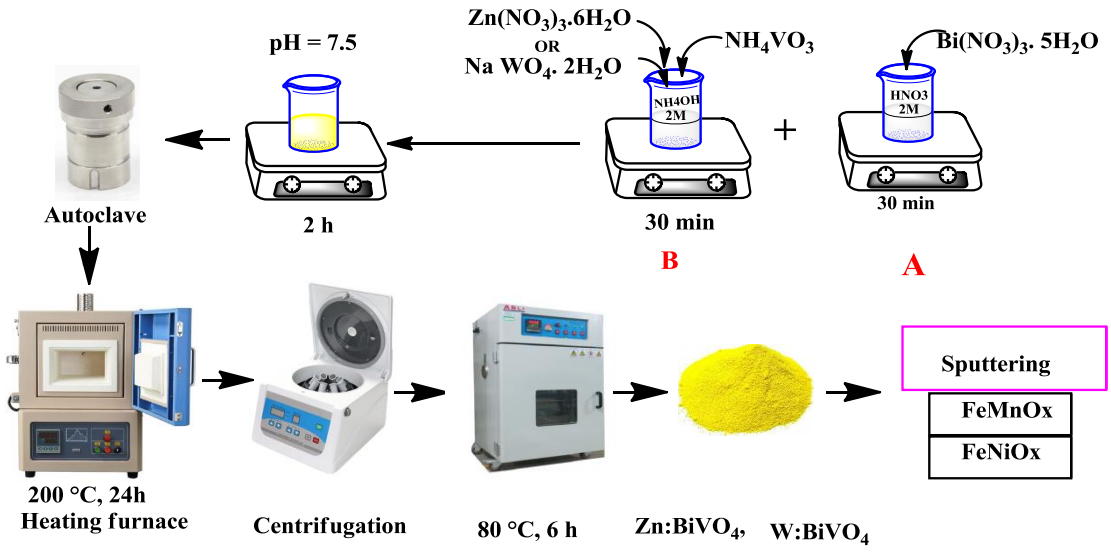

Figure 2. 2. Schematic diagram, representing hydrothermal synthesis process of W and Zn doped $BiVO_4$.

2.2.3 Loading of $FeMnO_x$ and $FeNiO_x$ bimetallic cocatalysts on pure BVO, 2% tungsten (W), and 2% zinc (Zn) doped bismuth vanadate ($BiVO_4$) powder via RF magnetron sputtering.

Bimetallic alloy targets were used in our project where the individual metals for $FeMnO_x$ alloy composed of Fe (50 wt. % Fe with 99.9% purity) and Mn (50 wt. % Mn with 99.9% purity) and for $FeNiO_x$ Fe (50 wt. % Fe with 99.9% purity) and Ni (50 wt. % Ni with 99.9% purity). The RF-magnetron sputtering deposition setup is shown in Figure 2.3, which was used for the

deposition of $FeMnO_x$ and $FeNiO_x$ bimetallic cocatalysts on $BiVO_4$ powder samples. The distance between the target and the sample was kept at 5 cm to ensure constant deposition. The working and base pressure was set to 3.2×10^{-2} and 7.5×10^{-6}Torr, where the composition of the working pressure was oxygen and argon in the ratio of 18.5 Ar sccm and 2.1 O_2 sccm. The deposition of $FeMnO_x$ and $FeNiO_x$ was accomplished using the RF power of 50 W. The $BiVO_4$ powder was placed at the bottom of round shaped capsule connected to the mechanical agitator with a sinusoidal wave frequency of 90 to 100 Hz which agitated the powder during the deposition. Bimetallic iron-manganese oxides ($FeMnO_x$) and iron-nickel oxides ($FeNiO_x$) nanoparticles were deposited on 150 mg of the pure $BiVO_4$ via RF-magnetron sputtering for 5, 10, and 20 min respectively. These samples were named 5-BVO/$FeMnO_x$, 10-BVO/$FeMnO_x$, 20-BVO/$FeMnO_x$, 5-BVO/$FeNiO_x$, 10-BVO/$FeNiO_x$, and 20-BVO/$FeNiO_x$ after the deposition.

The same procedure was used to deposit $FeMnO_x$, $FeNiO_x$ on 150 mg of W:BVO and Zn:BVO via RF-magnetron sputtering for 10 min. After synthesis the samples were named W:BVO/$FeMnO_x$, W:BVO/$FeNiO_x$, Zn:BVO/$FeMnO_x$, and Zn:BVO/$FeNiO_x$.

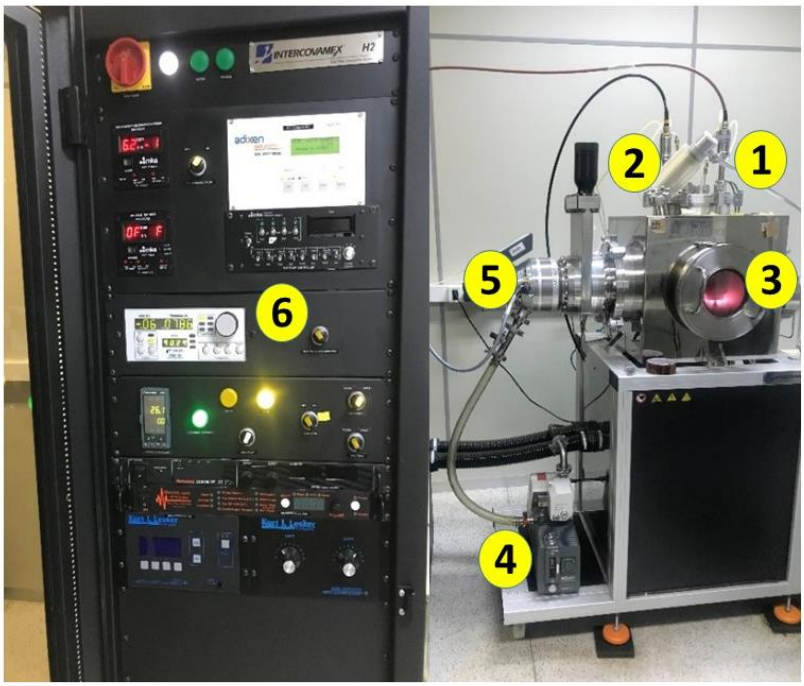

Figure 2. 3. RF magnetron sputtering deposition setup for powder and films: (1) Spray deposition system, (2) deposition gun, (3) high vacuum camera, (4) mechanical pump, (5) turbo molecular vacuum pump, and (6) control system

2.3 Synthesis of films

2.3.1 Cleaning of FTO

Flourine-doped tin oxide (FTO) is a conducting substrate made of glass transparent that was in our project used to obtain thin films (photoanodes). Initially, the FTO substrates were cleaned using 15 % soap and 85 % DI water at 90 °C for 1 h and then washed with ethanol, isopropyl, and acetone at 90 °C for 10 min separately. Furthermore, already washed FTO were dried in an oven at 80 °C for 1 h and then heated in a furnace at 500 °C for 1 h with a heating rate of 10 °C/ min and cooling rate of 2 °C/ min.

2.3.2 Synthesis of W:BVO, W:BVO/$FeNiO_x$ and W:BVO/$FeMnO_x$ films

For the mott-Schottky measurements, samples were prepared via the spin coating technique as shown in Figure 2.4. Initially, 10 mg of the already prepared W-doped $BiVO_4$ powder of each sample was dissolved in 2 ml of dimethyl sulfide (DMSO) separately and then mixed to form a slurry. 100 µL of the prepared solution was deposited on the already cleaned FTO via spin coating, using 500 r.p.m for 5 s, and then 3000 r.p.m for 10 s. Furthermore, the prepared film was dried at 150 °C for 25 min, this way one layer formed. The whole process was repeated 8 times to obtain eight layers based on our previous research work [98]. Finally, the prepared films were calcined at 300 °C for 1 h.

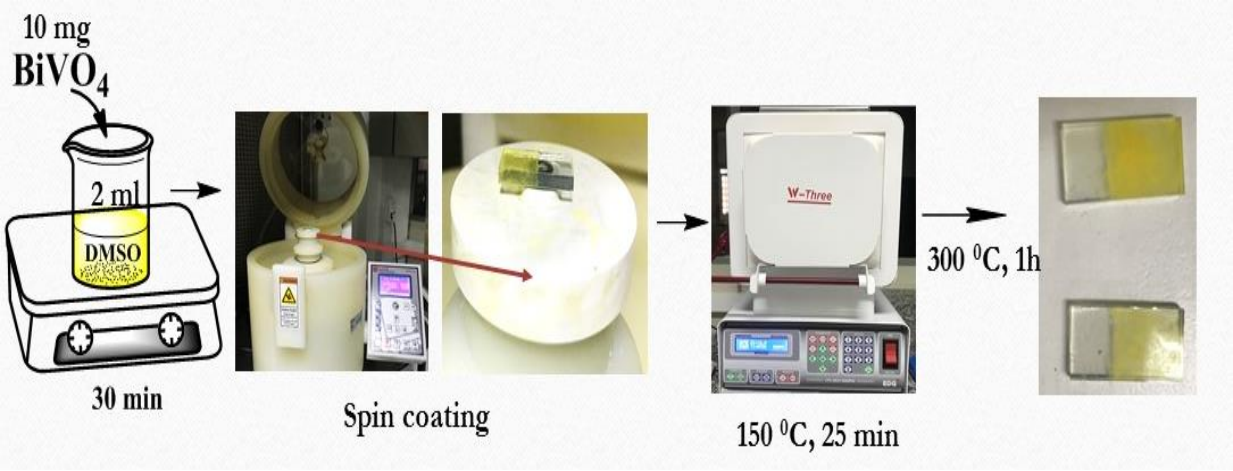

Figure 2. 4. Synthesis process of W:BVO, W:BVO/$FeNiO_x$, and W:BVO/$FeMnO_x$ films.

2.3.3 Synthesis of pure $FeNiO_x$ and $FeMnO_x$ films

Iron-manganese oxides ($FeMnO_x$) and iron-nickel oxides ($FeNiO_x$) nanoparticles were deposited on FTO via RF-magnetron sputtering for 10 min respectively. The distance between the sample and the target was kept constant (5 cm) for all the depositions. The working and base pressure was set to 2.1×10^{-2} and 1.6×10^{-6}Torr, which was composed of argon gas (15 ml min^{-1}). The deposition of FeMn (50 wt. % Fe and 50 wt. % Mn, 99.9% purity) and FeNi (50 wt. % Fe and 50 wt. % Ni, 99.9% purity) was accomplished with the RF power of 50 W.

The sample preparation map is also given in Figure 2.5, which further explains the $BiVO_4$ powder sample preparation with dopants and then the deposition of $FeMnO_x$, and $FeNiO_x$ cocatalysts via the sputtering technique.

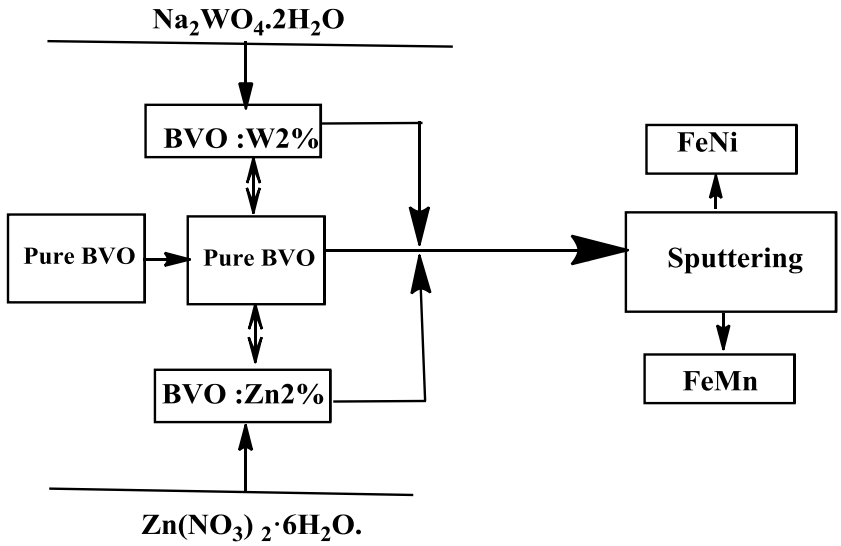

Figure 2. 5. Sample preparation map, showing different steps involved in the synthesis process.

2.4 Characterization

2.4.1 X-ray Diffraction (XRD) of Powder Samples

X-ray diffraction (XRD) is an analytical technique used for the identification of crystal structure and dimensions of a unit cell. In our experimental work, the XRD was performed to characterize the crystal structure and composition using Rigaku x-ray diffractometer (Ultima IV) operated at 40 kv and 40 mA with Cu-Ka radiations (λ = 1.5406 Å). The x-ray diffraction pattern was obtained at 2θ = 10° to 80°.

2.4.2 Scanning Electron Microscopy (SEM)

Scanning electron microscopy is a technique that uses an electron beam to analyze the morphology of the material. In our research work, the surface morphology of the prepared powder samples was investigated by SEM_ZEISS FEG Sigma Gemini operating at an accelerating voltage of 20 kV and equipped with an X-ray detector Oxford Penta Fet Precision for energy-dispersive X-ray spectroscopy (EDS) measurements. The specimen stub with conductive tape was used for the SEM of the powder sample. Initially, powder samples were pressed onto the surface of the conductive tape fixed on the surface of the sample stub and then the excess powder was blown off the surface of the conductive tape. Thus many powder samples were prepared for analysis.

2.4.3 Ultraviolet-Visible (UV-vis) Spectroscopy

Ultraviolet-visible spectroscopy is a quantitative technique that analyzes how much light is absorbed or reflected by a material. UV-vis spectroscopy can be accomplished by shining light through the material, where the recorded reflectance or absorption spectra are compared to a standard sample. In our experimental work, UV-vis diffuse reflectance spectra were obtained using Shimadzu UV-2600. The UV-vis spectra for all the samples were obtained in the wavelength range of 200 nm to 800 nm.

2.4.4 Brunner–Emmett–Teller (BET) analysis

Brunner-Emmett-Teller (BET) analysis is a technique used to measure the surface area of a material using the adsorption of gas molecules on its surface. BET was used to measure the surface area using Micromeritics Tristar 3000 with hydrogen absorption at 77 k. Initially, 350 mg of powder sample was placed in a sample holder and then all possible physically bound impurities were removed under vacuum and heating conditions. The surface area was measured by increasing the pressure and noting the amount of gas adsorbed on the surface.

2.4.5 Raman Spectroscopy

Raman spectroscopy is a technique used for the detection of vibrational, rotational, and other states in a system (molecular system), inquiring closely about the chemical composition of the

materials. In our experimental work, the Raman spectra were analyzed using Renishaw in Via Raman microscope equipped with double CCD cameras and Ar-Kr laser source of wavelength 514 nm. All samples were prepared for Raman analysis on glass slides, 40 mg of the $BiVO_4$ powder was placed on the glass slide and then slightly pressed.

2.4.6 X-ray Photoelectron Spectroscopy (XPS)

X-ray photoelectron spectroscopy was obtained to study the electronic chemical surface composition of all powder samples. A conventional spectrometer, Scientia Omicron ESCA+ with a high-performance hemisphere analyzer equipped with a monochromatic Al Kα source having energy equal to 1486.6 eV was used to analyze samples. A low-energy electron flood gun was used to reduce the charge effect in the samples. Scans were collected with a 50 eV pass energy with a step size of .05 eV to obtain high-resolution spectra. Samples were prepared on the specimen stub with conducting tape. Initially, the powder was placed on the stub, pressed, and then blown with air to remove excess powder from the surface. CasaXPS software was used to fit data, applying the peak shape of GL(30). All the peaks were calibrated with adventitious carbon (C-C 284.8 eV).

2.4.7 Transmission Electron Microscopy (TEM)

The Transmission Electron Microscopy analyses were performed using a JEOL JEM 2100F with a Gatan Tridiem 866 spectrometer coupled for Energy Electron Loss Spectroscopy (EELS) and an Oxford SSD detector coupled for Energy Dispersive Spectroscopy (EDS) studies. The crystalline structure and elemental mappings were investigated with scanning/transmission electron microscopy (S/TEM, FEI Talos F200X) and the energy dispersive spectroscopy unit (EDS, FEI ChemiSTEM®)

2.4.8 Flame Atomic Absorption Spectrometry Analysis

Sample preparation: 20 mg of each sample was weighed directly in PTFE microwave tubes (Xpress tubes from MARS6 microwave system) and then 2 ml of HCl and 1 ml of HNO_3 were added to each tube. The solution was heated up to 100 °C for 15 minutes and kept at this temperature for 15 minutes. Afterward, the samples were cooled down to room temperature

transferred to graduated polypropylene tubes, and volumized to 10 mL with ultra-purified water. The addition was done cautiously to avoid projections due to the heating of the water. Fully solubilized samples.

The sample was analyzed by Flame Atomic Absorption Spectrometry (FAAS) in a PerkinElmer-A Analyst 200 instrument (Figure 2.6), using hollow cathode lamps (LUMINATM Hollow Cathode Lamp -PerkinElmer)

Nickel determination: The nickel sample was analyzed in air-acetylene flame mode at flow rates of 10 and 2.5 L/min, respectively. The sample was introduced using a nebulizer system without using a spacer. The measurements were performed at a wavelength of 232 nm without the use of a background corrector (AA mode), using a 10 cm long burner.

Figure 2. 6. Flame Atomic Absorption Spectrometry.

2.4.9 Graphite Furnace Atomic Absorption Spectrometry Analysis

The samples were analyzed by Graphite Furnace Atomic Absorption Spectrometry (GFAAS) in a PerkinElmer - PinAAcle 900T instrument (Figure 2.7), using hollow cathode lamps (LUMINATM Hollow Cathode Lamp - PerkinElmer).

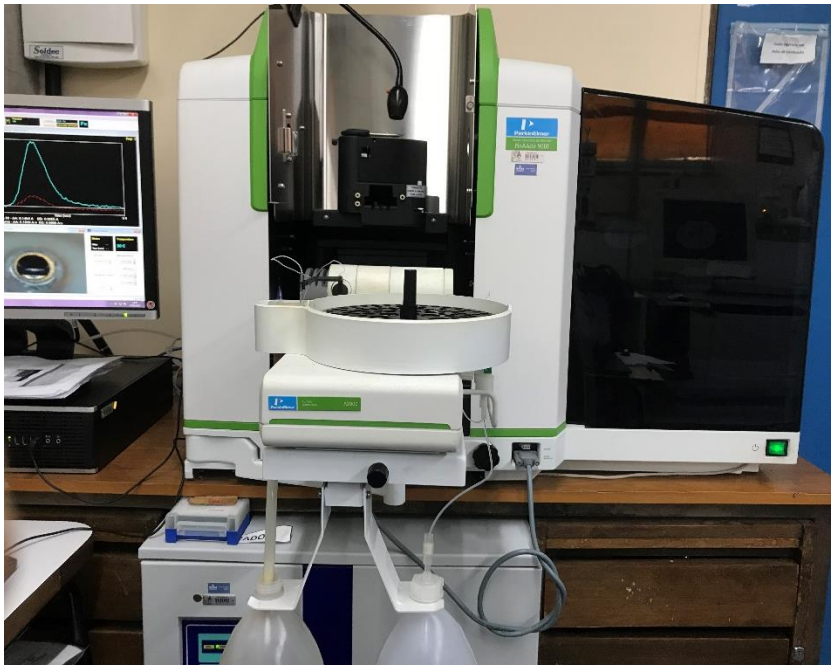

Figure 2. 7. Graphite Furnace Atomic Absorption Spectrometry.

Iron determination: **A** Graphite furnace (with platform) was used to analyze the sample that contained iron by injecting 20 uL of them by using a Furnace Autosampler (PerkinElmer - AS900). The measurements were performed at a wavelength of 248.33 nm with the use of Zeeman-effect as background corrector (AA-BG). All the measurements were performed under an argon atmosphere.

Manganese determination: The sample that contained manganese was analyzed in a graphite furnace (with platform) by injecting 20 uL of it by using a Furnace Autosampler (PerkinElmer - AS900)

2.5 Gas chromatography

The Agilent model 7890B, GC equipped with a thermal conductivity detector (TCD) was used in our project for the detection of oxygen as shown in Figure 2.8. The oxygen was injected into TCD through a pipe connected with the reactor and the evolved area of the oxygen was plotted through the computer system.

Figure 2. 8. Gas chromatograph (GC) equipped with a thermal conductivity detector.

2.6 Photocatalytic Oxygen Evolution

Photocatalytic oxygen was carried out in a closed quartz reactor having a volume of 90 ml. 25 mg of already prepared bismuth powders were dissolved in a 0.05M $FeNO_3$. $9H_2O$ (50 ml) aqueous solution. The solution was stirred for 15 min to make it homogenous and then purged argon gas for 15 min to remove dissolved gasses. A 300 W Xe lamp equipped with an AM 1.5 G filter was used as the light source, where the light intensity was adjusted to 246 mW/cm^2. The first measurement for oxygen evolution was taken in the absence of light and injected into the Agilent gas chromatograph model 7890B. The lamp was turned on and the quarts reactor was exposed to the light continuously for 3 h. The oxygen evolution was recorded after each 30 min while injecting

it into the chromatograph automatically using a narrow steel pipe. The produced oxygen was carried from the reactor to the gas chromatograph using argon gas with a constant flow of 0.9 mL min^{-1}. The gas chromatograph was connected to the computer system, where through software the area of the evolved oxygen was recorded. The photocatalytic process used in our research work is given in Figure 2.9.

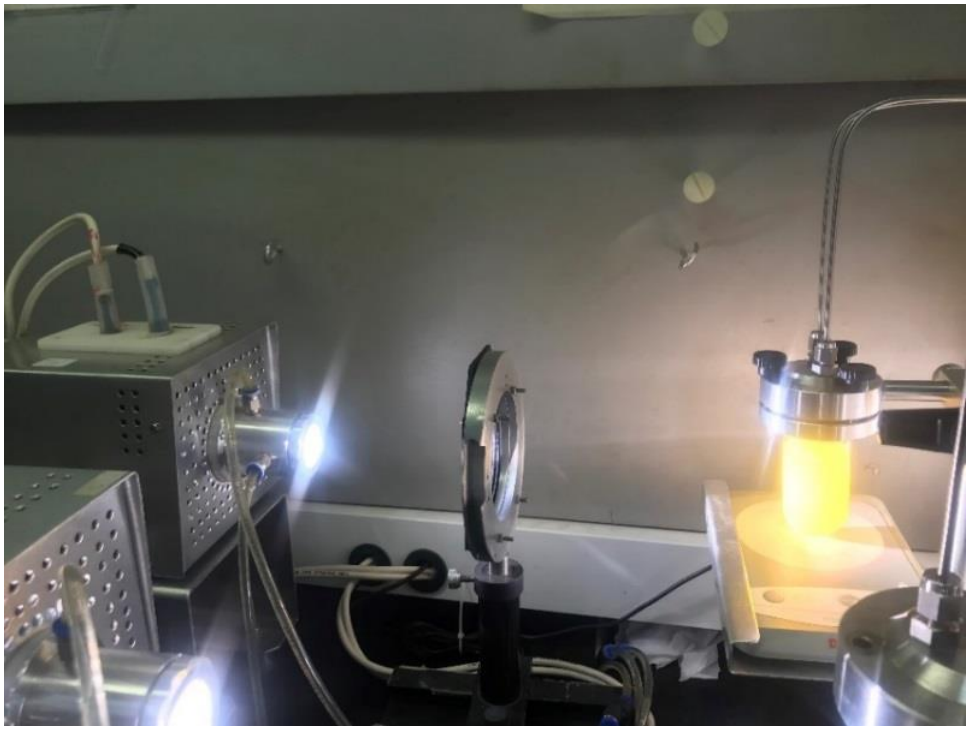

Figure 2. 9. Photocatalytic oxygen evolution, irradiating the sample with a 300 W Xe lamp with an AM 1.5 G filter.

2.7 Mott- Schottky analysis

Mott–Schottky (MS) measurements were performed with a conventional three-electrode system, where the W:BVO (or pure $FeNiO_x$, pure $FeMnO_x$, W:BVO/ $FeNiO_x$ and W:BVO/ $FeMnO_x$) film is the working electrode, Pt foil is the counter-electrode, and Ag/AgCl is the reference electrode. All measurements were conducted at the 0.1 M potassium phosphate buffer (pH 7), at 1 kHz in dark conditions (i.e., without illumination), using a suitable range of potentials to determine flat-band potentials and dopant density. The MS equation for *n*-type and *p*-type semiconductors is given in equations 2.1 and 2.2 [99,100]:

$$\frac{1}{C_{SC}^2} = \frac{2}{eA^2\epsilon_r\epsilon_0 N_D}\left(E - E_{FB} - \frac{kT}{e}\right), \qquad \text{n} - \text{type} \tag{2.1}$$

$$\frac{1}{C_{SC}^2} = \frac{2}{eA^2\epsilon_r\epsilon_0 N_A}\left(-E + E_{FB} - \frac{kT}{e}\right), \qquad \text{p} - \text{type} \tag{2.2}$$

where C_{SC} is the total capacitance in the space-charge depletion layer, ϵ_0 is the permittivity in the vacuum, ϵ_r is the relative permittivity of the semiconductor (ϵ_r = 68, 13, and 18 for W:BVO [101], $FeNiO_x$ [102], and $FeMnO_x$ [103] semiconductors, respectively), A is the surface area of the working electrode, E is the applied potential, E_{FB} is the flat-band potential, N_D is the donor carrier density, N_A is the acceptor carrier density, and T is the temperature. The majority carrier densities are calculated from the slopes, whereas E_{FB} is determined from the x-intercept of the C_{SC}^{-2} versus E.

2.8 Band Bending Model for p-n Heterojunction

The details for constructing interfacial band alignment of *p-n* heterojunctions are described elsewhere [104–107]. Briefly, consider a *p-n* heterojunction whose interface is at the point $x = 0$, with the *n*-type semiconductor situated at $x \leq 0$ and the *p*-type semiconductor at $x \geq 0$. Let N_A, W_p, and $\epsilon_{r,p}$ represent the acceptor density, depletion width, and dielectric constant on the p-side, while N_d, W_n, and $\epsilon_{r,n}$ are the donor density, depletion width, and dielectric constant on the *n*-side. The conduction band energy for the n-type (p-type) layer is given by $E_{C,n(p)}$. The solution for the one-dimensional Poisson equation describing this abrupt *n-p* heterojunction, with the proper boundary conditions, is:

$$E_C(x) = \begin{cases} E_{C,n} + qV_n, x < -W_n \\ E_{C,n} + qV_n - \dfrac{qN_D}{2\epsilon_0\epsilon_{r,n}}(x + W_n)^2, -W_n \leq x < 0 \\ E_{C,p} - qV_p + \dfrac{qN_A}{2\epsilon_0\epsilon_{r,p}}\left(x - W_p\right)^2, 0 \leq x < W_p \\ E_{C,p} - qV_p, x > W_p \end{cases} \tag{3.5}$$

Where $E_C(x)$ is the conduction band energy given as a function of position, and V_n and V_p are the potential drops supported in the *n* and *p* layers, respectively, given as a function of the dopant concentrations and dielectric constants by:

$$V_n = \frac{N_D W_n^2}{2\epsilon_0 \epsilon_{r,n}} = \frac{\epsilon_{r,p} N_A}{q(\epsilon_{r,p} N_A + \epsilon_{r,n} N_D)} V_{bi} \text{ and } V_p = \frac{N_A {W_p}^2}{2\epsilon_0 \epsilon_{r,n}} = \frac{\epsilon_{r,n} N_D}{q(\epsilon_{r,p} N_A + \epsilon_{r,n} N_A)} V_{bi}$$

Here, V_{bi} is the total interfacial potential drop, defined as:

$$V_{bi} = V(-W_n) - V(W_p) = V_n + V_p = E_{F,n} - E_{F,p}$$

Where $E_{F,p}$ and $E_{F,p}$ are the Fermi energies of the p and n-type semiconductors, respectively. Similarly, the depletion width of the n and p-type semiconductors are given by:

$$W_n = \left(\frac{2\epsilon_0 \epsilon_{r,n} N_A V_1}{q N_D} \left(\frac{1}{N_A + N_D} \right) \right)^{1/2} \text{ and } W_p = \left(\frac{2\epsilon_0 \epsilon_{r,n} N_D \psi_{bi}}{N_A(\epsilon_{r,p} N_A + \epsilon_{r,n} N_D} \right)^{1/2}$$

The discontinuities of the valence and conduction bands (ΔE_V and ΔE_C) must be invariant after equilibrium since bandgap energies and electronic affinities are considered constants in the classical band bending model.

The distribution of the electric field ($\xi(x)$) can be obtained through the (minus) first derivative of the electrostatic potential. It is straightforward to show that:

$$\xi(x) = \begin{cases} \frac{qN_D}{\epsilon_0 \epsilon_{r,n}}(x + W_n), -W_n \leq x < 0 \\ \frac{-qN_A}{\epsilon_0 \epsilon_{r,p}}(x - W_p), 0 \leq x < W_p \end{cases} \quad (3.6)$$

Therefore, the built-in electric field developed on the space charge region has its maximum value at the point where the junction occurs ($x = 0$), which is:

$$|\xi_{max}| = \frac{qN_D W_n}{\epsilon_0 \epsilon_{r,n}} = \frac{qN_A W_p}{\epsilon_0 \epsilon_{r,p}}, \quad (3.7)$$

Confirming that higher values of depletion widths (and therefore, potential drops) result in more intense built-in electric fields.

2.9 Computational details

All calculations were performed using QUANTUM ESPRESSO density functional theory (DFT) software and the crystal structure model was constructed in VESTA and AVOGADRO software [108]. The clinobisvanite structure of $BiVO_4$ having symmetry group of *I2/b* with the lattice parameters of a=5.147Å, b=5.147Å, c=11.7216 Å and $\gamma = 90^0$ and the bond distances of 2.443 Å (Bi-O), 2.488Å (Bi-O), 1.738 Å (V-O), 3.900 Å (Bi-Bi) and 3.900 Å (V-V) was used [109–111]. In our model, the basic unit cell of $BiVO_4$ consists of 24 atoms: 4 atoms from bismuth, 4 atoms from vanadium, and 16 atoms from oxygen. Keeping the impurity concentrations equals to 4.16% (atomic fraction), we have replaced one V atom with one Zn atom. The primitive unit cell 1x1x1 was optimized by using the ultra-soft pseudopotentials of plan wave basis set with cutoff energy 500 eV. The adsorption of FeMn cocatalysts was performed by creating a vacuum 20 Å along the y-direction for the study of the periodic boundary condition. The Generalized gradient approximation (GGA) at Perdew-Burke-Ernzerhof (PBE) exchange-correlation functional was used for the structural and energy optimization calculation [112]. The Monkhorst-pack scheme k-points grid sampling was set as $5 \times 5 \times 1$ for the irreducible Brillouin zone. To get reasonable results, the lattice parameters and atomic coordinates were first optimized by the minimum total energy and atomic forces. The charge density difference for Zn-doped $BiVO_4$ and Zn-doped $BiVO_4$ loaded with bimetallic FeMn cocatalysts was obtained from equation $\Delta\rho = \rho_{total} - \rho_{Zn} - \rho_{FeMn}$, where ρ_{total} is representing the charge density of bimetallic adsorption on Zn doped BiVO4, ρ_{Zn} is charge density of Zn doped $BiVO_4$, and ρ_{FeMn} is the charges density of FeMn [113].

3. Tungsten (W) doped $BiVO_4$: Results and discussion

3.1 X-ray diffraction (XRD) pattern of Powder Samples

3.1.1 X-ray diffraction (XRD) pattern of W-doped $BiVO_4$

X-ray diffraction pattern of pure and W-doped BVO samples are shown in Figure 3.1, where all peaks of the XRD plot are in good agreement with JCPDS (Card No. 14-0688, space group: I2/a, a = 5.195, b = 11.701, c = 5.092, b = 90.38) and correspond to the monoclinic scheelite (m-s) phase of $BiVO_4$ [114]. The monoclinic scheelite (m-s) phase generally shows well splitting of peak at 2θ ~18.7°, 35 °, and 46° [115,116] . There were no extra peaks observed in the XRD plot for both BVO and W-doped BVO. The peak positions around 2θ~18.7 °, 28.8 °, and 30.55 ° in doped and undoped samples correspond to (110), (121), and (040) facets. If we compare the (040) peak at around 2θ~30.55° for pure BVO and W:BVO, the peak is more intense in W:BVO than pure BVO which shows growth towards the (040) direction.

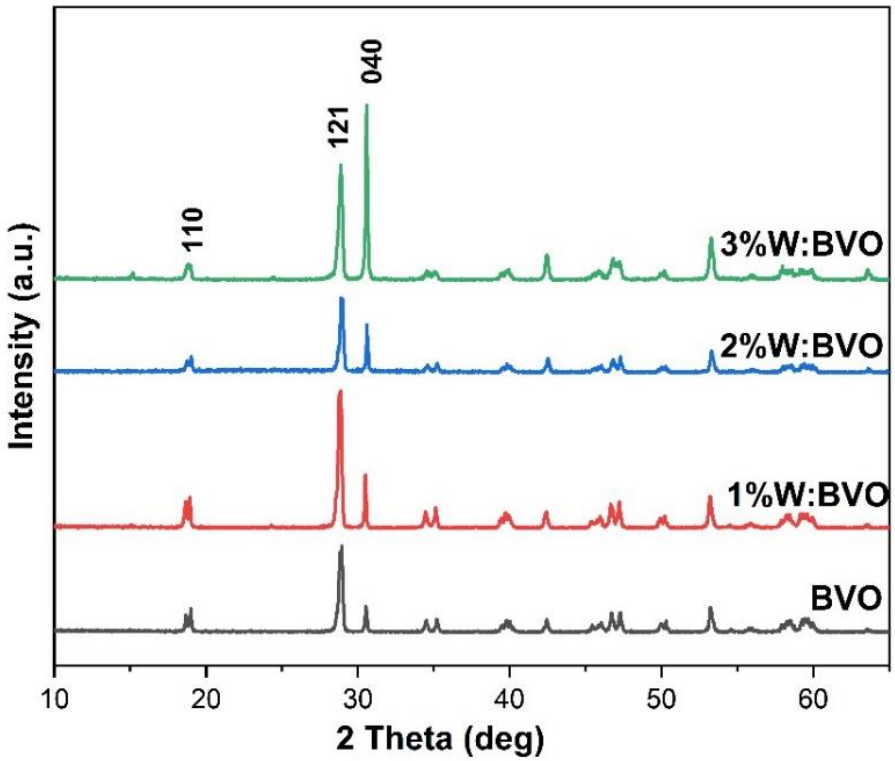

Figure 3. 1. XRD pattern of all $BiVO_4$ powder samples doped with 1%, 2%, and 3% tungsten (W) showing a trend towards 040 direction.

The growth towards the (040) facet can be confirmed from the ratio (040/110) facets, which increased for the W:BVO sample as compared to the BVO [117]. The growth was found to increase towards the (040) direction because of the increasing concentration of W dopant. Therefore increasing the concentration of dopants at a particular doping site can increase the atomic scattering factor leading to an increase in intensity at a particular site. Furthermore, the 121 peak for W:BVO shifted to lower angles which could be due to larger ionic radii of W [118]. The shift towards lower angles can be explained by the different sizes of ionic radii of W (0.65 Å) and V (0.54 Å). The larger ionic radii of the W dopant helped to enlarge the crystal lattice which further led to the shift (Figure 3.2).

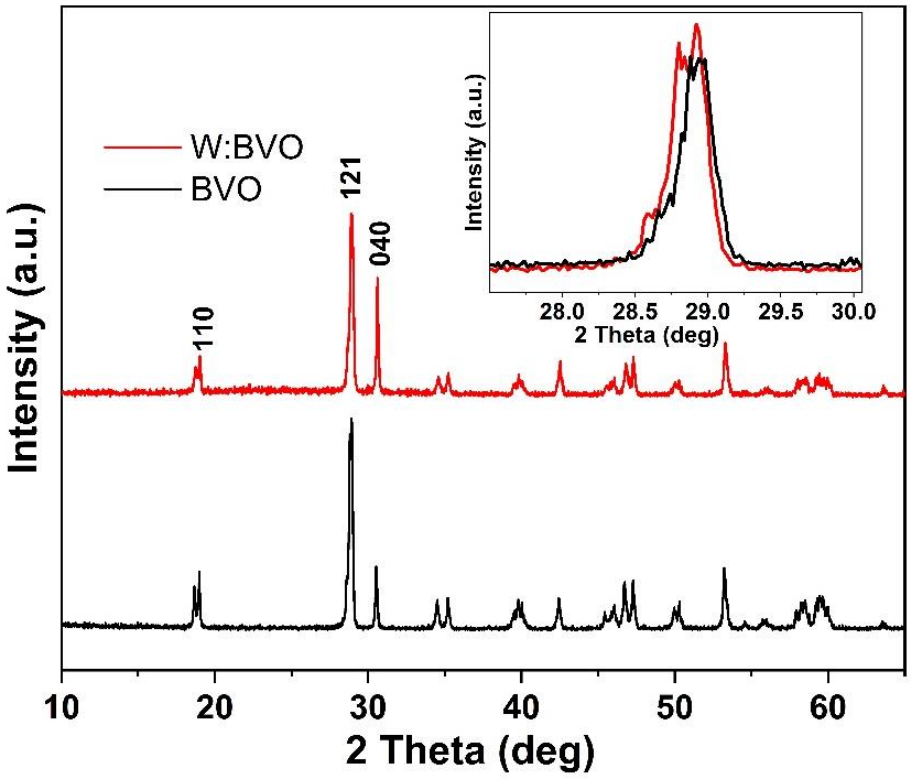

Figure 3. 2. XRD pattern of all $BiVO_4$ powder samples doped with 2%, tungsten (W) showing a shift toward lower angle.

The Scherer equation was used to calculate the crystallite size of all samples [119].

$$D = \frac{K\lambda}{\beta \cos\theta} \quad (3.1)$$

Where D is the crystallite size in nanometers, λ is the x-ray wavelength (0.15418 nm), K and β are represent the shape factor and the peak width at half of the maximum. The crystallite size was also calculated for each sample using the highest peak (121) in the XRD data as shown in Table 3.1 which increased for W-doped $BiVO_4$. The crystallinity of the W-doped samples was also calculated which was determined from XRD scans primarily by forming an amorphous halo to separate the crystalline peaks from amorphous scattering, and calculating the ratio of the crystalline peak areas to the total area [120]. The improved crystallinity (Table 3.1) was observed for W-doped $BiVO_4$ when compared to pure $BiVO_4$.

Table 3.1 Crystalline (based on XRD analyses) and morphological (based on SEM images) properties of pure $BiVO_4$ and W-doped $BiVO_4$.

S.NO	Sample	Crystallite size (nm)	Crystallinity (100%)	Particle size length (nm)	Particle size width (nm)
1	BVO	27.0	65	620 ± 15	300 ± 08
2	1%W: BVO	28.9	68	625 ± 13	300 ±09
3	2%W: BVO	29.2	79	500 ± 16	278 ± 10
4	3%W: BVO	30.9	76	295 ± 10	295 ± 09

3.1.2 X-ray diffraction (XRD) pattern of pure $BiVO_4$ loaded with $FeMnO_x$ and $FeNiO_x$ cocatalysts

The x-ray diffraction spectra of pure $BiVO_4$ loaded with $FeMnO_x$ and $FeNiO_x$ cocatalysts are shown in Figure 3.3, which were measured at the same conditions used for W-doped $BiVO_4$. All the samples represented the characteristic peaks of the monoclinic scheelite $BiVO_4$. The XRD peaks for samples loaded with $FeMnO_x$ and $FeNiO_x$ cocatalysts were found similar to the pure $BiVO_4$. The similar XRD peaks for these samples were because of the lower contents of the $FeMnO_x$ and $FeNiO_x$ cocatalysts at the surface of $BiVO_4$.

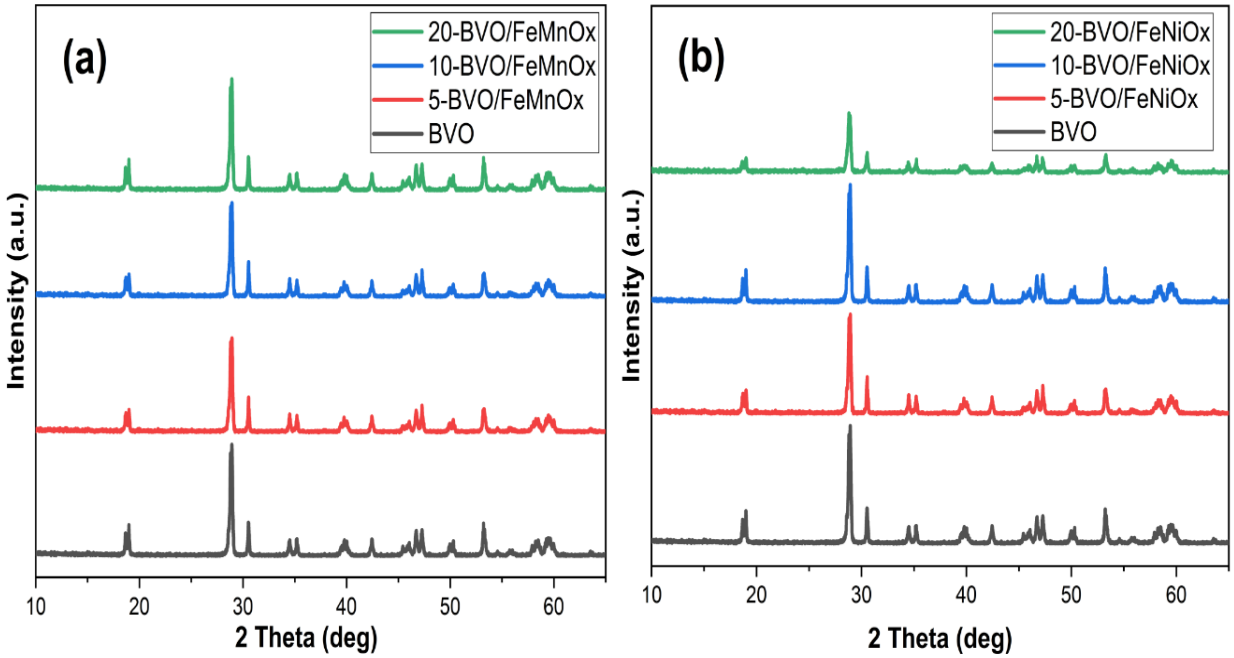

Figure 3. 3. XRD pattern of $BiVO_4$ loaded with cocatalysts i.e. (a) $FeMnO_x$ and (b) $FeNiO_x$ via RF magnetron sputtering deposition for 5,10, and 20 min.

3.1.3 X-ray diffraction (XRD) pattern of 2% tungsten (W) $BiVO_4$ loaded with $FeMnO_x$ and $FeNiO_x$ cocatalysts

X-ray diffraction pattern of 2% tungsten (W) doped $BiVO_4$ sample loaded with $FeMnO_x$ and $FeNiO_x$ cocatalysts were also analyzed using the above conditions. The RF magnetron sputtering deposition time for the cocatalysts was set to 10 min which is based on the oxygen evolution test (Figure 3.18c). It was found that all the W-doped $BiVO_4$ samples loaded with $FeMnO_x$ and $FeNiO_x$ cocatalysts have monoclinic phases and there were no extra peaks that appeared in the XRD pattern. The similar XRD spectra of these samples were because of the lower contents of $FeMnO_x$ and $FeNiO_x$ cocatalysts at the surface of W-doped $BiVO_4$. In short, the XRD pattern was not changed after loading a small amount of $FeMnO_x$ and $FeNiO_x$ cocatalysts and was found similar to 2%W-doped $BiVO_4$. The XRD pattern of W-doped $BiVO_4$ loaded with $FeMnO_x$ and $FeNiO_x$ cocatalysts is shown in Figure 3.4 and the corresponding crystallinity and crystallite size are shown in Table 3.2.

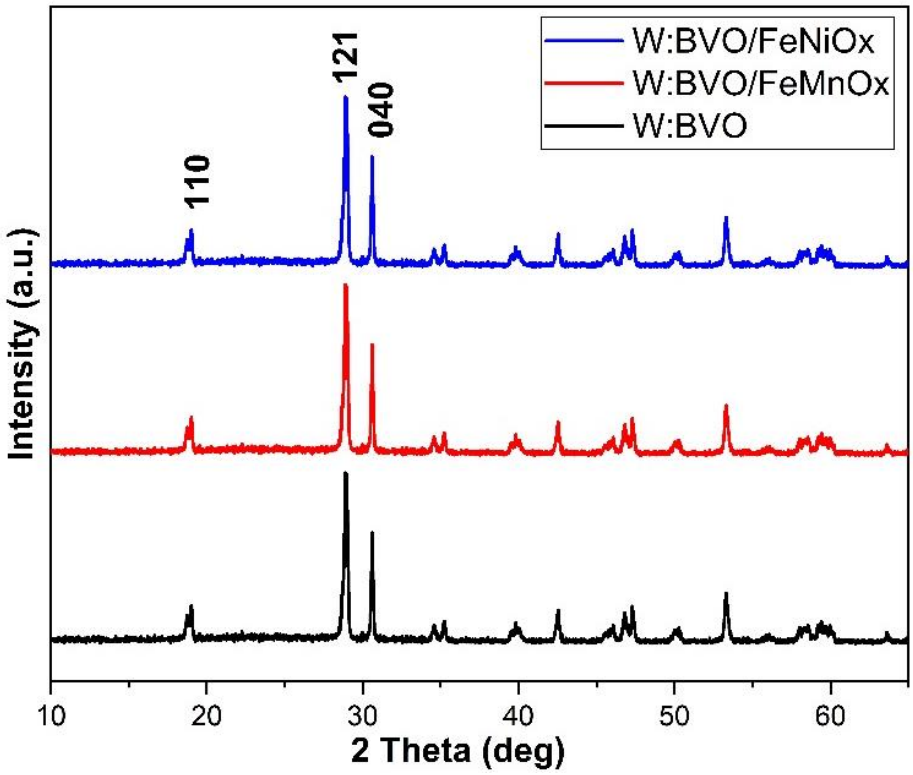

Figure 3. 4 XRD pattern of 2% tungsten (W) doped $BiVO_4$ loaded with $FeMnO_x$ and $FeNiO_x$ cocatalysts via RF magnetron sputtering deposition for 10 min.

Table 3.2 Crystalline (based on XRD analysis) and morphological (based on SEM images) properties of 2%W-doped $BiVO_4$ loaded with FeMnOx and $FeNiO_x$ cocatalysts.

S.NO	Sample	Crystallite size (nm)	Crystallinity (100%)	Particle size (nm)
1	W:BVO	29.3	79	293
2	W:BVO/$FeNiO_x$	29.0	79	296
3	W:BVO/$FeMnO_x$	29.2	79	293

3.2 Raman spectroscopy

Raman spectroscopy is an effective and easy tool to elucidate the bonding state and the local structure of the semiconductor. Herein it was performed to further confirm the tungsten (W) dopant sites and the $FeMnO_x$ and $FeNiO_x$ deposition on pure and W-doped BVO. The vibrational bands at ~330, 373, and 826 cm^{-1} were observed in all samples. The bands at 330 and 373 cm^{-1} were

assigned to the asymmetric and bending vibration of VO_4^{-3} units, and the band around 826 cm^{-1} was assigned to the V-O bond length [92].

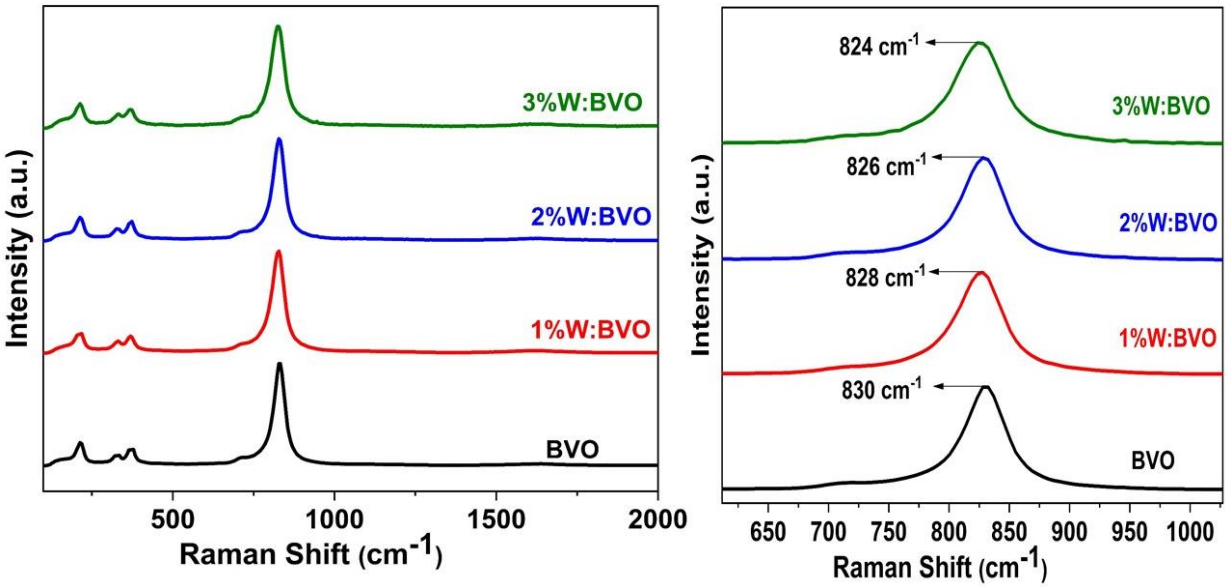

Figure 3. 5. Raman spectra of all $BiVO_4$ powder samples doped with 1%, 2%, and 3% tungsten (W).

3.2.1 Raman spectroscopy of W-doped $BiVO_4$.

Raman spectra of all tungsten (W) doped samples are shown in Figure 3.5, where the major peak in Raman spectra was shifted to the lower wave number as compared to BVO. The Raman spectra were shifted to a lower wave number according to the percentage of W dopants in $BiVO_4$. This shift in Raman spectra is related to the V-O bond length, which was calculated using equation 3.2. The wavenumber for the pure BVO (830 cm^{-1}) corresponded to the bond lengths of 1.6939 Å which were increased for the W-doped $BiVO_4$ samples as shown in Table 3.3. The increase in V-O bond length values for the W-doped $BiVO_4$ samples can be related to the crystallinity which was higher for the W-doped $BiVO_4$ than BVO.

$$\upsilon\ (cm^{-1}) = 21349 \exp(-1.9176\ R(Å)) \qquad (3.2)$$

Table 3.3 Raman shift, bond length, and bandgap based on Raman and UV-vis analysis.

S.No	Samples	Raman shift (cm^{-1})	Bond length (Å)	Bandgap (eV)
1	BVO	830	1.6939	2.41
2	1%W: BVO	828	1.6952	2.38
3	2%W: BVO	826	1.6964	2.36
4	3%W: BVO	824	1.6977	2.35

3.2.2 Raman spectroscopy of pure $BiVO_4$ loaded with $FeMnO_x$ and $FeNiO_x$ cocatalysts

The Raman spectra of the pure $BiVO_4$ loaded with bimetallic cocatalysts ($FeMnO_x$ and $FeNiO_x$) were also obtained as shown in Figure 3.6. The vibrational bands at ~330, 373, and 826 cm^{-1}were observed in all samples but no obvious shifts were observed for the pure $BiVO_4$ loaded $FeMnO_x$ and $FeNiO_x$. The wave numbers for the samples with cocatalysts were found similar to that of pure $BiVO_4$. The similar Raman spectra value is probably due to the lower amount of cocatalysts at the surface of the $BiVO_4$.

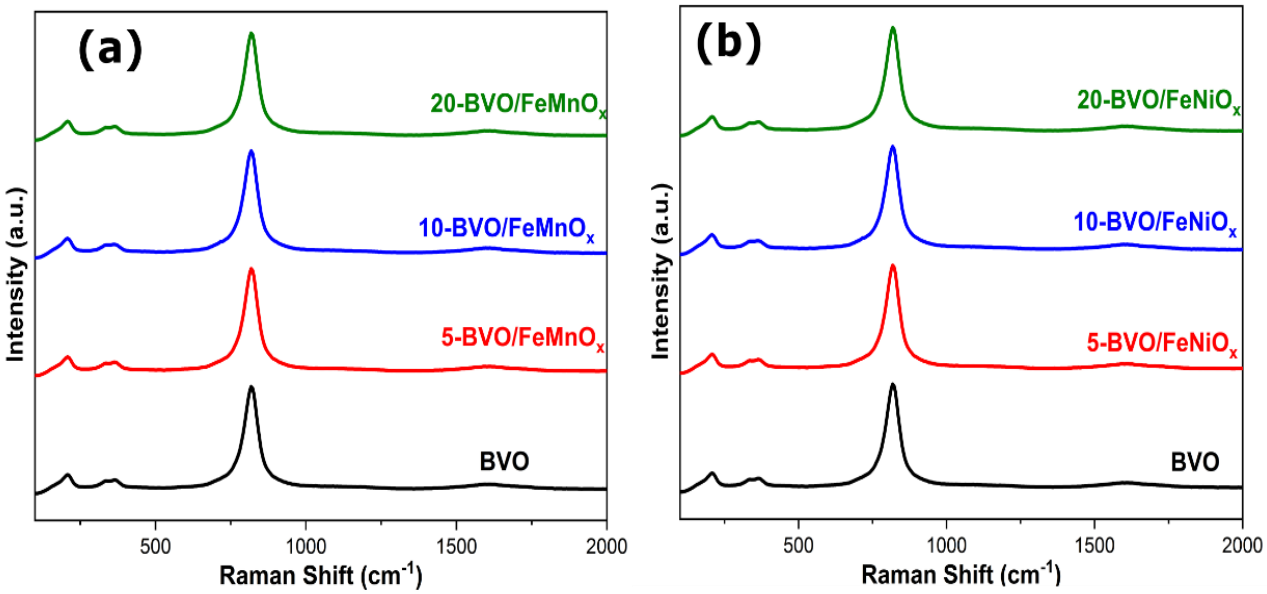

Figure 3. 6. Raman spectra of all $BiVO_4$ powder samples loaded with $FeMnO_x$ and $FeNiO_x$.

3.2.3 Raman spectroscopy of 2% W-doped $BiVO_4$ loaded with $FeMnO_x$ and $FeNiO_x$ cocatalysts

The Raman spectra of 2% W-doped $BiVO_4$ samples were analyzed using the same parameters as shown in Figure 3.7. The specific vibrational bands at ~330, 373, and 826 cm^{-1} were observed. The Raman spectra of all 2% W-doped $BiVO_4$ loaded with $FeMnO_x$ and $FeNiO_x$ cocatalysts are similar to that of 2% W-doped $BiVO_4$ (W:BVO). The major peak in the Raman spectra corresponds to the wave number of 826 cm^{-1}, which corresponds to a V-O bond length of 1.6964 Å. The reason for the similar spectra of W:BVO/ $FeMnO_x$ and W:BVO/ $FeNiO_x$ samples to W:BVO is due to the lower content of $FeMnO_x$ and $FeNiO_x$ at the surface of W-doped $BiVO_4$. Our results are consistent with the previous research work, where they have deposited Ni nanoparticles over $NaTaO_3$ semiconductor using different deposition times i.e. 5, 10, and 20 min. They have found that Raman spectra remain the same after the deposition of nanoparticles [121].

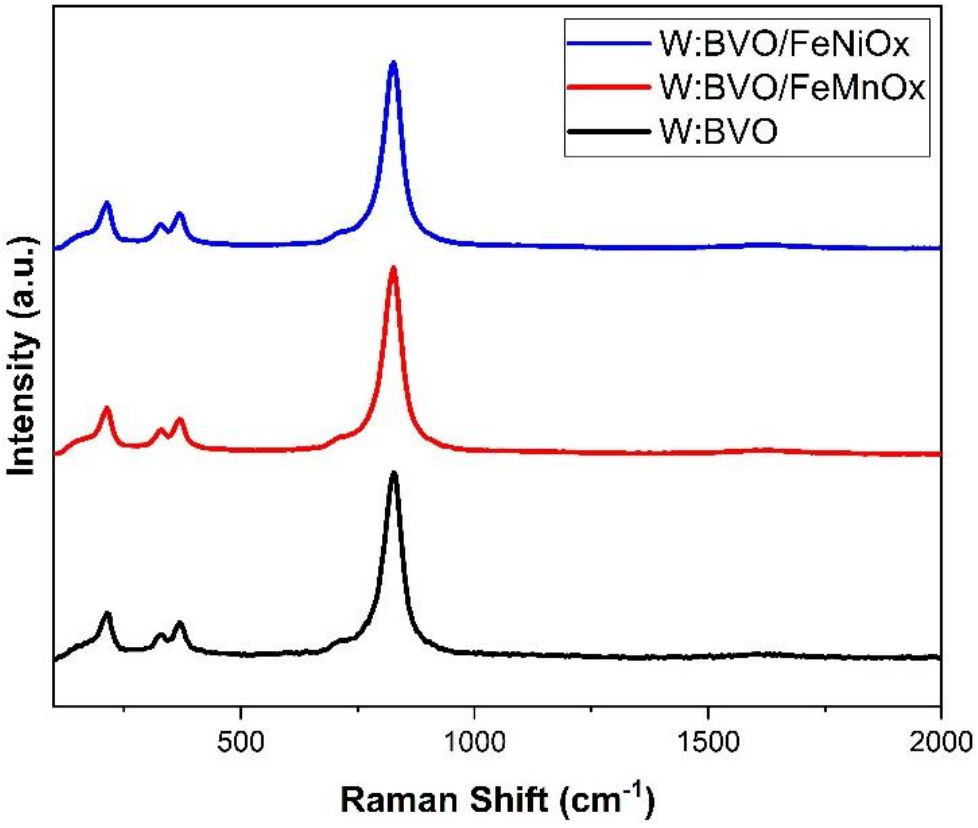

Figure 3. 7. Raman spectra of W-doped $BiVO_4$ powder samples loaded with $FeMnO_x$ and $FeNiO_x$.

3.3 Scanning electron microscopy (SEM) of pure and W-doped $BiVO_4$

The morphology of all samples was confirmed using scanning electron microscopy (SEM) as shown in Figure 3.8 and the concern particle sizes are shown in Table 3.1. The pure BVO shows a group of particles joined together having rod-like morphology. The rod-like particle has an average length and width of 620 and 300 nm respectively. The morphology of the pure $BiVO_4$ changed with increasing concentrations of W dopants. The 1%W:BVO shows a similar particle size (length 625 and width 300) to that of pure BVO but particles are more bounded together. Similarly, 2% W doped $BiVO_4$ shows a different morphology than the pure with a reduced particle size (length 500, and width 278 nm), and also particles are attached in branches making a leaf-like morphology. The leaf-like morphology was found more visible in the 3 % W doped $BiVO_4$. The 3% W doping in $BiVO_4$ changed the morphology to leaf-like morphology, where the length and width of each particle is about 295 nm [115,122,123].

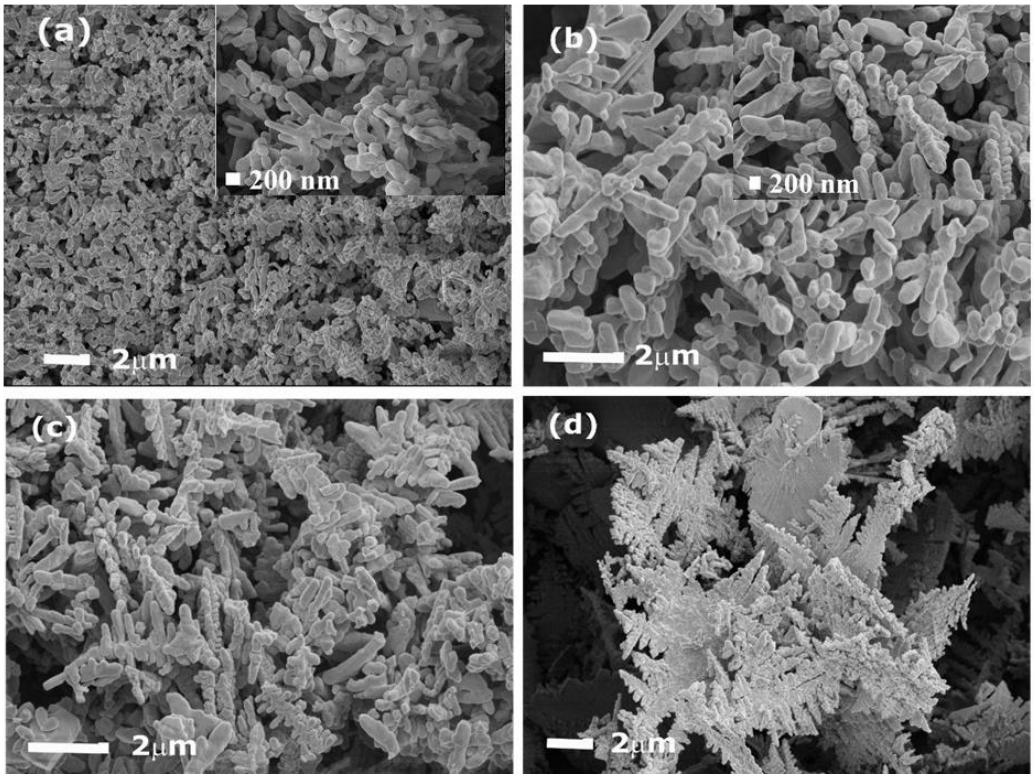

Figure 3. 8. Scanning electron microscopy images of (a) pure (b) 1%W (c) 2%W, and (d) 3%W doped $BiVO_4$, representing different morphology with reduced particle sizes. The inset in Figures 1a and 1b displays the high-resolution SEM images of BVO and W:BVO, respectively.

The elements mapping and the elemental compositions were also obtained from the EDX (Figure 3.9 and Figure 3.10). The elemental mapping result has shown the uniform distribution of Bi, V, and O, and also the uniform distribution of tungsten (W) elements on $BiVO_4$.

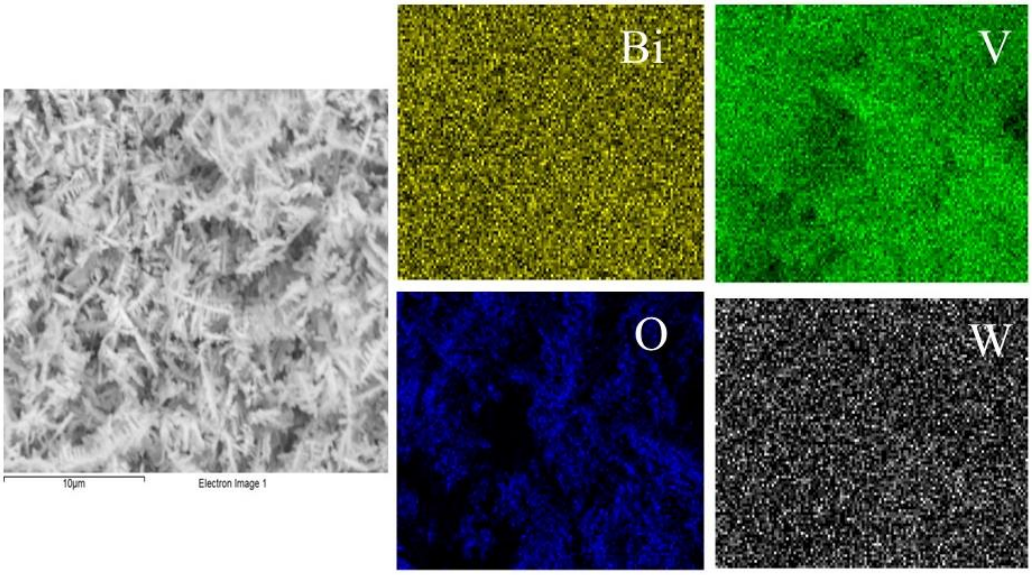

Figure 3. 9. Elemental mapping of W-doped $BiVO_4$, showing the uniform distribution of Bi, V, O, and tungsten (W).

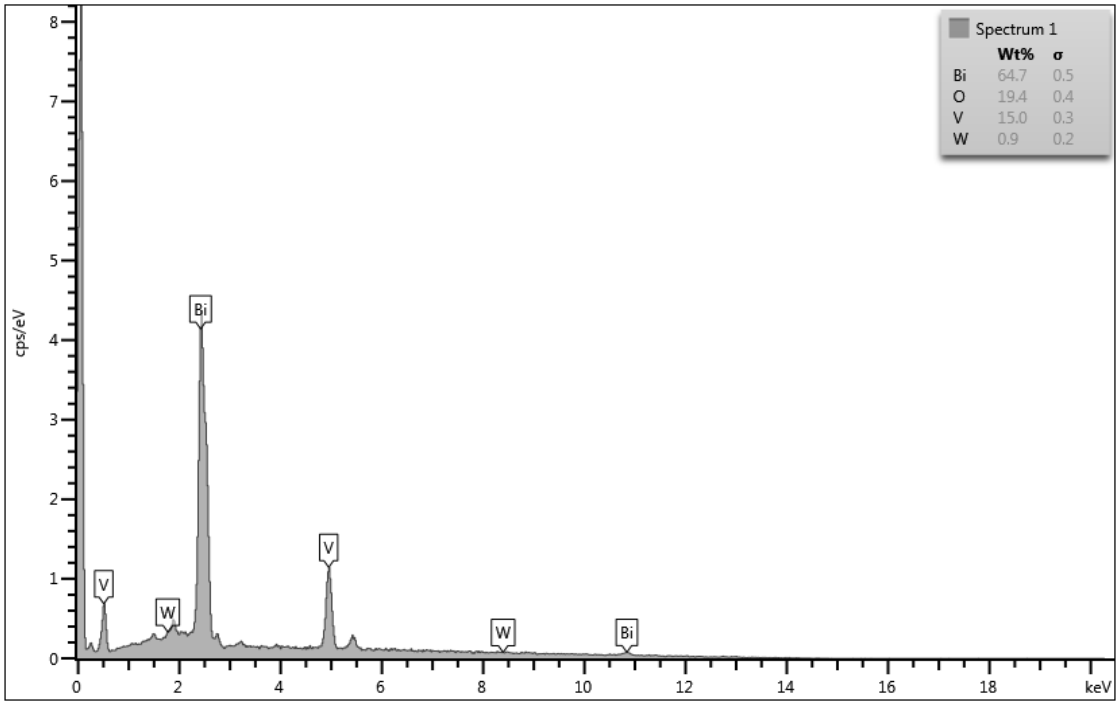

Figure 3. 10. EDS of 2% W doped $BiVO_4$ showing Bi, V, and W peaks.

3.3.1 Scanning electron microscopy (SEM) of pure and 2% W-doped $BiVO_4$ loaded with $FeMnO_x$ and $FeNiO_x$ cocatalysts.

The morphology of the samples loaded with $FeMnO_x$ and $FeNiO_x$ cocatalysts was also analyzed as shown in Figure 3.11. The morphologies of the samples loaded with cocatalysts were found similar to those of pure BVO and W:BVO. The similar morphologies of these samples were obtained because of the lower contents of the $FeMnO_x$ and $FeNiO_x$ cocatalysts. The small amount of $FeMnO_x$ and $FeNiO_x$ does not lead to a clear change in the morphology of the pure and W-doped $BiVO_4$, therefore revealing the same morphological properties.

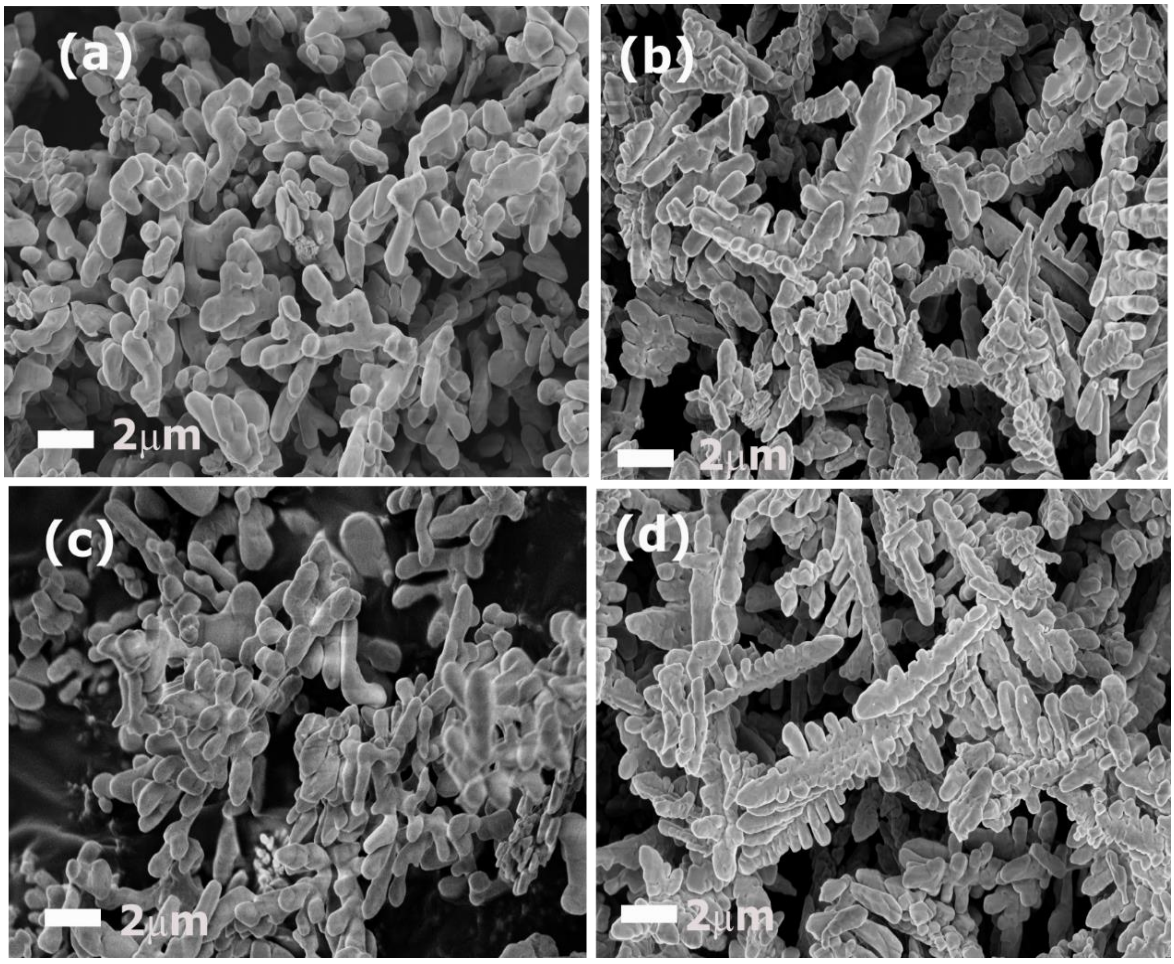

Figure 3. 11. Scanning electron microscopy images of the (a) pure BVO loaded with $FeMnO_x$ (b) 2%W doped BVO loaded with $FeMnO_x$, (c) pure loaded with $FeNiO_x$, and (d) 2%W doped BVO loaded with $FeNiO_x$ cocatalysts.

3.4 UV-vis diffuse reflectance spectra

3.4.1 UV-vis diffuse reflectance spectra of W-doped $BiVO_4$

The optical properties of pure and W-doped $BiVO_4$ powder samples were determined from UV-vis diffuse reflectance spectra where the band energies were calculated from the Tauc plots (Figure 3.12). The UV-vis diffuse reflectance spectra of pure and W-doped $BiVO_4$ exhibit strong absorption in the visible region, which further clarifies that all the photocatalytic samples are operational upon visible light irradiations. The corresponding band energies of 1% W:BVO, 2% W:BVO, and 3%W:BVO were calculated from the Tauc plots which are shown in Table 3.2. The band gap energies of the W doping in $BiVO_4$ samples were red-shifted as compared to the as-prepared $BiVO_4$. The band gap energies decreased from 2.41 eV to 2.35 eV in the case of pure BVO and 3%W:BVO.

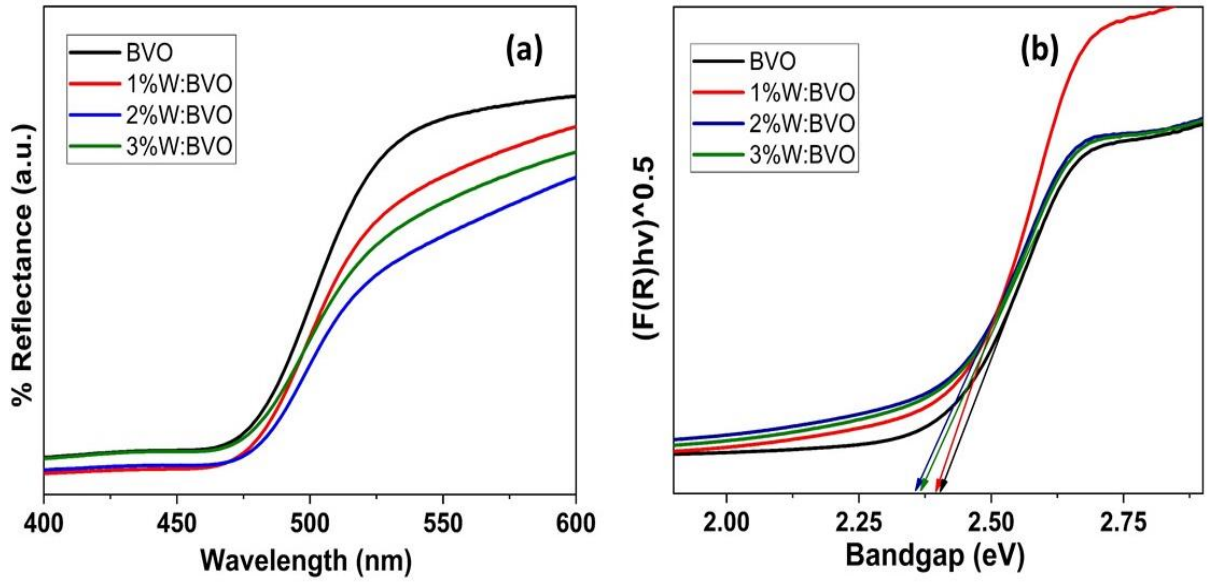

Figure 3. 12. (a) UV-vis diffuse reflectance spectra and (b) Bandgap energies of 1%W, 2%W, and 3%W doped $BiVO_4$ powder sample are compared to pure $BiVO_4$, which were obtained using the Kubelka-Munk transformation of defused reflectance spectra of the samples. The reflectance spectra of the W-doped $BiVO_4$ samples correspond to higher wavelengths which leads to the redshift in the band gap energies.

This red shift in the band gap of W-doped $BiVO_4$ is due to the formation of intraband states and the photon absorbance increased due to the formation of an intraband [92]. There are other

several reasons for the redshift in binding energies: (1) the first reason, charge transfer transition can be in between the metallic ions and valence/conduction band, (2) the second reason for the redshift is the addition of impurities to the band gap after doping. Moreover, doping in $BiVO_4$, distorted the lattice which resulted in rising defects, and led to breaks in the periodicity; thus, decreasing the band gap energy [124].

3.4.2 UV-vis diffuse reflectance spectra of pure and W-doped $BiVO_4$ loaded with $FeMnO_x$ and $FeNiO_x$ cocatalysts

The UV-vis diffuse reflectance spectra of the pure and W-doped $BiVO_4$ loaded with $FeMnO_x$ and $FeNiO_x$ co-catalysts are shown in Figure 3.13. The band gap energies of the pure and W-doped $BiVO_4$ remain the same after the deposition of $FeMnO_x$ and $FeNiO_x$ cocatalysts.

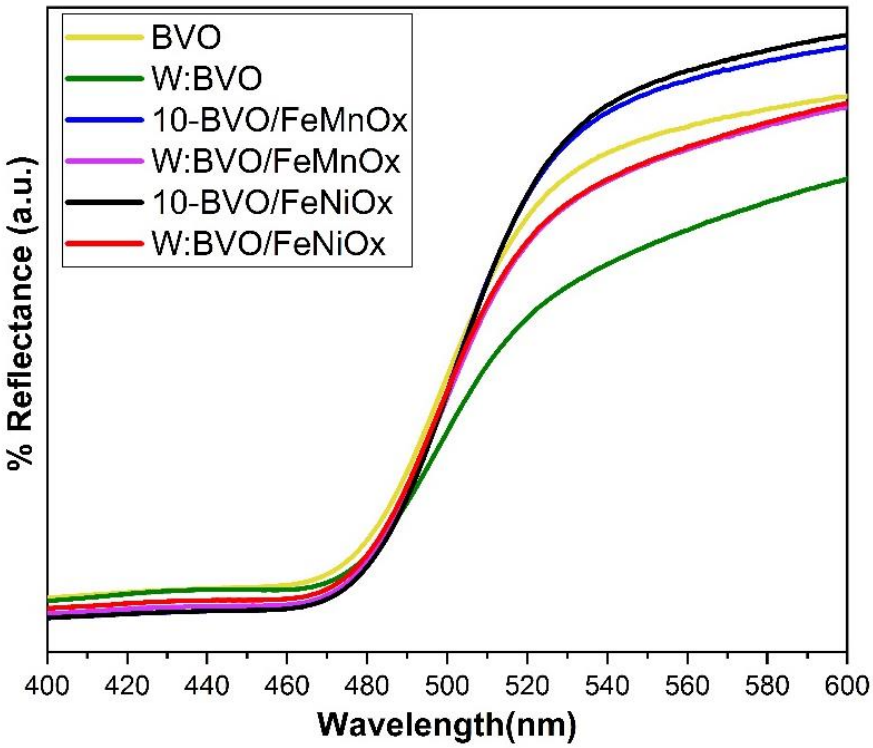

Figure 3. 13. UV-vis diffuse reflectance spectra of pure and W-doped $BiVO_4$ loaded with $FeMnO_x$ and $FeNiO_x$ cocatalysts via sputtering deposition for 10 min, where cocatalysts deposit on pure $BiVO_4$ shows no change in the reflectance spectra and for the W doped $BiVO_4$ reflectance correspond to higher wavelengths which is because of the W dopants.

Shortly, the deposition of cocatalysts at the surface of pure and W-doped $BiVO_4$ does not explicitly change the reflectance spectra; therefore leads to the same bandgap energies (Figure 3.13A). The

reason for no change in the band energies is because of the lower contents of the $FeMnO_x$ and $FeNiO_x$ at the surface of $BiVO_4$. Previously, $FeNiO_x$ and $FeCoO_x$ were used as cocatalysts on semiconductors via magnetron sputtering for a shorter time, which did not change the band energies of the semiconductor [125]. Thus, $FeMnO_x$ and $FeNiO_x$ co-catalyst deposition does not change the reflectance spectra of the pure and W-doped $BiVO_4$.

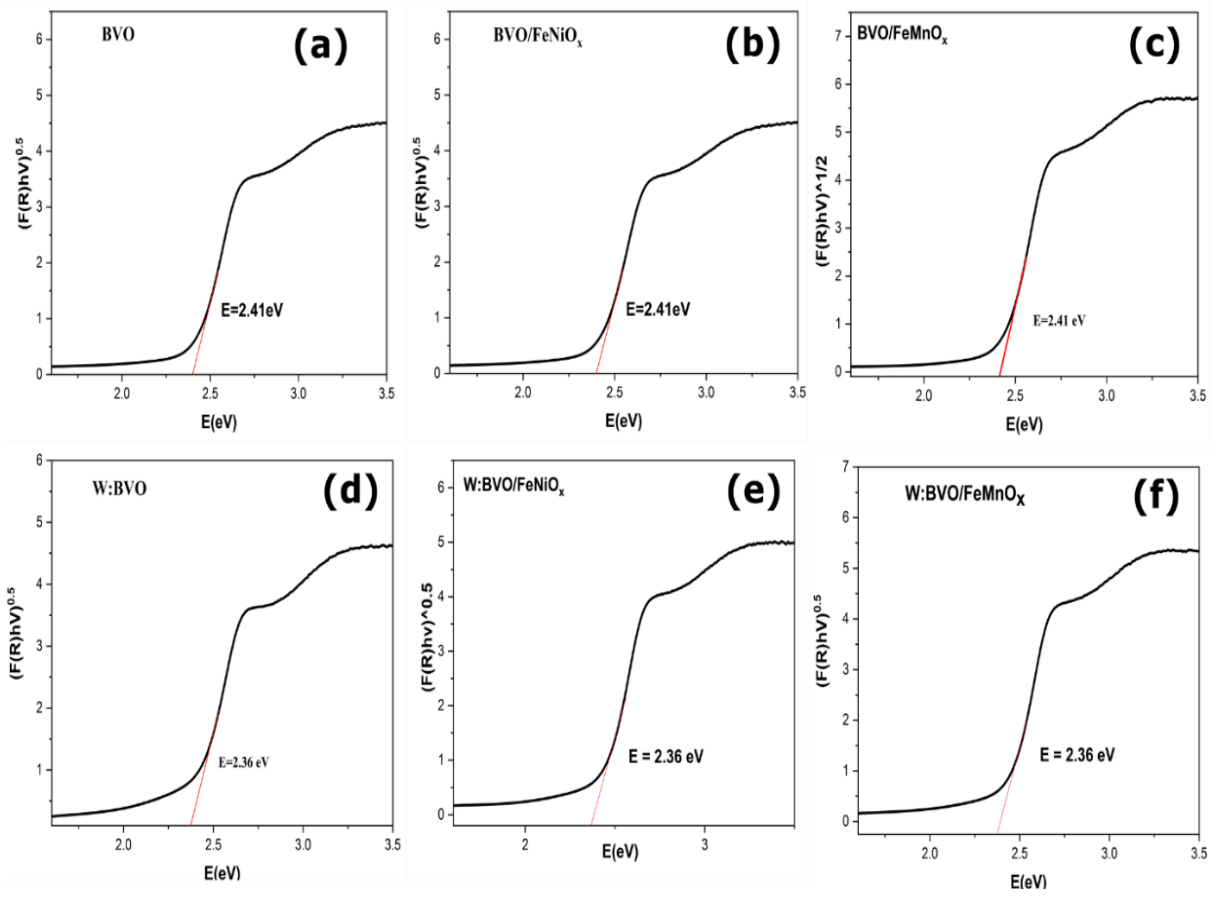

Figure 3.13A. Plots of transformed Kubelka–Munk function versus photon energy for BVO coated with $FeMnO_x$, and $FeNiO_x$ (a-c), and W:BVO coated with $FeMnO_x$, and $FeNiO_x$ cocatalysts (d-e).

3.5 X-ray photoelectron spectroscopy (XPS) of pure and W-doped $BiVO_4$

Surface chemical composition and binding energy (B.E) shifts were analyzed using X-ray photoelectron spectroscopy (XPS). XPS survey spectra of 1%, 2%, 3% W doped $BiVO_4$ and 2%W

doped $BiVO_4$ loaded with $FeMnO_x$ and $FeNiO_x$ cocatalysts are compared in Figure 3.14 and their high-resolution spectra of Bi4f, V2p, O1s, and tungsten (W) are compared in Figure 3.15.

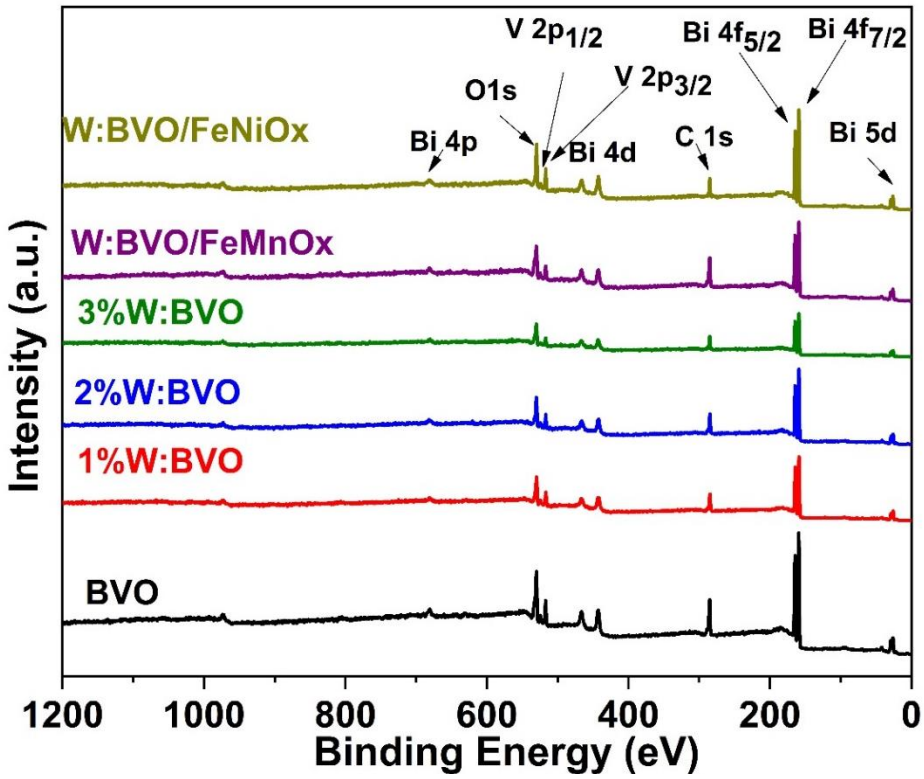

Figure 3. 14. XPS survey spectra of 1%, 2 %, and 3% W doped $BiVO_4$ and 2% W doped $BiVO_4$ loaded with $FeMnO_x$ and $FeNiO_x$ cocatalysts.

For pure BVO, two symmetric peaks named Bi 4f 7/2 and Bi 4f 5/2 appeared at B.Es of 164.5 and 159.2 eV corresponding to the Bi^{3+} oxidation state, respectively [126]. The two split peaks of V appeared at binding energies of 524.5 and 516.9 eV corresponding to V 2p1/2 and V 2p3/2, respectively, which were attributed to the V^{5+} oxidation state. B.Es for the Bi 4f and V 2p split peaks correspond to the formation of bismuth vanadate ($BiVO_4$) [127]. The XPS spectra of O1s were further fitted to three distinct peaks named O_c, O_v, and O_L. The O1s peaks appeared at binding energies of 529.8, 531.7, and 533.1 eV and were assigned to oxygen in the $BiVO_4$ lattice, oxygen defects in the semiconductor, and the C-O group [84]. The oxygen vacancies (O_V) are responsible for the electronic structure of $BiVO_4$, as found by many studies O_V-induced charge transition levels further help to reduce recombination sites and increase the conductivity of $BiVO_4$ [128]. It can be created when dopant atoms occupy the V site in the $BiVO_4$ structure, further extending the V-O bond on the $BiVO_4$ surface, thereby displacing the original coordinated O atom

to the doping site [129]. Therefore, the doping process is favorable for their formation, W dopant in the $BiVO_4$ promotes the $O_{V,}$ which eventually enhances the electron density near the bottom of the conduction band [92]. Increased concentration of W in $BiVO_4$ leads to increased oxygen vacancies due to greater migration of the original coordinated O atom to the doping site than in pure $BiVO_4$ (Figure 3.15c). Tungsten (W) peaks were also observed in the XPS spectra of the W-doped specimens; for the tungsten (W) doped $BiVO_4$ the two partially split peaks i.e. W $4f_{7/2}$ and W $4f_{5/2}$ correspond to B.Es of 35.4 and 37.5 eV confirming W^{+6} (Figure 3.15d). The W peak intensity was increased due to an increase in W concentration in $BiVO_{4,}$ which represents the percentage of W dopant in $BiVO_4$. Moreover, the B.Es of Bi 4f, V2p, and O1s shifted to higher values concerning W dopant in $BiVO_4$ as compared to the pure BVO. The shift in the B.Es can be elucidated by the closer interaction of the dopant hexavalent element (W) with Bi 4f, V2p, and O1s, which can be expected due to the interaction of high electronegativity of the dopant (W^{6+} > V^{5+}) [123]. As the $W^{6+} > V^{5+}$, replacing the V^{5+} site with W^{6+} dopants can gather more electrons around W, thus binding energies shifted [130]. Furthermore, W incorporation to the V site in $BiVO_4$ act as n type dopant which could rise the Fermi level towards the conduction band. Under light illumination W incorporation increase the carrier charge densities as well as separation of photogenerated electron-hole pairs due to band bending at the semiconductor/electrolyte interface [131].

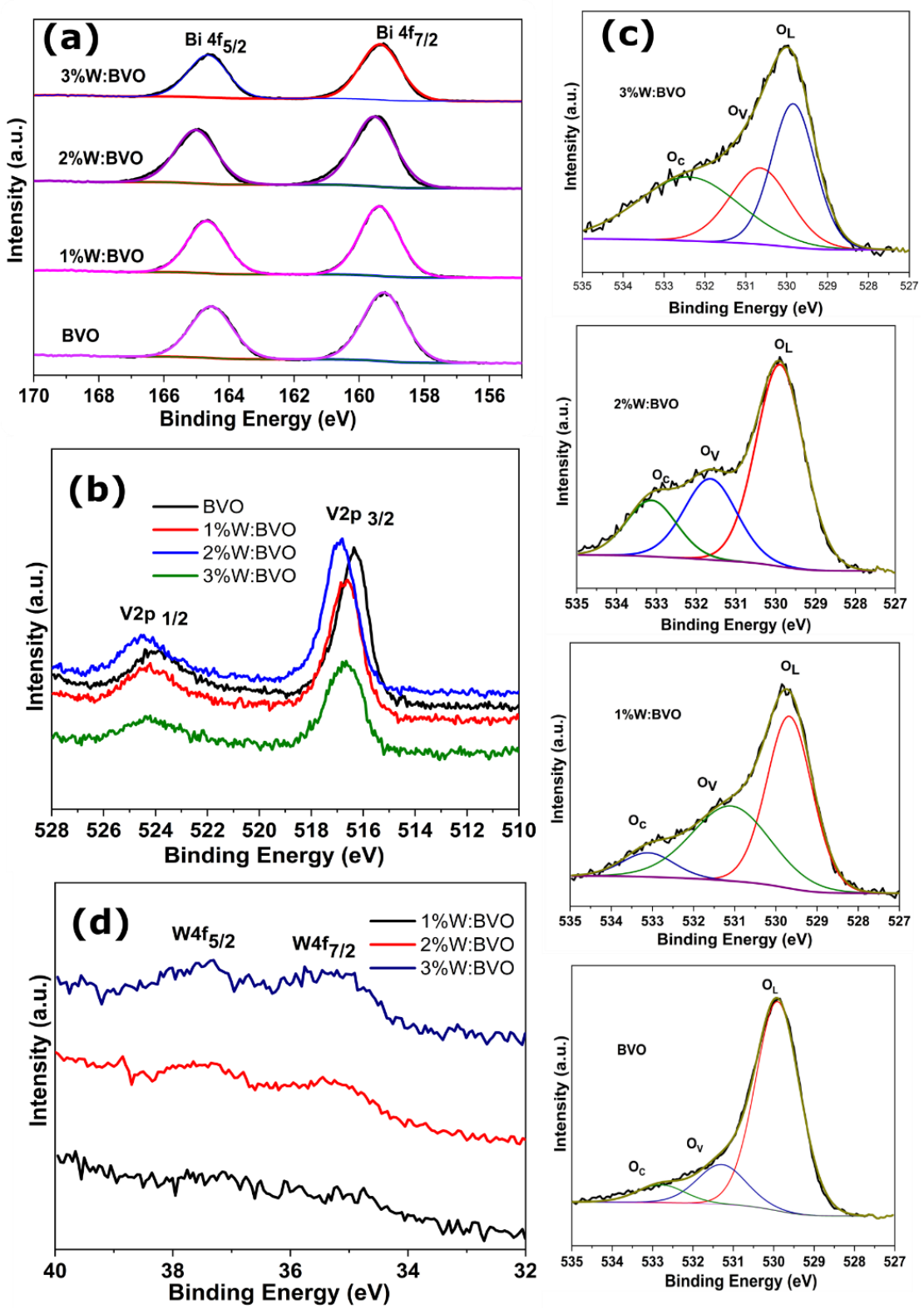

Figure 3. 15. XPS spectra of tungsten 1%W,2%W, and 3%W doped BVO samples compared to pure BVO, representing a shift towards higher binding energies (a) Bi4f (b) V2p, (c) O1s, and (d) tungsten (W) peaks intensity increased with concentration.

3.5.1 X-ray photoelectron spectroscopy of 2 %W-doped $BiVO_4$ loaded with $FeMnO_x$ and $FeNiO_x$ cocatalysts.

The surface chemical compositions and shift in binding energies were also analyzed from the XPS spectra for the samples loaded with $FeMnO_x$ and $FeNiO_x$ cocatalysts (Figure 3.16). The deposition of $FeMnO_x$ and $FeNiO_x$ cocatalysts on W:BVO shifts binding energies of Bi, V, and O. The Bi split peaks i.e. Bi $4f_{3/2}$ and Bi $4f_{1/2}$ in the W:BVO sample corresponds to the binding energies of 159.78 and 165.16 eV respectively. These B.Es were shifted to 159.67 and 164.98 eV for W:BVO/$FeMnO_x$ and 159.38 and 164.69 eV for W:BVO/$FeNiO_x$ (3.16a). Similarly, the V2p and O1s peaks for the samples loaded with cocatalysts shifted also to the lower binding energies (Figure 3.16b & 3.16c). $FeMnO_x$ and $FeNiO_x$ cocatalysts act as p-type semiconductors and $BiVO_4$ as n-type semiconductors. The Fermi level of the *n*-type semiconductor is near the conduction band while the Fermi level of the *p*-type is near the valence band. Both types of semiconductors are combined to form a p-n junction, thus causing band bending [132]. The shift in binding energies towards lower values is probably due to the upward band bending effect as $FeMnO_x$ and $FeNiO_x$ cocatalysts have different Fermi levels than $BiVO_4$; thus, combing materials with different Fermi levels causes band bending and induces an electric field [105]. Band bending provides beneficial energetics for the migration and separation of photogenerated charge carriers [133,134]. The $FeMnO_x$ and $FeNiO_x$ were deposited on W:BVO but there were no Fe, Mn, and Ni peaks detected in the XPS spectra, probably due to the lower content of cocatalysts at the surface of the $BiVO_4$ particles. The $BiVO_4$ particles were continuously moving by the use of agitating resonant mechanical apparatus; therefore, the deposited cocatalysts were homogeneously dispersed on $BiVO_4$, providing a very small amount of content for the XPS detection [125].

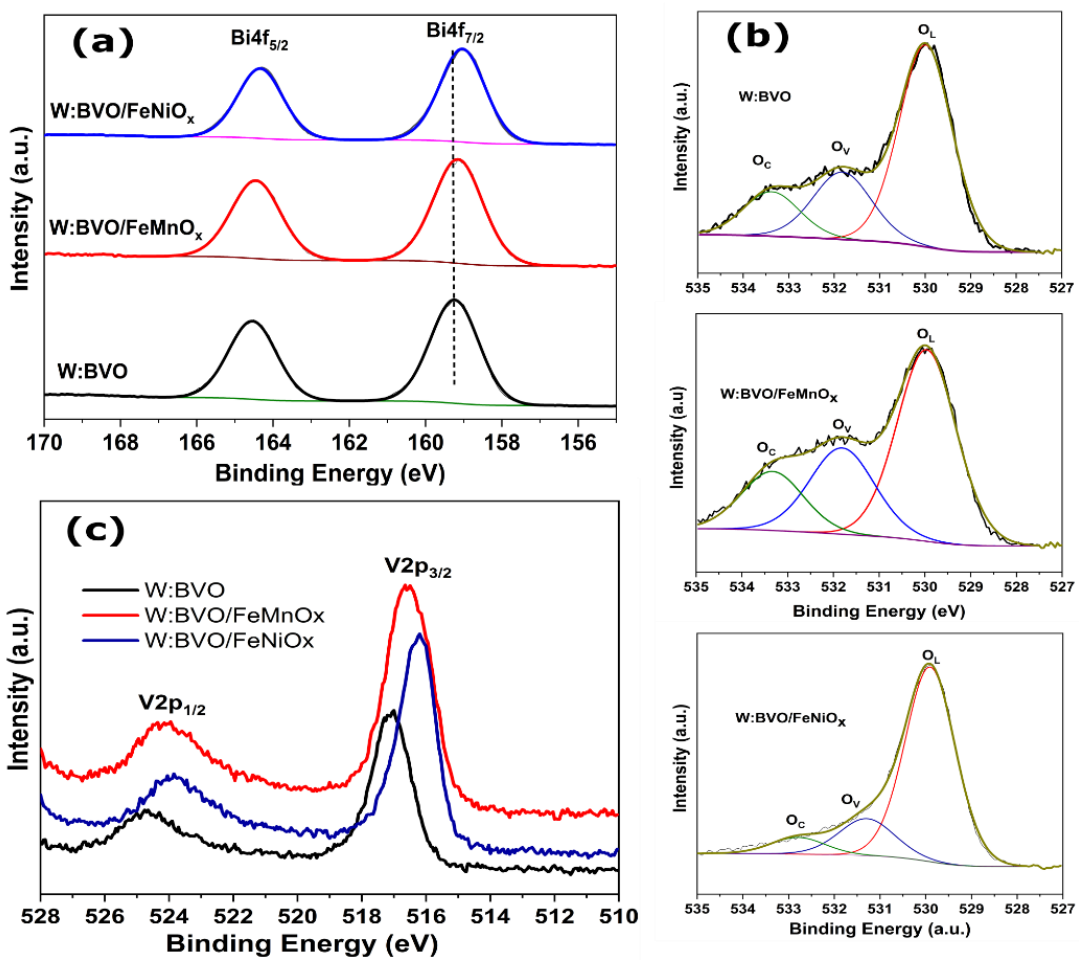

Figure 3. 16. XPS spectra of W:BVO loaded with $FeMnO_x$ and $FeNiO_x$ cocatalysts, representing a shift in B.E towards lower values for (a) Bi4f, (b) O1s, and (c) V2p.

Furthermore, to clarify the Fe, Mn, and Ni peaks, an extra deposition of $FeMnO_x$ and $FeNiO_x$ cocatalysts was made on the Si substrate using the same deposition time, keeping the substrate at a fixed position to ensure the deposition of the contents at the same place (Figure 3.17). The spin-orbit doublets of Fe2p in all samples located around 711.2 eV and 724.9 eV, which corresponds to the spin-orbital splitting of $2p_{3/2}$ and $2p_{1/2}$ of Fe^{3+} ions in the $FeNiO_x$ and $FeMnO_x$ structures [135,136]. The Ni 2p characteristic split peaks at 855.9 and 873.2 eV, corresponding to the Ni^{3+} oxidation state. Additionally, the presence of two more peaks around 854.5 and 872.2 eV may also indicate the presence of Ni^{2+} in the $FeNiO_x$ structure, and the peak around 855.9 and 873.7 eV indicates the presence of Ni^{3+}. The Mn 2p peaks located at 653.4 and 641.9 eV can be attributed

to the Mn^{3+} species in the $FeMnO_x$ sample, and also the peaks located around 654.4 and 643.2 eV correspond to the binding energy of Mn^{4+} [137].

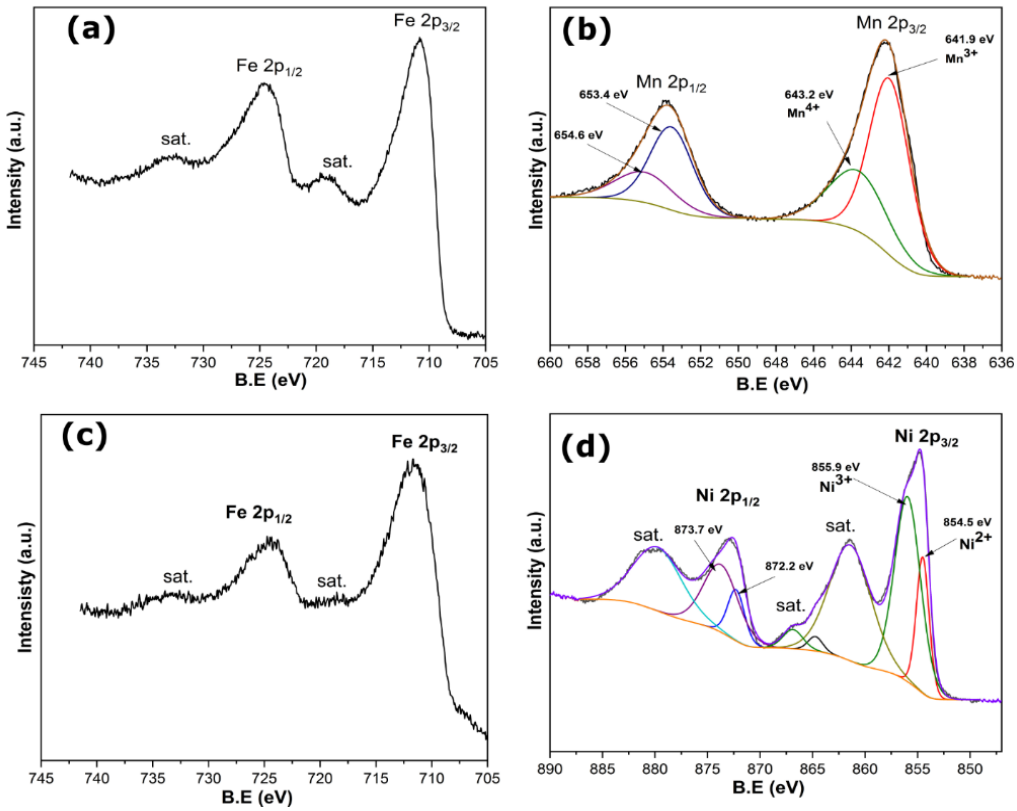

Figure 3. 17. XPS plots represent different Fe, Mn, and Ni peaks for the deposition of $FeMnO_x$ and $FeNiO_x$ cocatalysts on Si substrate.

3.6 High resolution transmission electron microscopy (HRTEM) of the W-doped BiVO4 loaded with FeMnOx

Figure 3.18 summarizes the high-resolution transmission electron microscopy (HRTEM) images combined with spectroscopy Energy Electron Loss Spectroscopy (EELS) and Energy Dispersive Spectroscopy (EDS) analyses that confirm the presence of FeMnOx nanoparticles over the W:BVO surface. HRTEM and the correspondent FFT image of the edge of W:BVO nanoparticle exhibited in Figure 3.18a, shows the high crystallinity of the sample. The crystallinity can be explained from the brighter spots in the FFT image which are related to the fringe strips. The brighter spots or fringe strips show periodicity (equally spaced) which can be related to the crystallinity [87]. Additionally, the contrast variation (dark region) at the edge of the HRTEM

image can be associated with the presence of FeMnOx, two of them are shown by yellow arrows with a size close to 5 nm. Figure 3.18b shows a HAADF (high angle annular dark field) image of the edges of three W:BVO nanoparticles, the areas used for drift correction (yellow box), and spectral image acquisition (green box). The Bi and W elements maps correspond to EDS measurement and V, O, Mn, and Fe element maps correspond to the average between EELS and EDS measurements. The EDS (Figure 3.18c) shows a uniform distribution of the Bi, V, O, and W, and despite the high damage caused by the electron beam, the presence of two FeMnOx nanoparticles on the surface of W:BVO with the sizes close to 5 nm again (see the coincidence position of Fe and Mn in the corresponding maps). Finally, the W intensity changes following the thickness of the sample, corroborating the uniform distribution observed by SEM results.

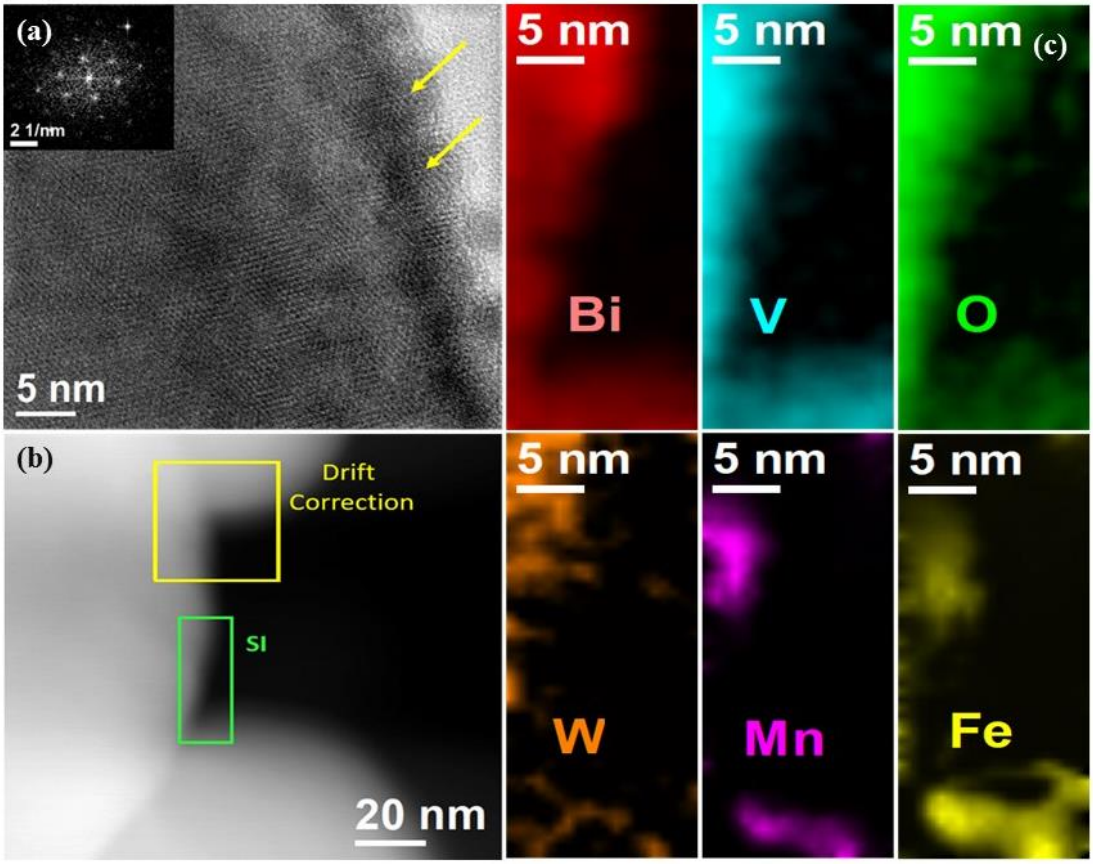

Figure 3. 18. (a) HRTEM image of the edge of W:BVO nanoparticle with the corresponding FFT inset, (b) HAADF (high angle annular dark field) image of the edges of three W:BVO nanoparticles and correspondent, and (c) EDS map, representing Bi, V, O, W, Fe, Mn, where Fe and Mn have a particle size of 5 nm.

3.7 Atomic Absorption Spectrometry (FAAS) and Graphite Furnace Atomic Absorption Spectrometry (GFAAS)

The contents of loaded cocatalysts were further identified by flame atomic absorption spectrometry (FAAS) and graphite furnace atomic absorption spectrometry (GFAAS) [138]. The FAAS and GFAAS were used to analyze Fe, Ni, and Mn contents in the W:BVO/$FeNiO_x$ and W:BVO/$FeMnO_x$ samples, where Ni content was detected by the FAAS and Fe and Mn contents detected by the GFAAS. The numerical values of the Fe, Ni, and Mn with standard deviation (SD) are given in Table 3.3. The different numerical values of these materials are due to the sensitivity of the system used to detect them.

Table 3.3. Representing the amount of Fe, Ni, and Mn contents detected by FAAS and GFAAS.

Fe		**Ni**		**Mn**	
µg/g	**SD**	**mg/g**	**SD**	**µg/g**	**SD**
36.14	2.53	0.75	0.0002	1.59	0.064

3.8 Photocatalytic oxygen evolution

The photocatalytic activity of $BiVO_4$ powders was tested for oxygen evolution in the presence of $Fe(NO_3)_3.9H_2O$ (50 mM) as a sacrificial agent. The O_2 evolution for all W-doped $BiVO_4$ samples is shown in Figure 3.19a, where the oxygen evolution of the as-prepared sample (BVO) is 93 µmol over 3 h illumination to the light source. The oxygen evolution was increased to 129 µmol for the 1% W-doped $BiVO_4$ (1%W:BVO), 160 µmol for 2% W-doped $BiVO_4$ (2%W:BVO), and 109 µmol for 3% W-doped $BiVO_4$ (3%W:BVO), which was attributed to the high exposure of the (040) facet and high charge transport efficiency in the bulk of the tungsten-doped $BiVO_4$. The growth of the (040) facet can be confirmed from the ratio (040/110) facets, which increased

for the 1%W, 2%W, and 3%W doped $BiVO_4$ sample as compared to the as-prepared BVO (Figure 3.1) [115]. Furthermore, $BiVO_4$ has two doping sites i.e. the Bi^{+3} site and V^{+5} site, doping of a hexavalent impurity (W^{+6}) to the V site donates more electrons thus increasing n-type conductivity which improves photo response [139]. W dopant in the $BiVO_4$ promotes the O_V, and these vacancies enhanced the electron density near the bottom of the conduction band [92]. The oxygen vacancies (O_V) are responsible for the electronic structure of $BiVO_4$, as found by many studies that O_V induced charge transition levels further help to reduce recombination sites and increase the conductivity of $BiVO_4$, thus improving photocatalytic activity [128]. Density-functional theory calculations (DFT) have also predicted that the W dopant is a shallow electron donor which increases the carrier charge density of the $BiVO_4$ [123,140].

P-type bimetallic $FeMnO_x$ and $FeNiO_x$ cocatalysts were also deposited on n-type pure $BiVO_4$ [17]. The photocatalytic activity of the BVO loaded with $FeNiO_x$ and $FeMnO_x$ cocatalysts was increased to 127 and 143 μmol (Figure 3.19b-c) for the best sample (deposition of 10 min) as compared to pure BVO (93 μmol). Similarly, the $FeNiO_x$ and $FeMnO_x$ cocatalysts were deposited on W-doped BVO as surface cocatalysts to further increase the photocatalytic activity. The photocatalytic oxygen evolution was further increased to 175 and 181 μmol after depositing $FeNiO_x$ and $FeMnO_x$ (Figure 3.19d). The increment in photocatalytic O_2 evolution is because of the deposition of *p*-type $FeMnO_x$ and $FeNiO_x$ bimetallic cocatalysts. The combination of *p*-type $FeMnO_x$ and $FeNiO_x$ cocatalysts with *n*-type $BiVO_4$ may create an extra built-in electric field to increase charge transfer and decrease charge recombination to further improve photocatalytic activity. The combination of *p*-type $FeMnO_x$ and $FeNiO_x$ cocatalysts with *n*-type $BiVO_4$ makes type II heterojunction (p-n junction) which provides potential barriers to inhibit the electron flow from the $BiVO_4$ to $FeNiO_x$ and $FeMnO_x$ layers [17]. Furthermore, p-type cocatalysts (oxidation cocatalysts) can facilitate the transfer and separation of photogenerated electron-hole, which further enhances photocatalytic activity [125,141]. The photocatalytic oxygen evolution for different samples, irradiated with visible light for 3 hours is shown in Table 3.4.

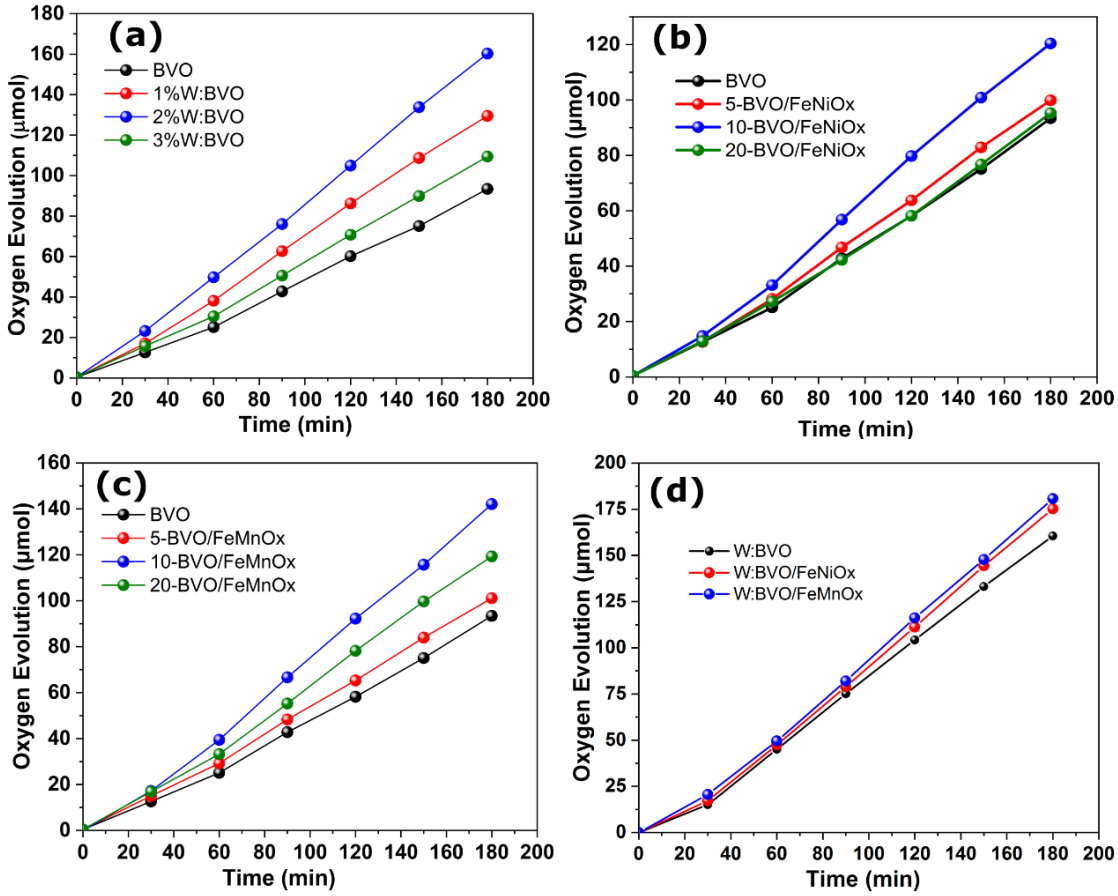

Figure 3. 19. Photocatalytic O_2 evolution test of (a) Pure and W (1%, 2%, and 3%) doped $BiVO_4$ (b) $FeNiO_x$ cocatalysts loaded on pure BVO, (c) $FeMnO_x$ cocatalysts loaded on pure BVO, (d) $FeMnO_x$, and $FeNiO_x$ cocatalysts loaded on tungsten doped BVO (W:BVO), over 3 h exposure to 300 W Xe lamp with an AM 1.5 G filter.

Photocatalyst stability and reusability are also important factors for the commercial use of photocatalysts. A recycling test was performed to further investigate the reusability of the photocatalysts, by illuminating the W:BVO/FeMnOx powder sample through a Xe lamp with an AM 1.5 G filter for four different cycles (each cycle of 3 h) (Figure 3.20). The reusability of a photocatalyst was tested for oxygen evolution using the previous setup. Photocatalytic O_2 evolution was measured every 30 min. The W:BVO/$FeMnO_x$ photocatalyst remained stable after four cycles, and only the oxygen activity decreased slightly. The slight decrease in the photocatalytic oxygenation of the photocatalyst is due to the losing of sample during recycling process. The results suggested that W:BVO/FeMnOx not only presents good stability but also has continuous photocatalytic activity. Therefore, W:BVO/FeMnOx can be used as a stable photocatalyst for the production of O_2.

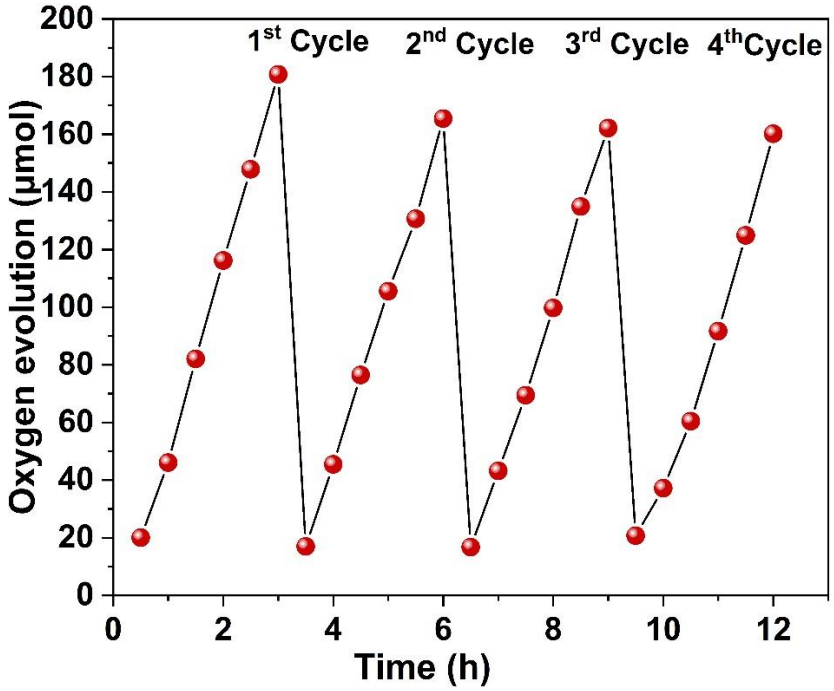

Figure 3. 20. Recycling test of the W:BVO/$FeMnO_x$ over four cycles (each cycle 3 h) exposure to 300 W Xe lamp with an AM 1.5 G filter for four cycles.

Table 3.4. Photocatalytic oxygen evolution, irradiated with 300 W Xe lamp with an AM 1.5 G filter for 3 hours.

S.NO	Sample Description	Sample ID	Oxygen Evolution (µmol)
1	$BiVO_4$	BVO	1240 µmol $g^{-1}h^{-1}$
2	1% W doped $BiVO_4$	1%W:BVO	1720 µmol $g^{-1}h^{-1}$
3	2% W doped $BiVO_4$	2%W:BVO	2133 µmol $g^{-1}h^{-1}$
4	3% W doped $BiVO_4$	3%W:BVO	1453 µmol $g^{-1}h^{-1}$
5	$BiVO_4$ loaded with $FeNiO_x$ for 5 min	5-BVO/ $FeNiO_x$	1333 µmol $g^{-1}h^{-1}$
6	$BiVO_4$ loaded with $FeNiO_x$ for 10 min	10-BVO/ $FeNiO_x$	1693 µmol $g^{-1}h^{-1}$
7	$BiVO_4$ loaded with $FeNiO_x$ for 20 min	20-BVO/ $FeNiO_x$	1267 µmol $g^{-1}h^{-1}$
8	$BiVO_4$ loaded with $FeMnO_x$ for 5 min	5-BVO/ $FeMnO_x$	1347 µmol $g^{-1}h^{-1}$

9	$BiVO_4$ loaded with $FeMnO_x$ for 10 min	10-BVO/ $FeMnO_x$	1907 μmol $g^{-1}h^{-1}$
10	$BiVO_4$ loaded with $FeMnO_x$ for 20 min	20-BVO/ $FeMnO_x$	1587 μmol $g^{-1}h^{-1}$
11	2% W doped $BiVO_4$ loaded with $FeNiO_x$ for 10 min	W:BVO/ $FeNiO_x$	2233 μmol $g^{-1}h^{-1}$
12	2% W doped $BiVO_4$ loaded with $FeMnO_x$ for 10 min	W:BVO/ $FeMnO_x$	2413 μmol $g^{-1}h^{-1}$

3.9 Band alignment and charge transport properties.

To investigate the interfacial band alignment and photoinduced charge pathways on the W:BVO/$FeNiO_x$ and W:BVO/$FeMnO_x$ heterojunctions, we first constructed their energy band diagrams under equilibrium (i.e., dark) conditions. To this end, the Fermi level position, impurity concentrations, and bandgaps of the isolated (pure) semiconductors (in the form of films) were estimated using Mott-Schottky (MS) analysis and UV-Vis spectroscopy. Specifically, pure $FeNiO_x$ and $FeMnO_x$ films were deposited by magnetron sputtering, whereas spin-coating was employed to produce the pure W:BVO film. All MS curves were measured in 0.1 M potassium phosphate electrolyte (pH 7), typical for BVO-based photoanodes [105,132]. Figure 3.21a shows the MS curve for the pure W:BVO film, clearly showing a straight line with a positive slope, characteristic of n-type semiconductors. According to equation 3.3, the donor concentration (N_D) and flat band potential (E_{FB}) for the pure W:BVO, calculated from the angular coefficient and intercept of the straight line, are $N_d = 1.30 \times 10^{18}\ cm^{-3}$ and $E_{FB} = 0.12$ V vs. RHE, respectively. Importantly, these estimated values are similar to that reported in the literature. [140,142]. In contrast, Figure 3.21b shows the MS curve for the pure $FeNiO_x$ film, exhibiting a straight line with a negative slope, which is a p-type semiconductor signature. From equation 3.4, the concentration of acceptors and flat potential for $FeNiO_x$ is $1.22 \times 10^{19}\ cm^{-3}$ and $1.22\ V$ vs. RHE, respectively. A similar analysis for pure $FeMnO_x$ film reveals that $N_A = 5.15 \times 10^{19}\ cm^{-3}$ and $E_{FB} = 1.29$ V vs. RHE (Figure 3.21c). Furthermore, the bandgap energies estimated with Tauc plots for the $FeNiO_x$ and $FeMnO_x$ films are 2.32 and 2.15 eV, respectively (Figure 3.22).

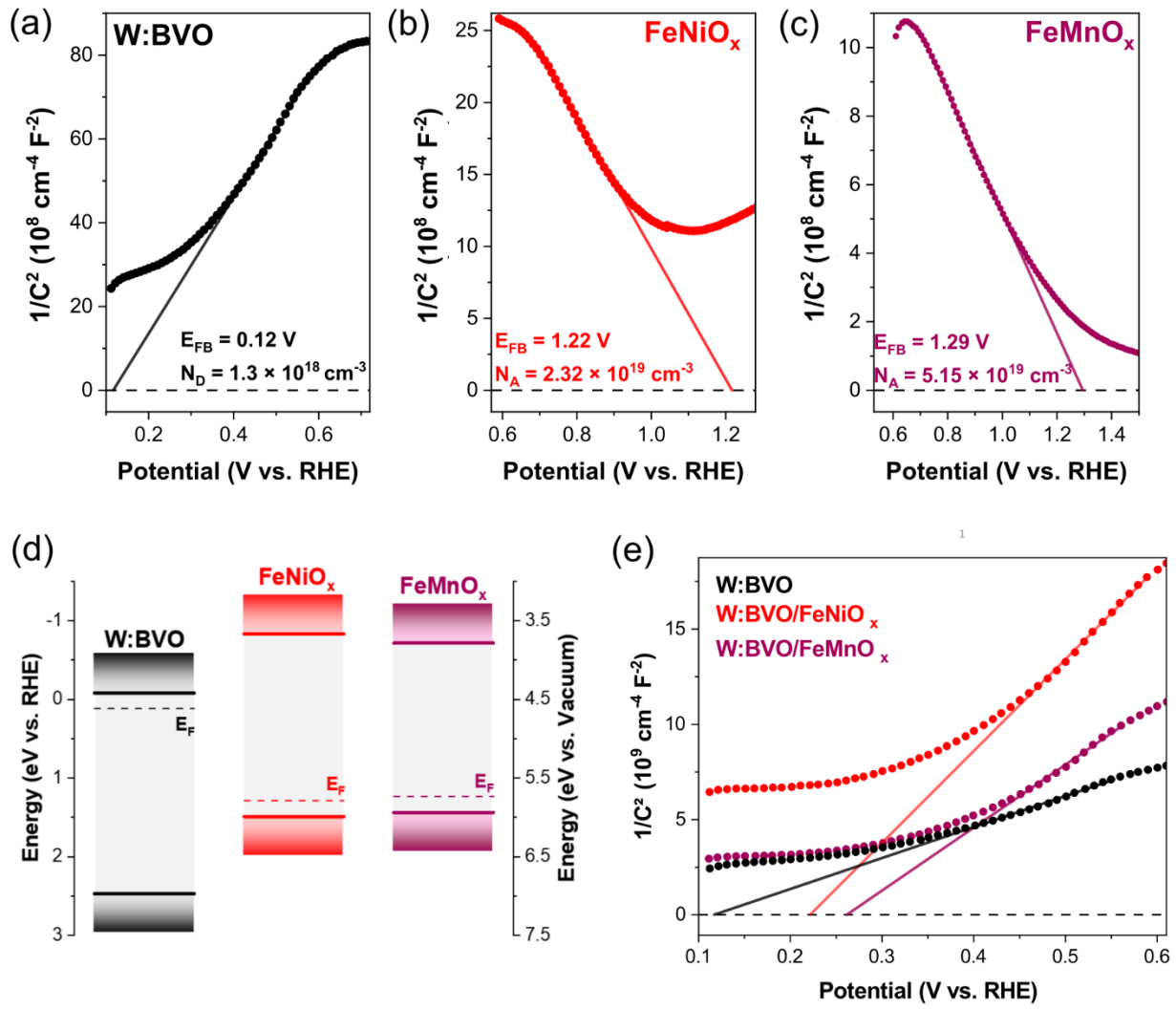

Figure 3. 21 Mott-Schottky curves for (a) n-type W:BVO film, (b) p-type $FeNiO_x$ film, and (c) p-type $FeMnO_x$ film; (d) energy band diagrams for pure W:BVO, $FeNiO_x$, and $FeMnO_x$ semiconductors; and (e) Mott-Schottky curves for the W:BVO/$FeNiO_x$ and W:BVO/$FeMnO_x$

$$\frac{1}{C_{SC}^2} = \frac{2}{eA^2\epsilon_r\epsilon_0 N_D}\left(E - E_{FB} - \frac{kT}{e}\right), \qquad \text{n} - \text{type} \qquad (3.3)$$

$$\frac{1}{C_{SC}^2} = \frac{2}{eA^2\epsilon_r\epsilon_0 N_A}\left(-E + E_{FB} - \frac{kT}{e}\right), \qquad \text{p} - \text{type} \qquad (3.4)$$

Figure 3.21d shows the band diagrams of pure W:BVO, $FeNiO_x$, and $FeMnO_x$ semiconductors, constructed under the assumptions that (i) the Fermi energy is approximately equal to the flat potential for the isolated semiconductors immersed in aqueous solutions [143],

(ii) the V.B of the p-type semiconductor is $\sim 0.2\ V$ above the top of V.B, and (iii) the C.B of the n-type semiconductor is $\sim 0.2\ V$ below the top of C.B [144]. Therefore, based on the alignment of flat bands of individual semiconductors before contact, we can infer the formation of desirable type II heterojunctions at the W:BVO/$FeNiO_x$ and W:BVO/$FeMnO_x$ interfaces. However, in addition to this type II alignment, local *p*-*n* heterojunctions between the *n*-type W:BVO and *p*-type bimetallic oxides are expected to occur. To verify the possible development of *p*-*n* heterojunctions, we further measured the MS curves of the W:BVO/$FeNiO_x$ and W:BVO/$FeMnO_x$ films. According to Figure 3.21e, the flat band potential of the heterojunctions exhibits a positive shift compared to that of W:BVO. As discussed below, to achieve electronic equilibrium (net zero current flow) under dark conditions, the Fermi energy of the *n*-type layer tends to increase in energy (moving towards the E_F of the *p*-type semiconductor) when the *p*-*n* heterojunction forms. Therefore, these characteristic positive shifts of the flat band potential unambiguously indicate the electrochemical (Fermi energy) potential alignment between the W:BVO and the bimetallic oxides, evidencing the formation of a p-n heterojunction [105,145]. Note that this result corroborates with our XPS analyses, where the Bi 4f and V 2p core levels of W:BVO shifts to lower binding energies after contact with the $FeMO_x$ (M = Ni, Mn) layers (Figure 3.16), suggesting the upward band bending by transferring electrons from the W:BVO to the p-type layer, which is typical for a *p*-*n* type-II heterojunction.[146] Interestingly, the measured N_D values for the heterojunctions and pure W:BVO film are very similar ($\sim 10^{18}\ cm^{-3}$), indicating that the charge carrier density in the W:BVO film was not affected by the deposition of $FeNiO_x$ and $FeMnO_x$ bimetallic oxides due to their ultrathin thickness.

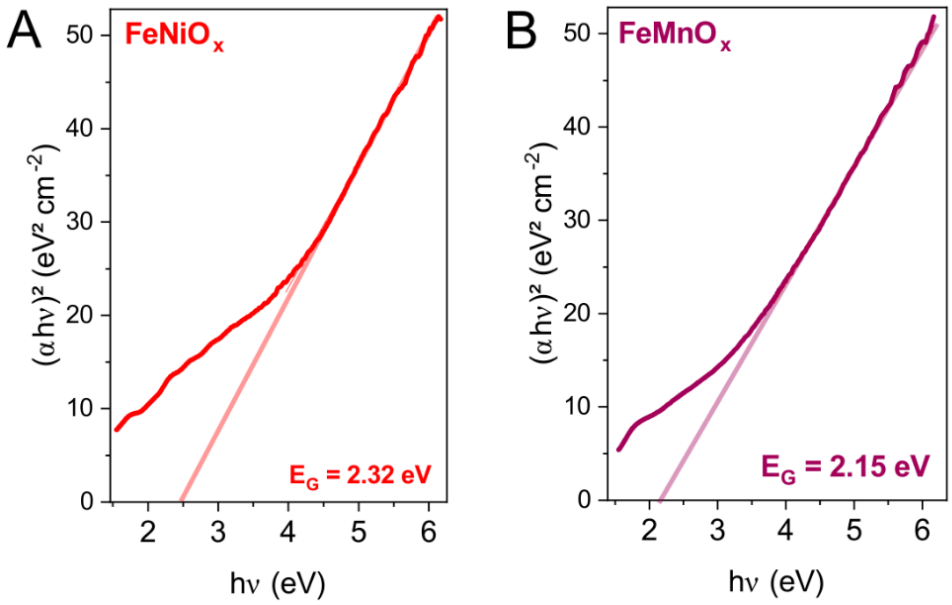

Figure 3. 22. (Direct) optical bandgap energy for pure (a) $FeNiO_x$ and (b) $FeMnO_x$ films.

Beyond the analysis of flat band diagrams, it is well known that *p*-*n* heterojunctions exhibit an interfacial space charge layer (SCR) characterized by the formation of band bending and built-in electric fields [107]. Precisely, under dark conditions, the Fermi energies (electrochemical potentials) of the *n*-type W:BVO and *p*-type $FeMO_x$ (M = Ni, Mn) semiconductors must align to ensure electronic equilibrium (net zero current flow) in the heterojunction. To this end, electrons in the W:BVO tend to diffuse into the *p*-type layer, while the holes in the *p*-type semiconductor follow the inverse pathway. These diffusions occur until the Fermi energy is constant throughout the entire heterojunction, producing an SCR characterized by band bending and a built-in electric field ($\vec{E}_{bi}$) that points from the *n*-type to the *p*-type semiconductor[107]. It is crucial to emphasize that band bending occurs due to the pinning of the semiconductor energy bands at the *p*-*n* interface, while the energy bands located in bulk move together with E_F. Furthermore, the SCR has energetic extension defined by the built-in potential ψ_{bi} (calculated by the difference between the Fermi energies, i.e., work functions, of the semiconductors), which is distributed over the energy drops in the n and p-type layers (Ψ_n and Ψ_p, where $q\psi_{bi} = |\Psi_n| + |\Psi_p|$), and spatial extension defined by the depletion widths in the n-type (W_n) and p-type (W_p) layers.

To understand the influence of these interfacial effects on the catalytic performance of the W:BVO/$FeNiO_x$ and W:BVO/$FeMnO_x$ heterojunctions, we constructed their interfacial band alignments using the classical band bending model under equilibrium (dark) conditions (see

appendix 1 for further details concerning theory, assumptions, and limitations of this model). As shown in Figure 3.23a, the W:BVO/$FeNiO_x$ heterojunction under dark shows (i) a constant Fermi energy throughout the entire material (indicating an equilibrium state); (ii) a space charge layer characterized by band bending with potential drops $\Psi_{\mathrm{n}}^{1} = 85$ meV and $\Psi_{\mathrm{p}}^{1} = 25$ meV, and depletion lengths of $\mathrm{W}_{\mathrm{n}}^{1} = 70$ nm and $\mathrm{W}_{\mathrm{p}}^{1} = 4$ nm; (iii) and a built-in electric field that points from the n-type to the p-type layer. A similar analysis for the W:BVO/FeMnO*x* heterojunction (Figure 3.23b) reveals potential drops $\Psi_{\mathrm{n}}^{2} = 107$ meV and $\Psi_{\mathrm{p}}^{2} = 10$ meV, and depletion lengths of $\mathrm{W}_{\mathrm{n}}^{2} = 79$ nm and $\mathrm{W}_{\mathrm{p}}^{2} = 2$ nm. The asymmetric band bending for both heterojunctions results from the significant difference between the impurity concentrations in the *n* and *p* layers ($N_D \ll N_A$), corroborating with previous publications [105,106]. Importantly, during the electrochemical alignment, the Fermi energy of the W:BVO layer tends to increase (in energy) significantly, while the Fermi energy of the *p*-type layer increases only marginally (due to the higher concentration of acceptors, $N_A \gg N_D$). Indeed, the calculated Fermi energies after equilibrium are 0.97 and 1.18 eV vs. RHE for the W:BVO/$FeNiO_x$ and W:BVO/$FeMnO_x$ heterojunctions, respectively, which are values close to the Fermi energy of the *p*-type layer.

According to the above analysis, the built-in electric field is the key element for photocatalytic applications, as it may efficiently accelerate the photogenerated charges of the W:BVO to the electrolyte, significantly suppressing their recombination. Precisely, applying electromagnetic radiation (photons with energy greater than E_G) to *p-n* heterojunctions has some consequences on their interfacial band alignment, including (i) the band flattening effect, acting as a slight forward bias that tends to reduce band bending due to the presence of photogenerated charges within the SCR [147], (ii) the preferential flow of photogenerated charges due to the presence of the built-in electric field, and (iii) the splitting of the dark Fermi level into quasi-Fermi levels to describe the non-equilibrium population of photogenerated electrons and holes. [148,149] According to these consequences, the photogenerated holes in the W:BVO layer are accelerated towards the *p*-type layer, which then carries out the water oxidation reactions at the sites of the $FeNiO_x$ and $FeMnO_x$ cocatalysts. In contrast, the photogenerated electrons in the W:BVO layer are efficiently accelerated by the built-in electric field towards the electrolyte, conducting the reduction of Fe^{3+} ions to Fe^{2+} at the W:BVO/electrolyte interface. It is essential to note that the potential barriers ΔE_V and ΔE_C (typical for type II heterojunctions) also assist in suppressing the recombination of electron-hole pairs by inhibiting the flow of photogenerated

electrons on the W:BVO to the bimetallic oxide layers and facilitating the transfer of photogenerated holes towards the $FeMO_x$ sites. Crucially, the built-in electric field intensity is associated with potential drops and depletion lengths: higher values of W_n^1 and Ψ_n^1, for instance, produce more intense built-in electric fields. In conclusion, the superior photocatalytic performance of the W:BVO/$FeMnO_x$ heterojunction, when compared to the W:BVO/$FeNiO_x$ heterojunction, can be attributed to the development of a relatively more intense built-in electric field, as indicated by the slightly higher values of depletion length and potential drops in n-type W:BVO layer.

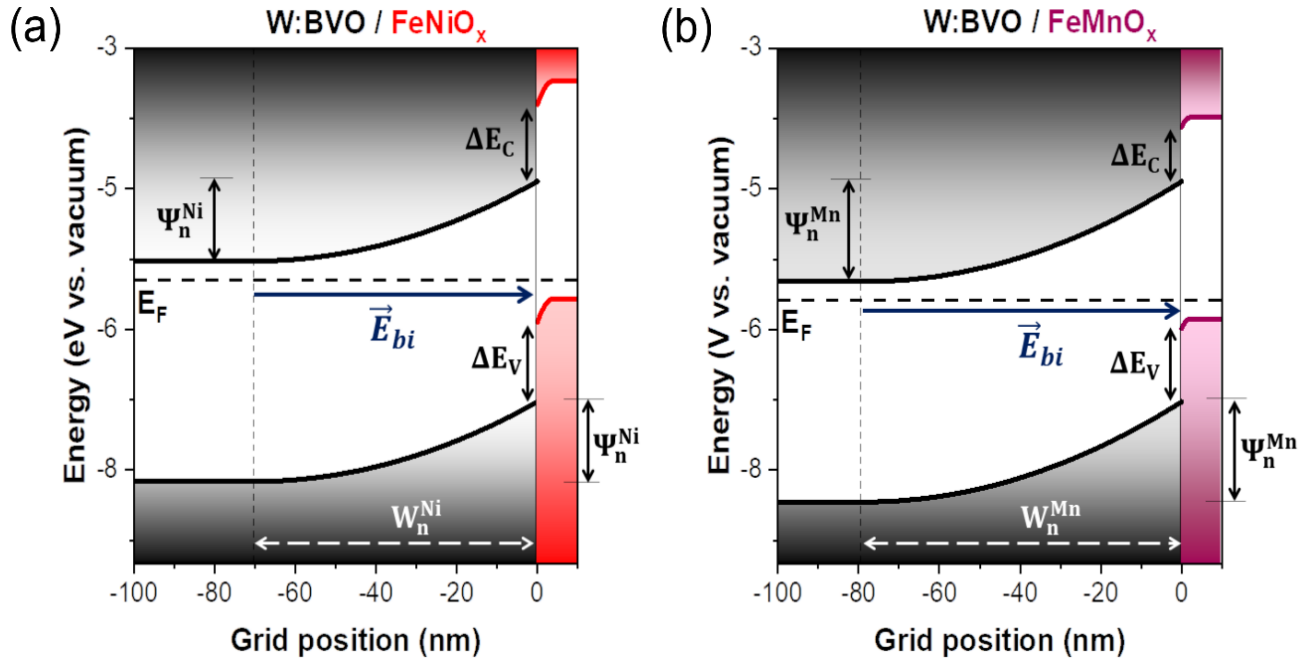

Figure 3. 23. Interfacial band alignment for the (a) W:BVO/$FeNiO_x$ and (b) W:BVO/$FeMnO_x$ heterojunctions.

4. Zinc (Zn) doped $BiVO_4$: Result and discussion

4.1 X-ray diffraction pattern of pure and Zn-doped $BiVO_4$

The structural properties of all doped and un-doped powder samples were studied using X-ray diffraction (XRD). All the XRD peaks for doped and un-doped samples are the characteristic peaks of the monoclinic scheelite (m-s) phase of $BiVO_4$ which are in agreement with standard Joint Committee on Powder Diffractions Standards (JCPDS) with Card No. 14-0688 [114]. It was also confirmed from the XRD data that adding (doping) of Zn to $BiVO_4$ does not lead to the formation of extra peaks; however, the intensities of peaks at position 2θ~18.7 °, 28.8 °, and 30.55 ° in all dopant samples was found affected due to increasing concentration of Zn. This specific position of intensities at 2θ~18.7 °, 28.8 °, and 30.55 ° represent different facets i.e. (110), (121), and (040) in which (121) corresponds to the characteristic peak of $BiVO_4$.

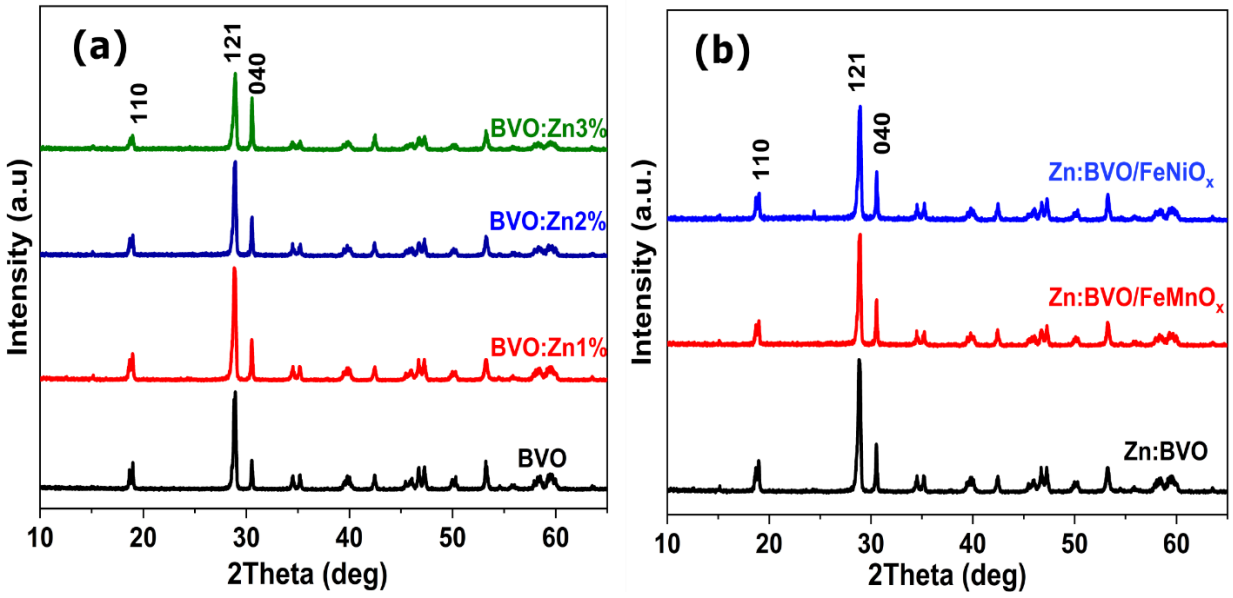

Figure 4. 1. XRD pattern of (a) pure BVO and Zn doped (1%, 2%, and 3%) BVO and (b) Zn doped BVO loaded with $FeMnO_x$ and $FeNiO_x$ cocatalysts.

It is clear from all XRD peaks of the dopant samples that the intensity at 2θ~18.7° decreased and the intensity at 2θ~ 30.55 ° increased with increasing concentration of Zn (Figure 4.1a). The increase in intensity at 2θ~30.55 ° is showing a crystal growth toward the (040) facet [123]. It was also confirmed that XRD peaks were shifted to lower 2θ at lower concentrations of Zn (1% and 2%) but at higher concentrations of (3%) shifted the XRD to a higher angle which is consistent

with the unit cell shrinkage according to Bragg's law [8,150,151]. Zn was also incorporated into Bi site using the same synthesis procedure, adding Zn precursors to Bi site instead of the V site. It was confirmed that anchoring Zn on the V side improves the crystallinity compared to anchoring on the Bi and results in crystal growth towards the (040) facet as shown in Fig 4.2. Therefore, Zn was incorporated into the V site instead of the Bi site for the synthesis of all Zn doped $BiVO_4$ samples. The crystallinity of Zn doping to the V side (~77%) is higher than the crystallinity of Zn doping to Bi side (~66%). The crystallinity is related to the crystallite size, for the Zn doped to V site the crystallite size was measured 29.2 nm and for Zn doping to Bi side reduced to 26.2 nm [152]. The crystallinity further improves the photocatalytic activity of semiconductors, as structural defects in semiconductors lead to increased charge recombination, which can be overcome by producing semiconductors with higher crystallinity [35,153].

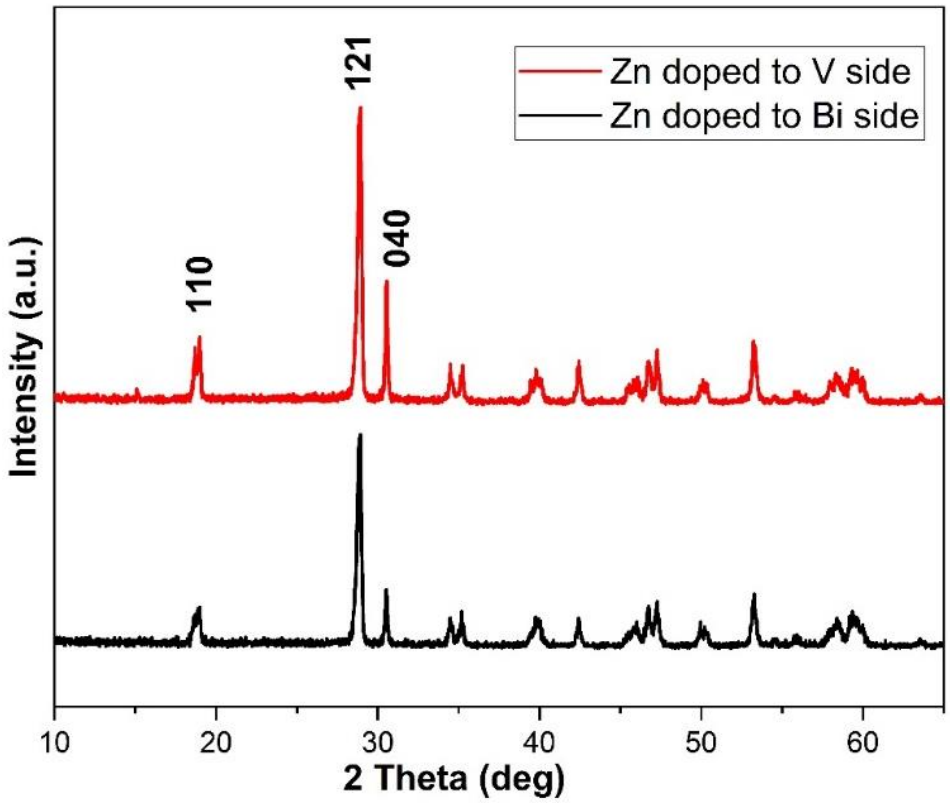

Figure 4. 2. XRD pattern of 2% Zn doping to V and Bi sites respectively; resulting in improved crystallinity.

Table 4.1. Crystalline (based on XRD analyses) and morphological (based on SEM images) properties of pure $BiVO_4$ and Zn-doped $BiVO_4$.

S.NO	Sample	Crystallite size (nm)	Crystallinity (100%)	Particle size length (nm)	Particle size width (nm)
1	BVO	27.0	65	620 ± 15	300 ± 10
2	BVO:Zn1%	28.2	70	417 ± 11	279 ± 12
3	BVO:Zn2%	29.2	77	370 ± 12	370 ± 13
4	BVO:Zn3%	24.8	69	535 ± 14	317 ± 11

4.1.1 X-ray diffraction pattern of Zn-doped $BiVO_4$ loaded with $FeMnO_x$ and $FeNiO_x$ cocatalysts

XRD was also performed to further study the structural properties of Zn-doped BVO loaded with $FeMnO_x$ and $FeNiO_x$ cocatalysts using the same parameters discussed above. It was found that the XRD pattern of Zn-doped BVO loaded with $FeMnO_x$ and $FeNiO_x$ was similar to Zn-doped BVO (Zn:BVO). The same XRD spectra of these samples are probably due to the lower contents of the cocatalysts at the surface of the 2%Zn-doped BVO. Furthermore, the lower contents of $FeMnO_x$ and $FeNiO_x$ on the surface of 2%Zn-doped BVO do not change the crystallographic planes; therefore, resulting in the same structure (Figure 4.1b).

4.2 Raman spectroscopy of pure, 1%, 2%, and 3%Zn doped $BiVO_4$, and 2%Zn doped $BiVO_4$ loaded with $FeMnO_x$ and $FeNiO_x$

Raman spectra were performed to further clarify the bonding state and the local structure of all zinc (Zn) doped $BiVO_4$ samples. The vibrational bands of as-prepared samples were observed at 327, 373, and 830 cm^{-1}, where the bands at 830, 327, and 373 cm^{-1} related to symmetric stretching mode, symmetric and asymmetric bending mode of V-O in VO_4^{-3} units [154]. The highly intense vibrational band at 830 cm^{-1} was assigned to the V-O bond length [151]. The major vibrational band in the pure $BiVO_4$ was observed at 830 cm^{-1}, which was changed to the lower wave numbers for the Zn-doped $BiVO_4$. The corresponding shift in the Raman spectra for the Zn

doped $BiVO_4$ samples is shown in Figure 4.3, where the major peaks shifted to lower wavenumbers concerning 1%, 2%, and 3% Zn dopants. The lowest shift of 827 cm^{-1} was observed for the sample doped with 2% and 3% of Zn.

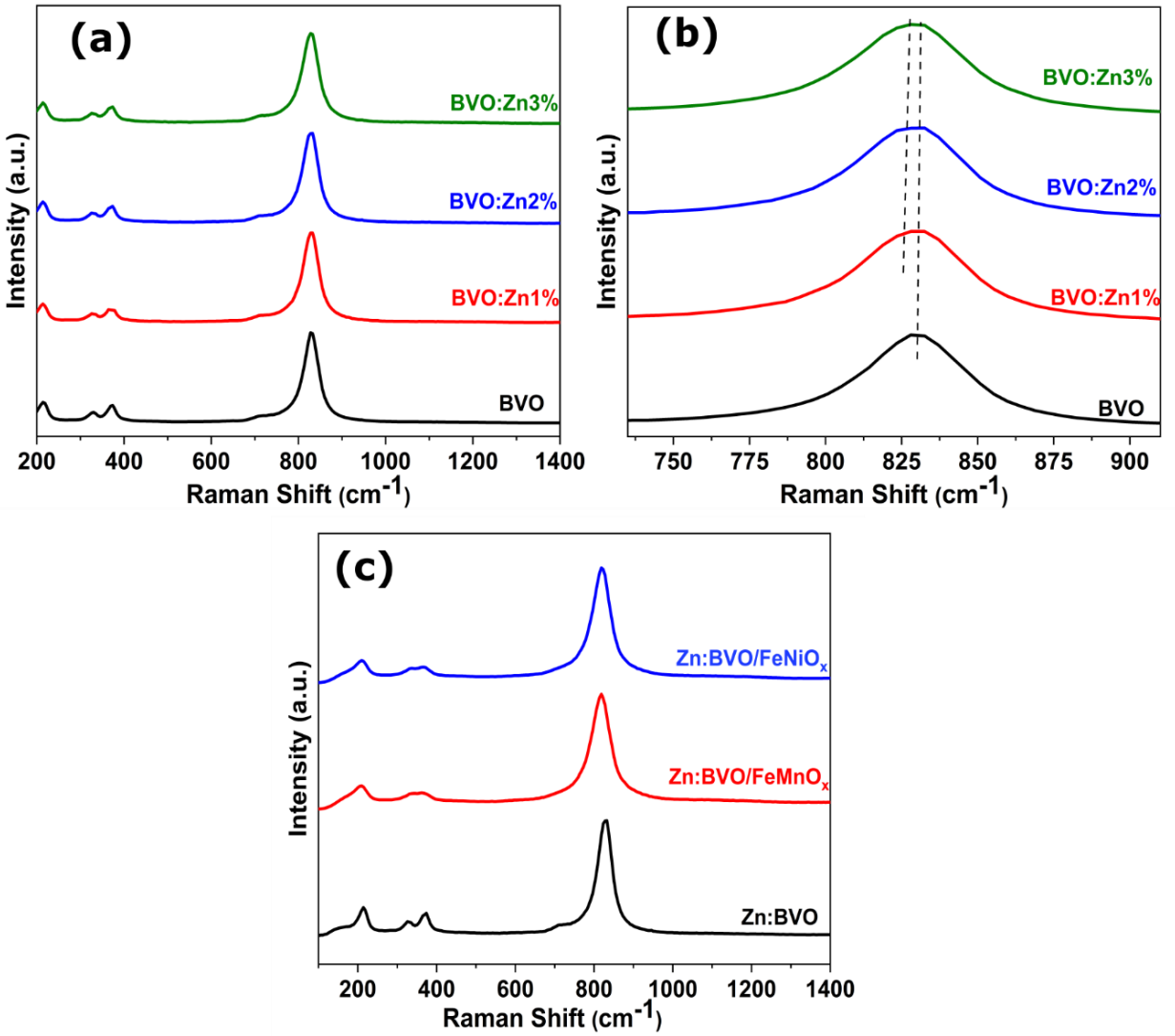

Figure 4. 3. (a) Raman spectra of pure and Zn (1%, 2%, & 3%) doped $BiVO_4$, (b) corresponding Raman shift, and (c) Raman spectra of Zn doped BVO with cocatalysts.

The shift in the Raman spectra was related to V-O bond length using equation 3.2 [155]. The Raman shifts and corresponding bond lengths are shown in Table 4.2, where the as-prepared and BVO:Zn2% have bond lengths of 1.6939 Å and 1.6958 Å respectively. The increase in the bond length is because of the different ionic radii of Zn than vanadium which can also be related to the

high crystallinity of Zn-doped BVO (Figure 4.1) compared to as prepared BVO [89,92]. The Raman spectra were also obtained for the Zn-doped BVO loaded with cocatalysts using the same conditions and found that the Raman spectra remain unaffected due to loading with $FeMnO_x$ and $FeNiO_x$ cocatalysts. The similar Raman spectra of the Zn:BVO/$FeMnO_x$ and Zn:BVO/$FeNiO_x$ samples are because of the lower contents of cocatalysts on Zn-doped $BiVO_4$.

$$\upsilon\ (cm^{-1}) = 21349 \exp(-1.9176\ R(Å)) \qquad (3.2)$$

Table 4.2. Raman shift, bond length, and bandgap based on Raman and UV-vis analysis.

S.No	Samples	Raman shift (cm^{-1})	Bond length (Å)	Bandgap (eV)
1	BVO	830	1.6939	2.42
2	BVO: Zn1%	828	1.6952	2.40
3	BVO: Zn2%	827	1.6958	2.37
4	BVO: Zn3%	828	1.6952	2.38

4.3 Ultraviolet-visible (UV-vis) spectroscopy

UV-vis spectroscopy was used to investigate the optical properties of all $BiVO_4$ powder samples. All the pure and Zinc (Zn) doped $BiVO_4$ samples reveal a strong absorption in the visible region. The band gap energies were calculated using the Tauc plot, it was observed that band energies red shifted due to an increase in the concentration of the Zn dopant in the $BiVO_4$. The band energy for the as-prepared samples corresponded to 2.42 eV, which was reduced to 2.37 eV upon doping with Zn. The band energy plots are shown in Figure 4.4, representing a redshift. The reason for the redshift in band gap energies is the formation of extra states by Zn dopants between valence and conduction bands of the $BiVO_4$ [97,156,157]. Some authors have also proposed that the narrowing of the band gap is due to the mixing of the B 1s and O 2p orbitals [158]. Zn dopants have larger radii of 0.083 nm than V (0.035 nm), introducing Zn to the $BiVO_4$ structure produces lattice deformation and induced oxygen vacancies which could be the reason for the impurity states

in the bandgap of $BiVO_4$. The availability of impurity states further improves the absorption and reduces the band gap [158,159]. Zn incorporation to the V site in $BiVO_4$ acts as *n*-type dopant which could rise the Fermi level of pristine $BiVO_4$ towards the conduction band. The redshift may be due to the charge transfer transition between the metallic ions and the valence/conduction band. Beside that dopants cause defects, leading to breaks in the periodicity; thus, decreasing the band gap energy [124]. There was no obvious change observed in the reflectance spectra of the samples loaded with bimetallic $FeMnO_x$ and $FeNiO_x$ cocatalysts, therefore corresponding to similar bang gap energies. The $FeMnO_x$ and $FeNiO_x$ cocatalysts have no obvious impact on the optical properties of the semiconductor which is probably due to the lower amount of cocatalysts on the surface of $BiVO_4$.

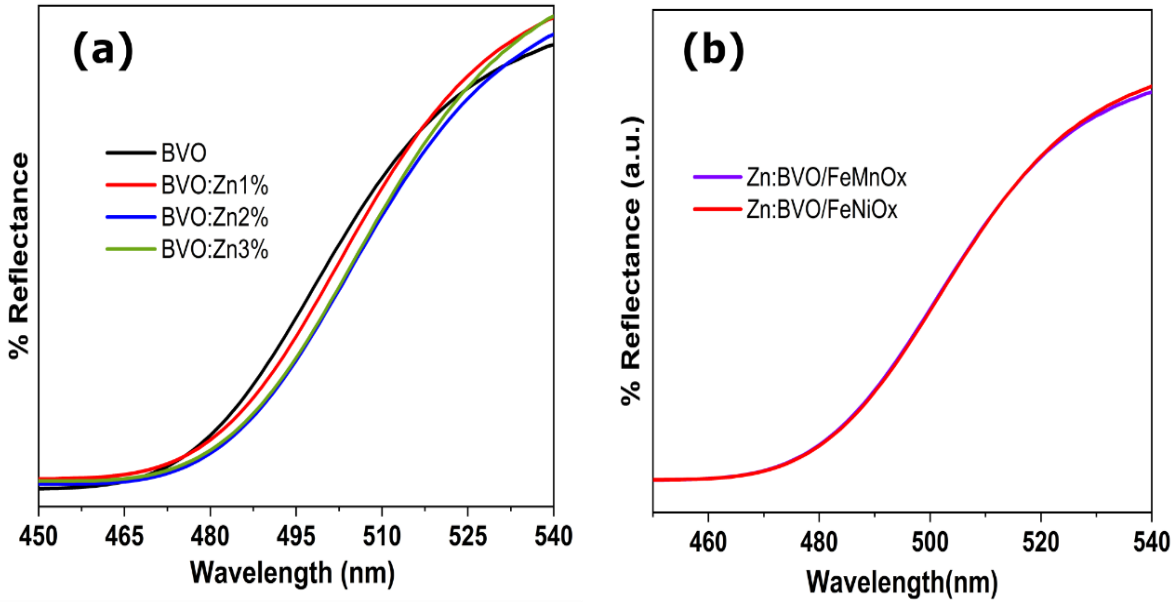

Figure 4. 4. UV-vis diffuse reflectance spectra of (a) Zn-doped $BiVO_4$, and (b) Zn-doped $BiVO_4$ loaded with $FeMnO_x$ and $FeNiO_x$ cocatalysts.

4.4 Brunauer, Emmett and Teller (BET) Analysis

The BET Surface area for the pure and Zn doped $BiVO_4$ sample is compared in Figure 4.5, where the Zn doped $BiVO_4$, exhibits a high surface area of 1.92 m^2/g as compared to pristine $BiVO_4$ (1.62 m^2/g). The increase in the BET surface area can be attributed to the Zn doping in $BiVO_4$, which may change the cell parameters of the $BiVO_4$. The larger BET area of

the Zn doped $BiVO_4$ can provide more active sites for the photocatalytic process and thus contribute significantly in the photocatalytic reaction [160].

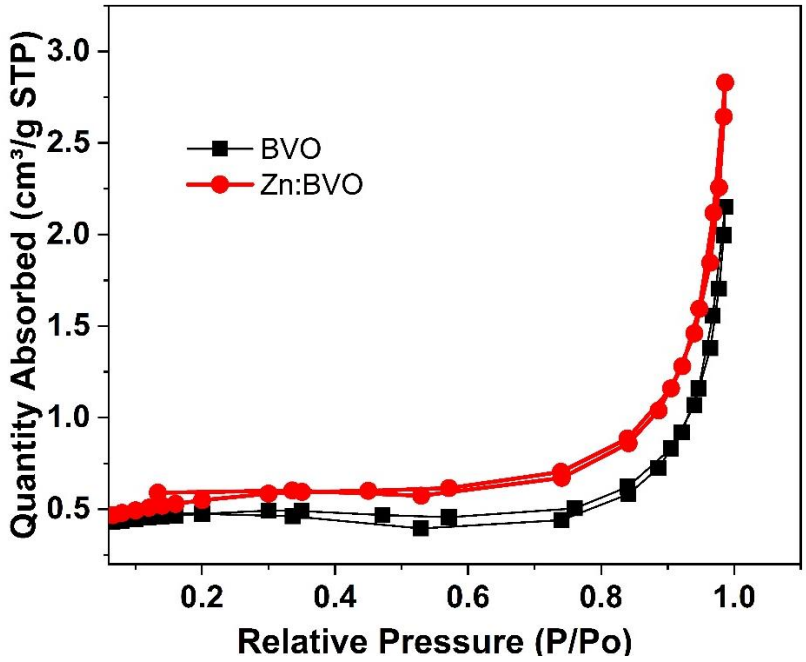

Figure 4. 5. BET surface area of the pristine compared to 2% Zn doped $BiVO_4$, where the Zn-doped displays a higher surface area than pristine.

4.5 Scanning electron microscopy (SEM)

The morphology and sizes of the samples were examined by using scanning electron microscopy (SEM). The SEM images of as prepared and Zn doped $BiVO_4$ are shown in Figure 4.6, where the pure shows agglomeration of particles. The pure BVO shows a group of particles joined together having rod-like morphology. The rod-like particle has an average length and width of 620 and 300 nm respectively. The agglomeration of $BiVO_4$ particles remained the same after 1% Zn doping but the morphology of particles slightly changed, where the average length and width of the nanorods decreased to 417 and 279 nm respectively [115]. After adding 2% Zn dopants to the $BiVO_4$, agglomeration of the particles slightly decreased and the morphology further changed to circular-shaped particles with an average length and width size of 370 nm. Finally, after adding 3% Zn dopants to the $BiVO_4$ structure the length increased to 535 nm, and the width of the particles reduced to, 317 nm. The particle sizes of all the samples are shown in Table 4.1.

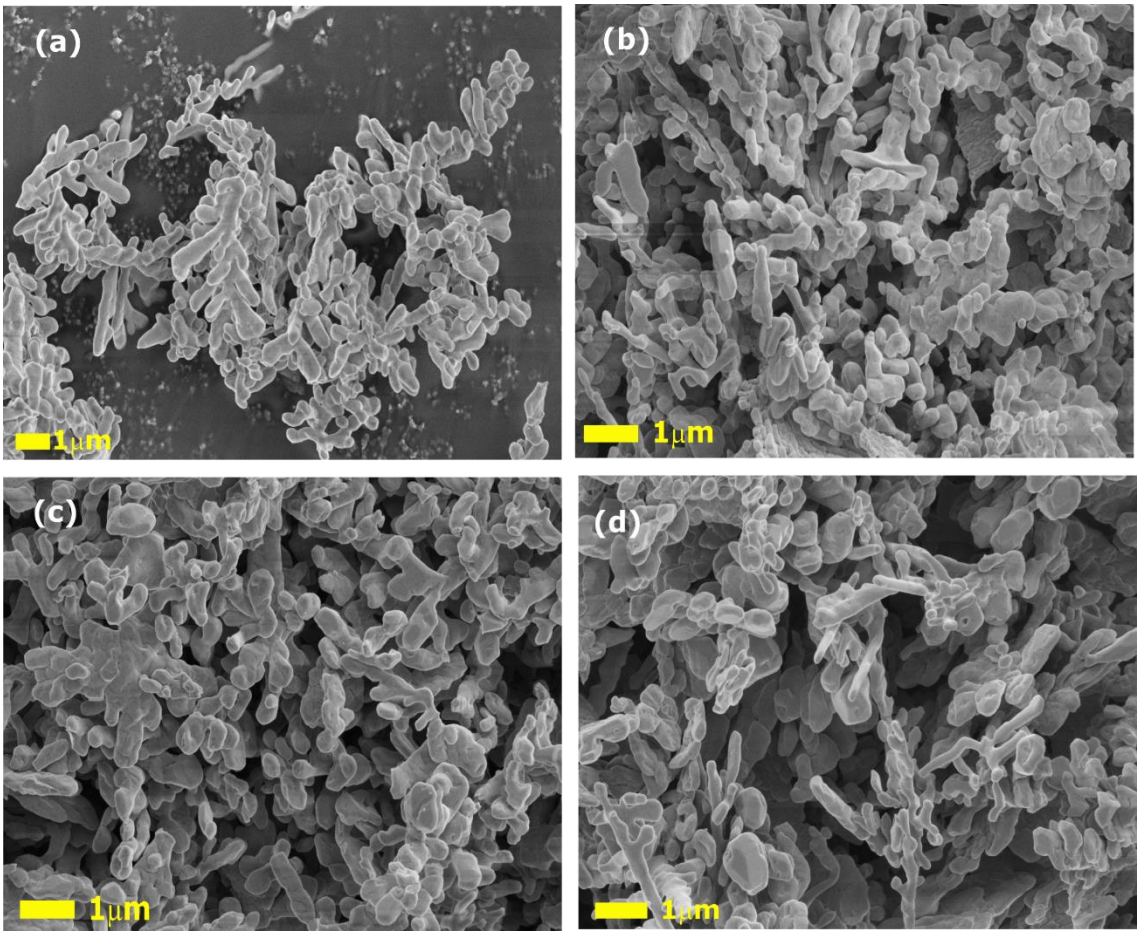

Figure 4. 6. SEM images of (a) pure, (b) 1% Zn-doped $BiVO_4$, (c) 2% Zn-doped $BiVO_4$, and (d) 3% Zn-doped $BiVO_4$.

4.6 X-ray photoelectron spectroscopy (XPS) of Zn-doped $BiVO_4$

The chemical states of the Zn-doped BVO were determined using X-ray photoelectron spectroscopy (XPS). Figure 4.7 displays XPS survey spectra of pristine, 1%, 2%, and 3% Zn doped $BiVO_4$, indicating that all doped samples contained Bi, V, O, C, and Zn elements. Also, high-resolution XPS spectra of Bi4f, V2p, O1s, and Zn2p for all doped samples are shown in Figure 4.8. For the pure BVO, two split peaks i.e. Bi 4f 5/2 and Bi 4f 7/2 were observed at binding energies (B.Es) of 164.5 and 159.2 eV which were assigned to the Bi^{3+} oxidation state. The V 2p 1/2 and V 2p 3/2 split peaks for the pure BVO observed at B.Es of 524.6 eV and 516.8 eV attributed to V^{5+}. The given B.Es of Bi 4f and V 2p split peaks correspond to the formation of bismuth vanadate ($BiVO_4$) [127]. The three fitted O1s peaks that appeared at B.Es of 532.7, 531.3, and

529.9 eV were assigned to oxygen in the $BiVO_4$ lattice, oxygen defects in the semiconductor, and chemisorbed oxygen respectively [84].

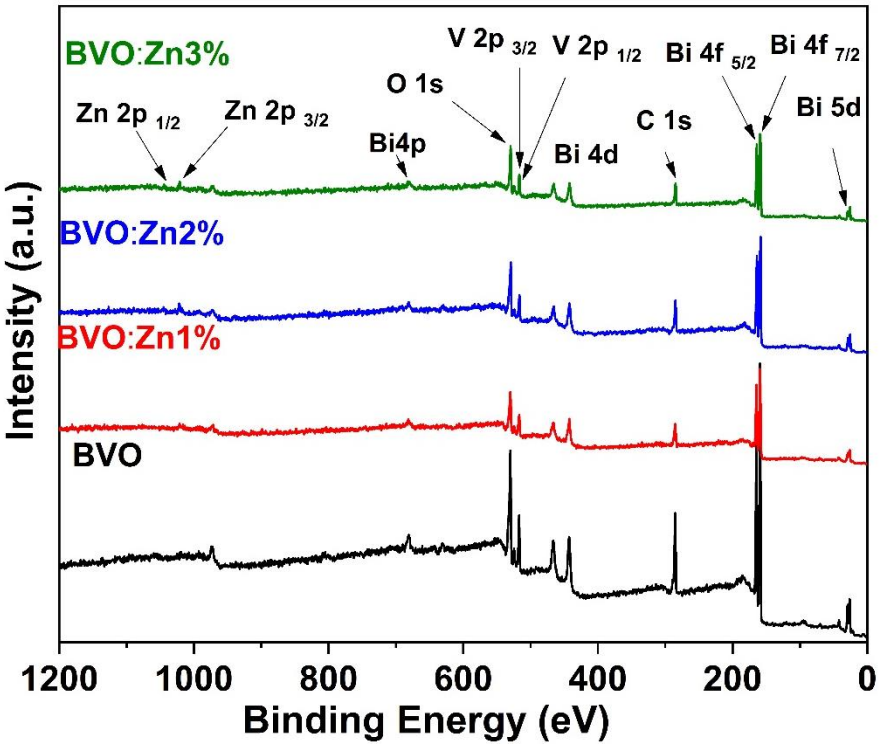

Figure 4. 7. XPS survey spectra of 1%, 2%, and 3% Zn doped $BiVO_4$

The Zn doping in $BiVO_4$ induced oxygen vacancies (O_V) as shown in Figure 4.8c where the O_V increased with increasing concentration of Zn. The O_V has an impact on the electronic structure of $BiVO_4$, inducing charge transition levels. The charge transition level further helps in reducing recombination sites and increases the conductivity of $BiVO_4$ which further enhances photocatalytic activity [128,151]. Additionally, the B.Es for Bi 4f, V2p, and O1s were shifted to lower values for the Zn-doped $BiVO_4$. The shift in the B.Es can be related to the closer interaction of Bi^{+3} (0.111nm), V^{+5} (0. 035 nm), and Zn^{+2} (0.083 nm) atoms because of different ionic radii sizes [151]. The shift in the B.Es and the Zn dopant sites can also be confirmed from Figure 4.8d, where the Zn peaks shifted to a lower value, and the visibility of peaks increased with increasing concentration of Zn in $BiVO_4$. Figure 4.8a further shows that the oxidation state of Bi^{3+} changed because of the breaking of the B-O bond at the surface of $BiVO_4$ particles, which results removal of oxygen atoms therefore forming oxygen vacancies (O_V) [161]. Similarly, in V 2p spectra a

shoulder at lower binding energies is observed for the BVO:Zn1% and BVO:Zn2% samples which should be attribution to the formation of V^{4+} species (Figure 4.8b)

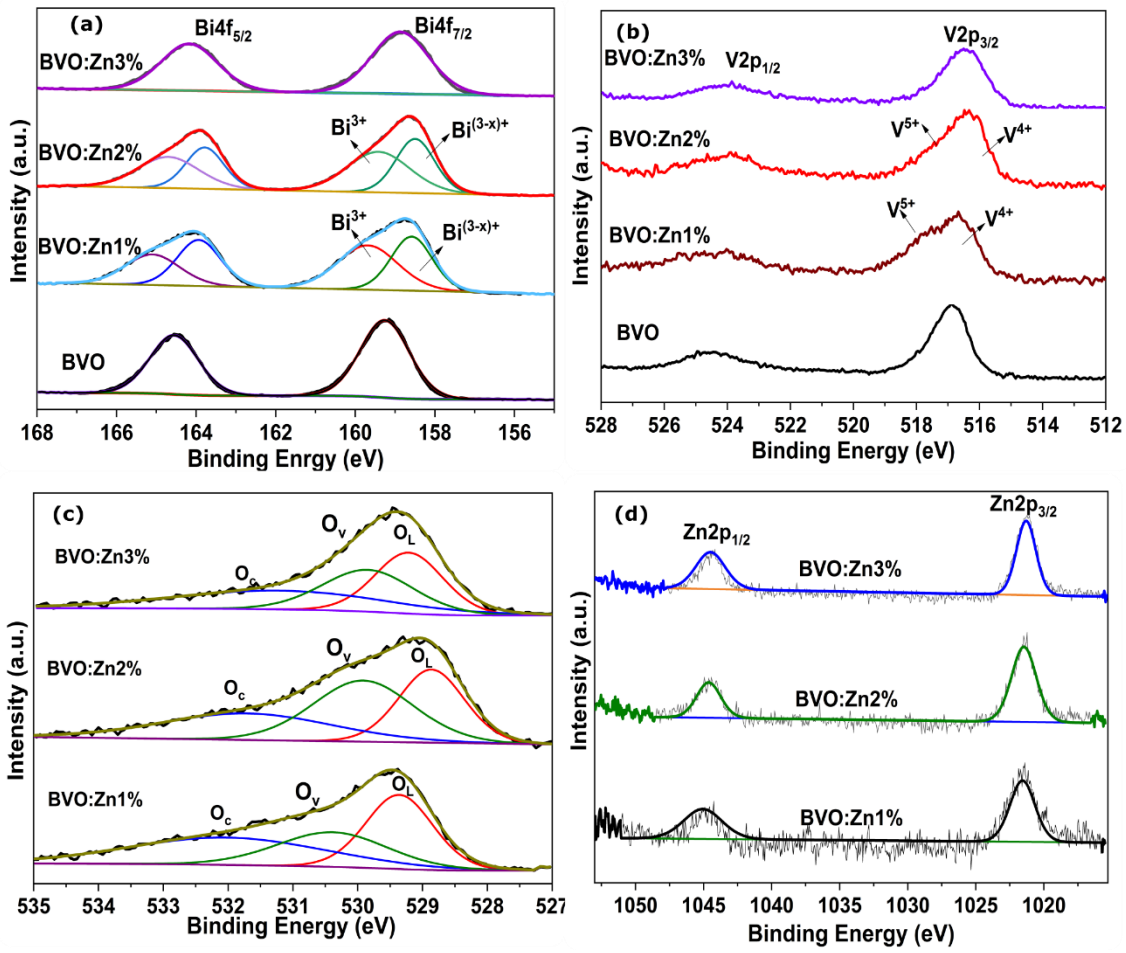

Figure 4. 8. XPS plot of (a) Bi, (b) V, (c) Zn, and (d) O1s for pure and 1%, 2%, and 3% Zn doped $BiVO_4$, representing a shift towards lower binding energies.

4.6.1 X-ray photoelectron spectroscopy (XPS) of Zn doped $BiVO_4$ loaded with $FeMnO_x$ cocatalyst

X-ray diffraction spectra of Zn-doped $BiVO_4$ loaded with the $FeMnO_x$ cocatalyst were also studied. For the Zn:BVO, two split peaks i.e. Bi 4f 5/2 and Bi 4f 7/2 were observed at binding energies (B.Es) of 164.0 and 158.6 eV which were assigned to the Bi^{3+} oxidation state. The V 2p 1/2 and V 2p 3/2 split peaks for the Zn:BVO observed at B.Es of 524.0 eV and 516.3 eV attributed to V^{5+}.The binding energies (B.Es) for Bi4f, V2P, and O1s were shifted to higher values for the Zn-doped $BiVO_4$ loaded with $FeMnO_x$ cocatalyst (Figure 4.9).

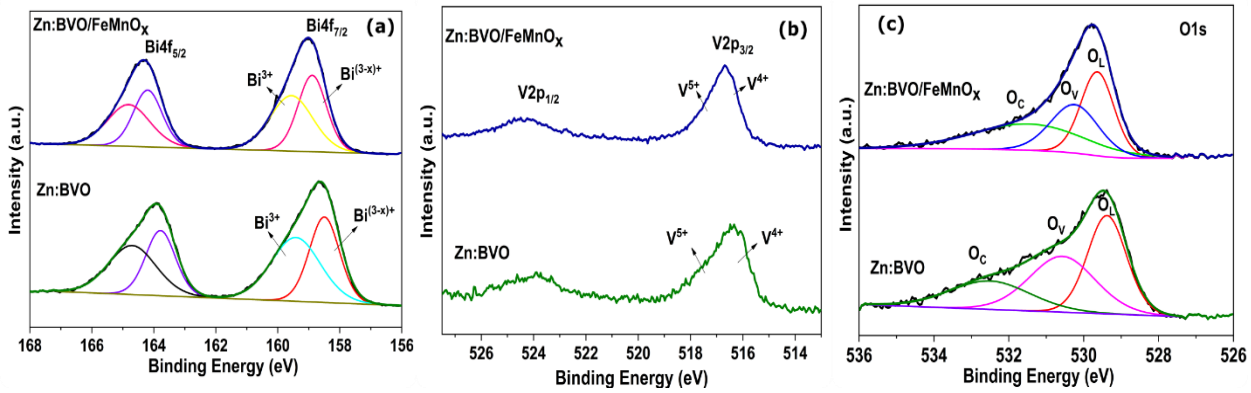

Figure 4. 9. XPS spectra of Zn doped $BiVO_4$ loaded with $FeMnO_x$ (a) Bi, (b) V, and (c) O1s, showing a shift towards higher binding energies concerning 2 % Zn doped $BiVO_4$.

The shift towards higher binding energies is due to the strong interaction of Zn-doped $BiVO_4$ and $FeMnO_x$ cocatalyst. The shift is probably due to the formation of p-n heterojunction by n-type $BiVO_4$ with p-type $FeMnO_x$ cocatalysts. The $FeMnO_x$ cocatalysts serve as *p*-type semiconductors and Zn doped $BiVO_4$ as *n*-type semiconductors; the Fermi level of the n-type semiconductor lies closer to the conduction band whereas the Fermi level of *p*-type closer to the valence band. Combining both types of semiconductors forms a p-n junction, thus causing band bending [132]. Band bending provides beneficial energetics for the migration and separation of photogenerated charge carriers [133,134]. Additionally, O1s fitted peaks appeared at B.Es of 532.1, 530.4, and 529.4 eV were assigned to oxygen in $BiVO_4$ lattice, oxygen defects in the semiconductor, and chemisorbed oxygen respectively [84]. The oxygen vacancies (O_v) were decreased after depositing $FeMnO_x$ cocatalyst on Zn-doped $BiVO_4$ as compared to Zn-doped $BiVO_4$, implying that O_v occupied by original O sites (Figure 4.9c) [162].

4.7 High Resolution Transmission Electron Microscopy (HRTEM)

The transmission electron microscopy (TEM) technique was used to further study the crystal structure and morphology of the photocatalyst shown in Figure 4.10a. The samples were dispersed in isopropanol and the dispersion was dropped onto a lacey grid with an ultra-thin closed C-film on a copper grid. It can be seen that the TEM image of the $BiVO_4$ (Figure 4.10a) photocatalyst is consistent with the SEM characterization result. From the high-resolution TEM (HRTEM) analysis of pure $BiVO_4$ and Zn:$BiVO_4$ (Figures 4.10b and 4.10c, respectively) and the corresponding

selected area diffraction pattern (SAED), we obtained a very similar d-spacing value of 0.309 nm for the (112) plane, characteristic of single-crystalline monoclinic $BiVO_4$. The HRTEM studies did not reveal any structural changes in the crystal structure between the $BiVO_4$ and the Zn:$BiVO_4$ particles. In Figure 4.10d, the HRTEM image of Zn:$BiVO_4$/$FeMnO_x$ (Figure 4.10d) shows a lattice structure consistent with the one for Zn:$BiVO_4$. Furthermore, it reveals further crystallites, which are marked in the white frame in the image. The evaluation of the FFT pattern confirmed the existence of single-crystalline $FeMnO_3$ with a d-spacing of 0.234 nm, which can be assigned to the (004) crystal plane. This demonstrates the effective deposition of $FeMnO_x$ onto the Zn-doped $BiVO_4$ nanoparticles. The high angle annular dark field (HAADF) - scanning transmission electron microscopy (STEM) image in Figure 4.10e illustrates an Zn:$BiVO_4$/$FeMnO_x$ agglomerate, and Figure 4.10f-h displays the corresponding elemental images of the sample. It can be seen that all the elements identified in the sample were homogeneously distributed. The uniform distribution of Fe and Mn on the Zn:$BiVO_4$ particles suggests that the deposition of $FeMnO_x$ by magnetron sputtering produced a layer with nanoparticles in a fine structure over the powder substrates. Overall, the HRTEM, STEM, and EDS results corroborated with previous XRD and XPS analyses.

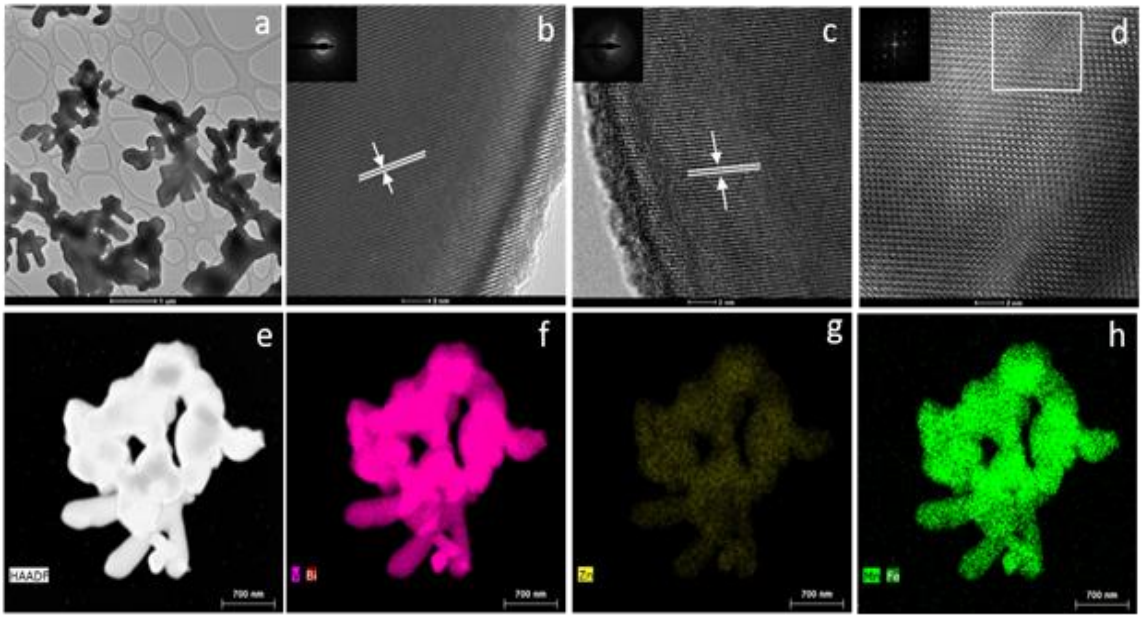

Figure 4. 10. (a) TEM image of pure $BiVO_4$; (b) HRTEM image of $BiVO_4$ and (c) Zn:$BiVO_4$, whereas the inset corresponds to the SAED patterns of the characteristic monoclinic $BiVO_4$ structure of the (112) planes; (d) HRTEM image of Zn:$BiVO_4$/$FeMnO_x$, whereas the inset show the SAED patterns and the white frame consists of the area of the FFT pattern, indicating the (004) plane of $FeMnO_3$; (e) HAADF-STEM image and (f-h) corresponding EDS mapping for Zn:$BiVO_4$/$FeMnO_x$.

4.8 Photocatalytic Oxygen (O_2) Evolution

The photocatalytic response of the different photocatalysts was tested for oxygen (O_2) evolution. The $Fe(NO_3)_3.9H_2O$ (50 mM) solution was used as a sacrificial agent during the photocatalytic O_2 evolution. The oxygen evolution of 1%, 2%, and 3% Zn-doped $BiVO_4$ samples is shown in Figure 4.11a, where all samples were irradiated with solar light for 3 h. The oxygen evolution was increased to 135 μmol for the Zn:BVO sample when compared to as prepared BVO (90 μmol). The higher oxygen evolution of the Zn:BVO was attributed to the doping of Zn in $BiVO_4$ which helped to further increase the 040 facets, thus increasing photocatalytic activity. Furthermore, the crystallinity and V-O bond length of $BiVO_4$ increases upon doping with Zn, which also boosts photocatalytic activity. The reduced band gap of the $BiVO_4$ is also an important factor for the improved photocatalytic activity. The Zn dopants in the $BiVO_4$ reduce the band gap energies; thus, improving photocatalytic activity [97,156,157]. The photocatalytic oxygen evolution was increased with the increasing concentrations of Zn in $BiVO_4$; however, the higher concentrations of Zn reduced the photocatalytic activity. The decrease in photocatalytic activity is probably due to a large amount of Zn dopants in the $BiVO_4$, leading to the unit cell shrinkage which further reduces the V-O bond length and crystallinity thus decreasing photocatalytic activity [163]. The bimetallic $FeMnO_x$ and $FeNiO_x$ cocatalysts were deposited on Zn:BVO which further helped in increasing photocatalytic activity. The $FeMnO_x$ further improved the photocatalytic O_2 to 154 μmol but for the $FeNiO_x$ cocatalysts, the photocatalytic oxygen evolution remains the same (134 μmol) as shown in Figure 4.11b. The lower photocatalytic activity of the Zn:BVO loaded with $FeNiO_x$ sample is due to the lower space charge region (SCR), which is characterized by a lower built-in electric field than Zn:BVO loaded with $FeMnO_x$ [17]. The increase in the photocatalytic O_2 was attributed to the p-n junction formed by p-type $FeMnO_x$ and n-type $BiVO_4$ which provide a built-in electric field to further increase the charge transfer and reduce charge recombination. Furthermore, the $FeMnO_x$ helps to take the holes from the surface of the $BiVO_4$ to suppress charge recombination and improve the charge transfers [125,141]. The evolved oxygen for all 1%, 2%, and 3% Zn doped $BiVO_4$, and 2 % Zn doped $BiVO_4$ loaded with $FeMnO_x$, and $FeNiO_x$ cocatalysts is shown in Table 4.3.

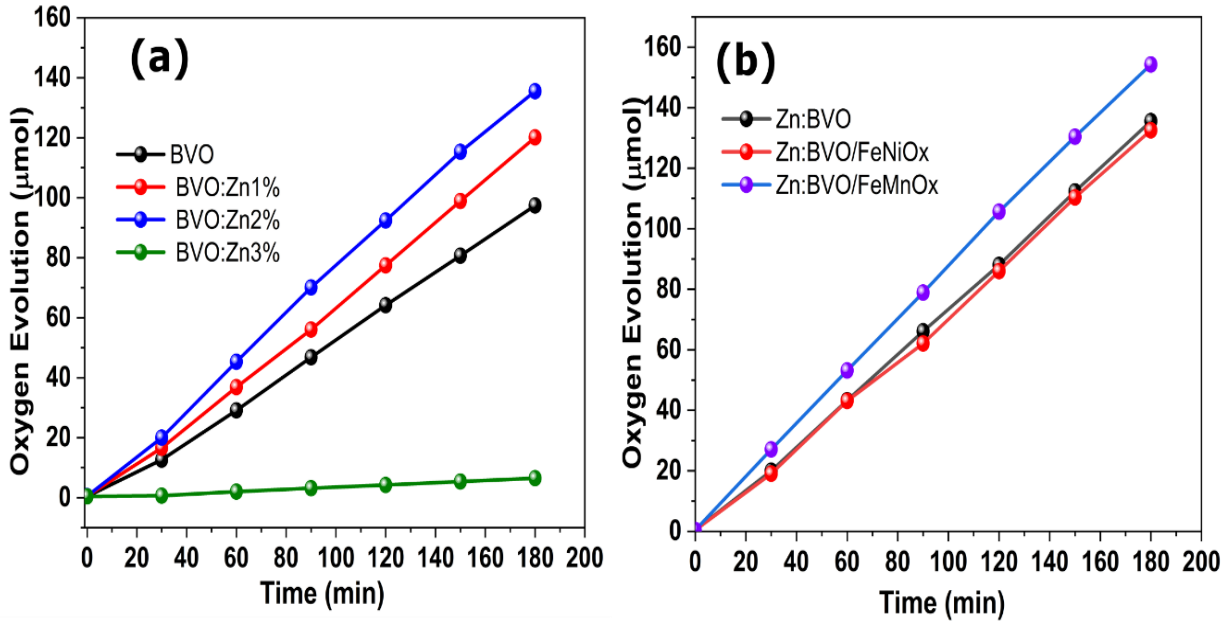

Figure 4. 11. Oxygen evolution of (a) pure Zn-doped $BiVO_4$, and (b) the Zn-doped $BiVO_4$ loaded with $FeMnO_x$ and $FeNiO_x$ cocatalysts. The 2%Zn doped $BiVO_4$ loaded with $FeMnO_x$ (Zn:BVO/$FeMnO_x$) showed higher oxygen evolution than the rest of the samples.

Table 4.3. Photocatalytic oxygen evolution of all sample exposure for 3 hours to 300 W Xe radiation filtered with AM 1.5G filter.

S.NO	Sample Description	Sample ID	Oxygen Evolution (µmol)
1	$BiVO_4$	BVO	1200 µmol $g^{-1}h^{-1}$
2	1% Zn doped $BiVO_4$	1%Zn:BVO	1600 µmol $g^{-1}h^{-1}$
3	2% Zn doped $BiVO_4$	2%Zn:BVO	1800 µmol $g^{-1}h^{-1}$
4	3% Zn doped $BiVO_4$	3%Zn:BVO	93 µmol $g^{-1}h^{-1}$
5	2% Zn doped $BiVO_4$ loaded with $FeNiO_x$ for 10 min	Zn:BVO/ $FeNiO_x$	1786 µmol $g^{-1}h^{-1}$
6	2% Zn doped $BiVO_4$ loaded with $FeMnO_x$ for 10 min	Zn:BVO/ $FeMnO_x$	2053µmol $g^{-1}h^{-1}$

4.9 Density Functional Theory (DFT) Calculations Results

The electronic properties of monoclinic $BiVO_4$ were calculated form the optimized structure geometry. Figure 4.12a reveals that the $BiVO_4$ has an indirect band gap of 2.1 eV which is closely matched with previously reported works [110,164–166]. Similarly, Zn doped $BiVO_4$ shows a direct band gap~1.1 eV (Figure 4.12b). The partial density of states (PDOS) results of the pure $BiVO_4$ further elucidating that the O-2p and V-3d orbitals are more dominant in valence band (V.B) and conduction band (C.B). Additionally, the PDOS for the pure $BiVO_4$ also confirming that the Bi 6s orbitals are present in V.B and Bi 6p orbitals are present in C.B (Figure 11c) [110,166].

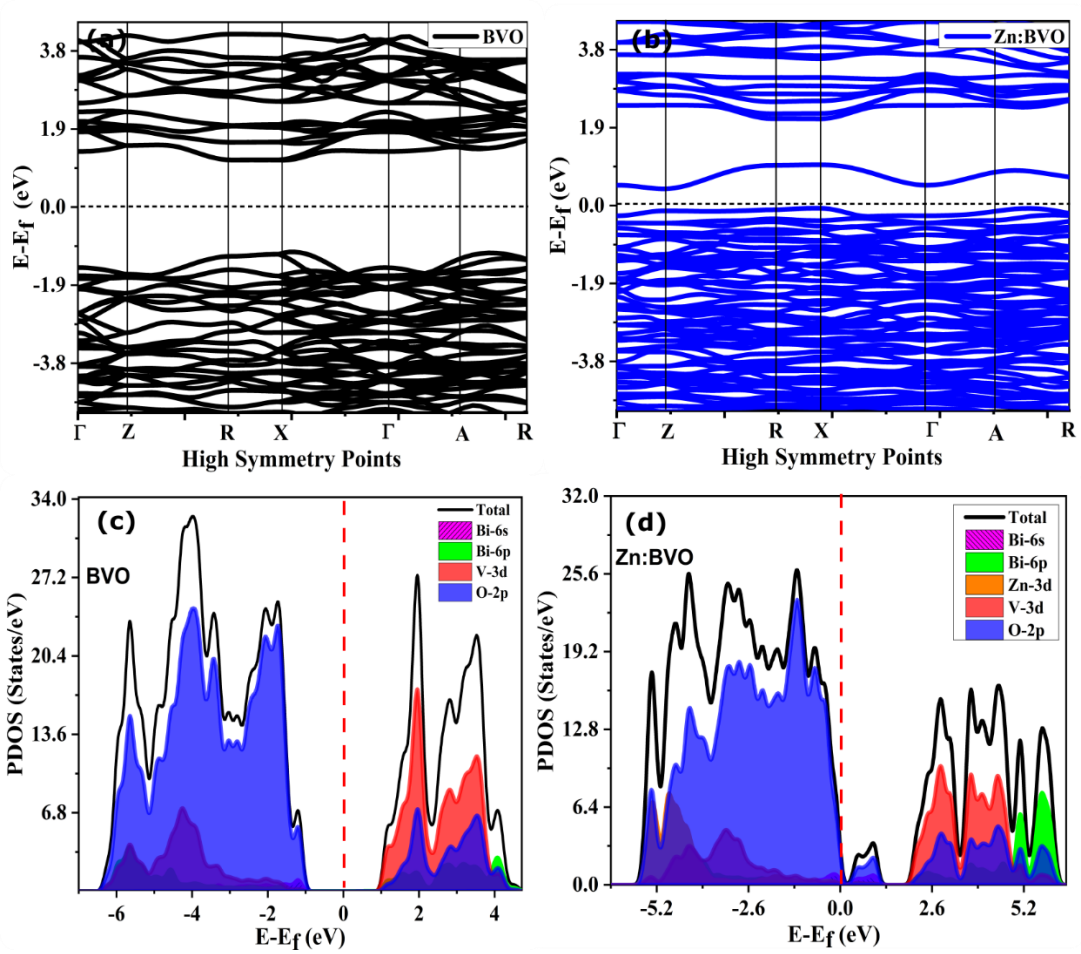

Figure 4. 12 (a) Band structure of pure $BiVO_4$ showing indirect band gap at X and R high symmetry points (b) band structure of Zn doped $BiVO_4$ reveals a direct band gap at X, (c) PDOS of pure $BiVO_4$, (d) PDOS of Zn $BiVO_4$.

The PDOS results for the Zn doped $BiVO_4$ show that the Zn atom contributes to both V.B and C.B by creating extra states close to the V.B (Figure 4.12d). The extra states contribute to reducing the

band gap energy and boosting the majority charge carries, thus improving the photocatalytic activity [167]. Furthermore, the extra states (sub-states) are formed by the major contribution of O orbitals above the V.B which is consistent with XPS results. The PDOS results indicate that the V.B and C.B orbitals distribution for the pure and Zn doped $BiVO_4$ are similar. However, the Fermi level is near to the V.B for the Zn doped $BiVO_4$, which is due to an extra electrons of the Zn atom. Furthermore, the closeness of the Fermi level to the V.B explains the *p*-type nature of the Zn doped $BiVO_4$. WJ Yin et all have suggested that the *p*-type conductivity of the $BiVO_4$ is due to doping under oxygen-rich conditions [168]. Figure 4.13 shows that the Zn dopants in the $BiVO_4$ caused a shift in the Fermi level towards lower energy which is also consistent with the XPS results.

The deposition of bimetallic iron-manganese ($FeMnO_x$) atoms on the Zn doped $BiVO_4$ was also confirmed by DFT calculation. The results represent that the $FeMnO_x$ cocatalysts oxidize after the adsorption on Zn doped $BiVO_4$ which is due to its interaction with oxygen atoms in the Zn doped $BiVO_4$ (Figure 4.14). The adsorption of the $FeMnO_x$ cocatalysts on Zn doped $BiVO_4$, caused a shift in the Fermi level toward higher energy which is also similar to the XPS results.

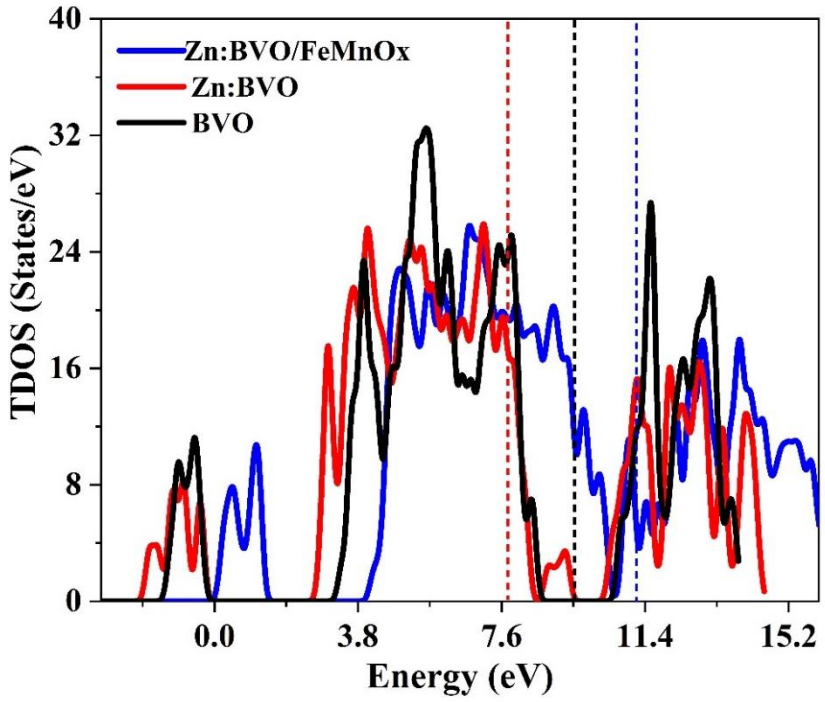

Figure 4. 13. Total density of states (TDOS) of BVO, Zn:BVO, and Zn:BVO/$FeMnO_x$.

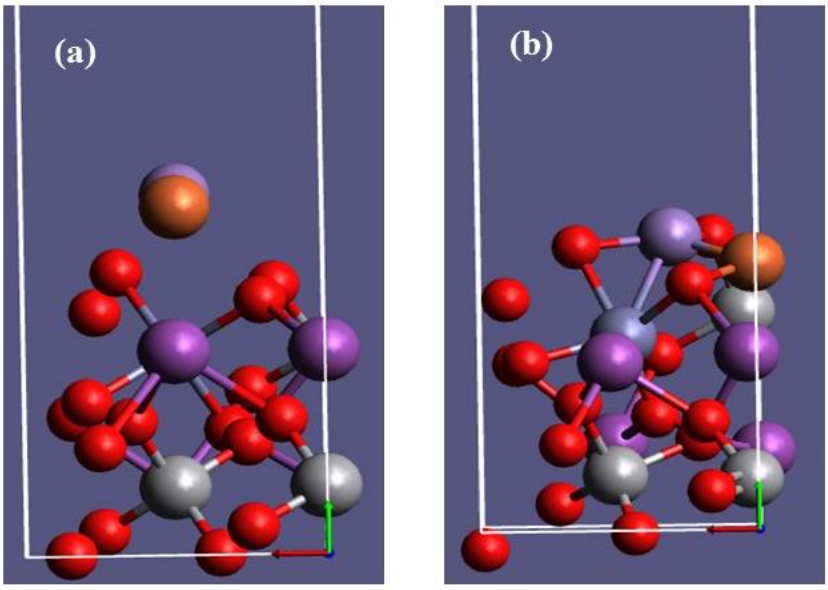

Figure 4. 14. (a) Before the adsorption of $FeMnO_x$ on Zn doped $BiVO_4$, and (b) after the adsorption of $FeMnO_x$ on Zn doped $BiVO_4$

Importantly, the adsorption of bimetallic $FeMnO_x$ cocatalysts enhances the charge density distribution as compared to Zn:BVO, as it creates more defects close to the Fermi level. These defects are beneficial for the photocatalytic activity of photocatalysts, as they delay the charge recombination time, thus improving photocatalytic performance [169]. The electron localization function (ELF) was conducted to further see the local electron distribution and chemical bonding of the system. ELF produces values in the range of 0 to 1, where 1 indicates higher localization of the electrons and 0 indicates complete delocalization of the electrons or no electrons present in the region. Similarly, a 0.5 value represents the uniform distribution of the electrons. Figure 4.15 displays the ELF for the pure, Zn:BVO, and Zn:BVO/$FeMnO_x$, where the Zn:BVO, and Zn:BVO/$FeMnO_x$ have red colored areas as compared to the pure $BiVO_4$, which represents the higher probability of electrons localization [170].

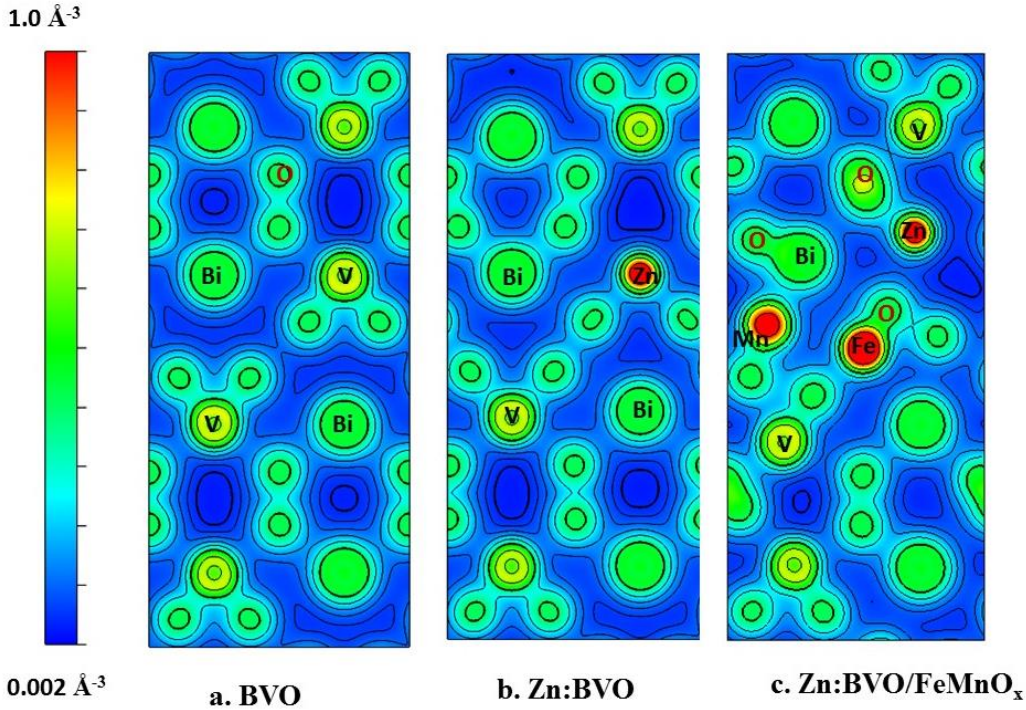

Figure 4. 15. Electron localization function (ELF) for (a) pure, (b) Zn doped $BiVO_4$, and (c) Zn doped $BiVO_4$ loaded with $FeMnO_x$ cocatalysts.

Chapter 5

5. Conclusion and Future Recommendations

5.1 Conclusion

In summary, the RF-magnetron sputtering technique was used to deposit a different kind of bimetallic $FeMnO_x$ and $FeNiO_x$ cocatalysts on hydrothermally prepared pure and tungsten doped $BiVO_4$ powder to enhance its photocatalytic activity. The photocatalytic activity of pure and W-doped BVO was tested for oxygen evolution which was improved to 160 μmol as compared to the pure BVO (93 μmol). The enhancement in oxygen evolution was attributed to the high exposure of the facet (040) of the tungsten-doped $BiVO_4$. The growth of the (040) facet can be confirmed from the ratio (040/110) facets, which increased for the W-doped $BiVO_4$ samples as compared to the as-prepared BVO. The rise in O_2 evolution can also be related to the high charge transport efficiency in the bulk of $BiVO_4$ because of W doping. $BiVO_4$ has two doping sites i.e. the Bi^{+3} site and V^{+5} site, doping of a hexavalent impurity (W^{+6}) to the V site donates more electrons thus increasing n-type conductivity which improves photo response. Additionally, W dopant in the $BiVO_4$ promotes the O_V, and these vacancies enhanced the electron density near the bottom of the conduction band. The oxygen vacancies (O_V) are responsible for the electronic structure of $BiVO_4$, by inducing charge transition levels which further help to reduce recombination sites and increase the conductivity of $BiVO_4$, thus improving photocatalytic activity. The photocatalytic activity was further improved by loading $FeMnO_x$ and $FeNiO_x$ cocatalysts on pure and W-doped BVO (W:BVO). The loading of $FeMnO_x$ and $FeNiO_x$ cocatalysts on pure BVO further improved the photocatalytic O_2 evolution to 146 and 130 μmol. Furthermore, when the $FeMnO_x$ and $FeNiO_x$ were deposited on W:BVO the photocatalytic oxygen was boosted to 181 and 175 μmol. The improvement in the photocatalytic oxygen evolution was related to the p-n junction made by the *n*-type $BiVO_4$ and *p*-type $FeMnO_x$ and $FeNiO_x$ cocatalysts. The *p*-type $FeMnO_x$ and $FeNiO_x$ cocatalysts have different Fermi levels than *n*-type $BiVO_4$; thus, combing materials with different Fermi levels causes band bending and induces an electric field. The induced electric field improves charge transfer kinetics; thereby, improving photocatalytic oxygen evolution.

Pure and zinc (Zn) doped $BiVO_4$ were also synthesized using a hydrothermal route and then deposited $FeMnO_x$ cocatalysts on Zn doped $BiVO_4$ using RF-magnetron sputtering to form a

heterojunction. The photocatalytic response of pure and Zn-doped $BiVO_4$ was tested for oxygen evolution by directly exposing the $BiVO_4$ solution to a 300 Xe lamp with an AM 1.5 G filter for 3 h. The photocatalytic oxygen (O_2) evolution was enhanced to 135 μmol as compared to the pure $BiVO_4$ (90 μmol). The higher oxygen evolution of the Zn:BVO was attributed to the doping of Zn in $BiVO_4$ which helped to further increase the 040 facets, thus increasing photocatalytic activity. Furthermore, the crystallinity and V-O bond length of $BiVO_4$ increases upon doping with Zn, which also boosts the photocatalytic activity. The reduced band gap of the $BiVO_4$ is also an important factor for the improved photocatalytic activity. The Zn dopants in the $BiVO_4$ reduce the band gap energies; thus, improving photocatalytic activity. The loading of $FeMnO_x$ on Zn-doped $BiVO_4$ (Zn:BVO) further improved photocatalytic O_2 evolution to 154 μmol. The increase in the photocatalytic O_2 was attributed to the p-n junction formed by *p*-type $FeMnO_x$ and *n*-type Zn doped $BiVO_4$ which provide a built-in electric field to further increase the charge transfer and reduce charge recombination. Additionally, $FeMnO_x$ cocatalysts on the $BiVO_4$ surface can provide more active sites for water oxidation reactions. Therefore, it helps in suppressing charge recombination and improving charge transfer at the surface of $BiVO_4$ photocatalysts leading to better photocatalytic oxygen evolution. DFT calculations have also shown that doping Zn in $BiVO_4$ reduced band gap and increased absorption of visible light, resulting increase in photocatalytic O_2 evolution. It was also confirmed from the DFT calculations that depositing $FeMnO_x$ on Zn doped $BiVO_4$ shifted Fermi levels and induced more charges to boost the photocatalytic reaction.

5.2 Future Recommendations

$BiVO_4$ has shown stable and versatile morphologies with optimal electronic and optical properties for photocatalysis. The photocatalytic properties of the pristine $BiVO_4$ were further improved by metallic doping as well as loading $FeMnO_x$ and $FeNiO_x$ cocatalysts. However, some experimental results need to be improved for better photocatalytic activity.

1. Loading the same cocatalysts to the pristine and doped $BiVO_4$ using other synthesis techniques.
2. We used RF-magnetron sputtering to deposit $FeMnO_x$ and $FeNiO_x$ cocatalysts at pristine and doped $BiVO_4$ interfaces. Therefore one should apply hydrothermal synthesis to deposit these cocatalysts, which may result in better photocatalytic activity.

3. The combination of these photocatalysts at pristine and doped $BiVO_4$ may result in an excellent photocatalytic response.
4. Depositing $FeMnO_x$ and $FeNiO_x$ cocatalysts on other metallic doped $BiVO_4$ like Mo may improve the photocatalytic response.

References

[1] S.R. Lingampalli, M.M. Ayyub, C.N.R. Rao, Recent Progress in the Photocatalytic Reduction of Carbon Dioxide, ACS Omega. 2 (2017) 2740–2748. https://doi.org/10.1021/ACSOMEGA.7B00721.

[2] S. Obregón, A. Caballero, G. Colón, Hydrothermal synthesis of BiVO 4: Structural and morphological influence on the photocatalytic activity, Applied Catalysis B: Environmental. 117–118 (2012) 59–66. https://doi.org/10.1016/j.apcatb.2011.12.037.

[3] N. Khan, F. Stelo, G.H.C. Santos, L.M. Rossi, R. V. Gonçalves, H. Wender, Recent advances on Z-scheme engineered BiVO4-based semiconductor photocatalysts for CO2 reduction: A review, Applied Surface Science Advances. 11 (2022) 100289. https://doi.org/10.1016/J.APSADV.2022.100289.

[4] E. Lewis, O. Chamel, M. Mohsenin, E. Ots, E.T. White, Intergovernmental Panel on Climate Change, in: Sustainaspeak, Routledge, New York : Routledge, 2018., 2018: pp. 153–154. https://doi.org/10.4324/9781315270326-109.

[5] K. Trenberth, A. Dai, … G.V.D.S.-N.C., undefined 2014, Global warming and changes in drought, Nature.Com. (n.d.). https://www.nature.com/articles/nclimate2067 (accessed March 8, 2023).

[6] N.S. Lewis, Toward Cost-Effective Solar Energy Use, Science. 315 (2007) 798–801. https://doi.org/10.1126/science.1137014.

[7] Y. Park, K.J. Mc Donald, K.S. Choi, Progress in bismuth vanadate photoanodes for use in solar water oxidation, Chemical Society Reviews. 42 (2013) 2321–2337. https://doi.org/10.1039/c2cs35260e.

[8] J. Guo, X. Liao, M.-H. Lee, G. Hyett, C.-C. Huang, D.W. Hewak, S. Mailis, W. Zhou, Z. Jiang, Experimental and DFT insights of the Zn-doping effects on the visible-light photocatalytic water splitting and dye decomposition over Zn-doped BiOBr photocatalysts, Applied Catalysis B: Environmental. 243 (2019) 502–512. https://doi.org/10.1016/j.apcatb.2018.09.089.

[9] M.G. Walter, E.L. Warren, J.R. McKone, S.W. Boettcher, Q. Mi, E.A. Santori, N.S. Lewis, Solar water splitting cells, Chemical Reviews. 110 (2010) 6446–6473. https://doi.org/10.1021/cr1002326.

[10] Y. Hu, J. Fan, C. Pu, H. Li, E. Liu, X. Hu, Facile synthesis of double cone-shaped Ag4V2O7/BiVO4 nanocomposites with enhanced visible light photocatalytic activity for environmental purification, Journal of Photochemistry and Photobiology A: Chemistry. 337 (2017) 172–183. https://doi.org/10.1016/j.jphotochem.2016.12.035.

[11] L. Zhang, H. Wang, Z. Chen, P.K. Wong, J. Liu, Bi2WO6 micro/nano-structures: Synthesis, modifications and visible-light-driven photocatalytic applications, Applied Catalysis B: Environmental. 106 (2011) 1–13. https://doi.org/10.1016/j.apcatb.2011.05.008.

[12] L. Zhang, H. Wang, Z. Chen, P.K. Wong, J. Liu, Bi2WO6 micro/nano-structures: Synthesis, modifications and visible-light-driven photocatalytic applications, Applied

Catalysis B: Environmental. 106 (2011) 1–13. https://doi.org/10.1016/j.apcatb.2011.05.008.

[13] W.H. Glaze, J.W. Kang, D.H. Chapin, The chemistry of water treatment processes involving ozone, hydrogen peroxide and ultraviolet radiation, Ozone: Science & Engineering. 9 (1987) 335–352. https://doi.org/10.1080/01919518708552148.

[14] P. Zhang, J. Zhang, J. Gong, Tantalum-based semiconductors for solar water splitting, Chemical Society Reviews. 43 (2014) 4395–4422. https://doi.org/10.1039/c3cs60438a.

[15] S. Zhu, D.W.-A.E. Materials, undefined 2017, Photocatalysis: basic principles, diverse forms of implementations and emerging scientific opportunities, Wiley Online Library. 7 (2017). https://doi.org/10.1002/aenm.201700841.

[16] A. FUJISHIMA, K. HONDA, Electrochemical Photolysis of Water at a Semiconductor Electrode, Nature. 238 (1972) 37–38. https://doi.org/10.1038/238037a0.

[17] A.S. Correa, L.G. Rabelo, W.S. Rosa, N. Khan, S. Krishnamurthy, S. Khan, R. V. Gonçalves, Interfacial band alignment and photoelectrochemical properties of all-sputtered $BiVO_4$/$FeNiO_x$ and $BiVO_4$/$FeMnO_x$ p–n heterojunctions, Energy Advances. (2023). https://doi.org/10.1039/D2YA00247G.

[18] C. Suarez, S. Hernández, N.R.-A.C.A. General, undefined 2015, BiVO4 as photocatalyst for solar fuels production through water splitting: a short review, Elsevier. (n.d.). https://www.sciencedirect.com/science/article/pii/S0926860X14007510 (accessed June 1, 2022).

[19] J. Tang, J.R. Durrant, D.R. Klug, Mechanism of photocatalytic water splitting in TiO2. Reaction of water with photoholes, importance of charge carrier dynamics, and evidence for four-hole chemistry, Journal of the American Chemical Society. 130 (2008) 13885–13891. https://doi.org/10.1021/JA8034637.

[20] J. Yang, D. Wang, X. Zhou, C. Li, A Theoretical Study on the Mechanism of Photocatalytic Oxygen Evolution on BiVO4 in Aqueous Solution, Chemistry – A European Journal. 19 (2013) 1320–1326. https://doi.org/10.1002/CHEM.201202365.

[21] I. Roger, M. Shipman, M.S.-N.R. Chemistry, undefined 2017, Earth-abundant catalysts for electrochemical and photoelectrochemical water splitting, Nature.Com. (n.d.). https://www.nature.com/articles/s41570-016-0003/briefing/signup/ (accessed January 5, 2023).

[22] J. Kim, J.L.-A. Materials, undefined 2019, Elaborately Modified BiVO4 Photoanodes for Solar Water Splitting, Wiley Online Library. 31 (2019). https://doi.org/10.1002/adma.201806938.

[23] A. Kudo, Y. Miseki, Heterogeneous photocatalyst materials for water splitting, Chemical Society Reviews. 38 (2009) 253–278. https://doi.org/10.1039/b800489g.

[24] K. Rajeshwar, Hydrogen generation at irradiated oxide semiconductor-solution interfaces, Journal of Applied Electrochemistry. 37 (2007) 765–787. https://doi.org/10.1007/S10800-007-9333-1.

[25] A. Fernández, G. Lassaletta, V.M. Jiménez, A. Justo, A.R. González-Elipe, J.M. Herrmann, H. Tahiri, Y. Ait-Ichou, Preparation and characterization of TiO2 photocatalysts supported on various rigid supports (glass, quartz and stainless steel). Comparative studies of photocatalytic activity in water purification, Applied Catalysis B, Environmental. 7 (1995) 49–63. https://doi.org/10.1016/0926-3373(95)00026-7.

[26] L. Jiang, L. Gao, Fabrication and characterization of ZnO-coated multi-walled carbon nanotubes with enhanced photocatalytic activity, Materials Chemistry and Physics. 91 (2005) 313–316. https://doi.org/10.1016/j.matchemphys.2004.11.028.

[27] S. Wu, H. Cao, S. Yin, X. Liu, X. Zhang, Amino acid-assisted hydrothermal synthesis and photocatalysis of SnO 2 nanocrystals, Journal of Physical Chemistry C. 113 (2009) 17893–17898. https://doi.org/10.1021/JP9068762.

[28] H. Xu, W. Wang, W. Zhu, Shape evolution and size-controllable synthesis of Cu2O octahedra and their morphology-dependent photocatalytic properties, Journal of Physical Chemistry B. 110 (2006) 13829–13834. https://doi.org/10.1021/JP061934Y.

[29] M. Ashokkumar, P. Maruthamuthu, Factors influencing the photocatalytic efficiency of WO3 particles, Journal of Photochemistry and Photobiology, A: Chemistry. 49 (1989) 249–258. https://doi.org/10.1016/1010-6030(89)87122-9.

[30] Z. Ai, L. Lu, J. Li, L. Zhang, J. Qiu, M. Wu, Fe@Fe2O3 Core-shell nanowires as iron reagent. 1. Efficient degradation of rhodamine by a novel sono-fenton process, Journal of Physical Chemistry C. 111 (2007) 4087–4093. https://doi.org/10.1021/JP065559L.

[31] A. Walsh, Y. Yan, M.N. Huda, M.M. Al-Jassim, S.H. Wei, Band edge electronic structure of BiVO 4: Elucidating the role of the Bi s and V d orbitals, Chemistry of Materials. 21 (2009) 547–551. https://doi.org/10.1021/CM802894Z.

[32] J. Li, L. Wang, X. Kong, B. Ma, Y. Shi, C. Zhan, Y. Qiu, A simple and efficient method using polymer dispersion to prepare controllable nanoporous TiO2 anodes for dye-sensitized solar cells, Langmuir. 25 (2009) 11162–11167. https://doi.org/10.1021/LA901488J.

[33] F. He, D. Zhou, X. Feng, C. Zhang, T. Li, G. Li, Solvothermal synthesis of rice-like TiO2 nanocrystals with enhanced photocatalytic activity, Materials Letters. 132 (2014) 1–3. https://doi.org/10.1016/j.matlet.2014.06.034.

[34] K.M. Garadkar, B.S. Shirke, P.P. Hankare, D.R. Path, Low cost nanostructured anatase TiO2 as a H2S gas sensor synthesized by microwave assisted technique, Sensor Letters. 9 (2011) 526–532. https://doi.org/10.1166/sl.2011.1507.

[35] N.C. Castillo, A. Heel, T. Graule, C. Pulgarin, Flame-assisted synthesis of nanoscale, amorphous and crystalline, spherical BiVO4 with visible-light photocatalytic activity, Applied Catalysis B: Environmental. 95 (2010) 335–347. https://doi.org/10.1016/j.apcatb.2010.01.012.

[36] A. Kudo, S. Hijii, H2 or O2 evolution from aqueous solutions on layered oxide photocatalysts consisting of Bi3+ with 6s2 configuration and d0 transition metal ions, Chemistry Letters. (1999) 1103–1104. https://doi.org/10.1246/CL.1999.1103.

[37] V.E. Levine, THE REDUCING PROPERTIES OF MICROÖRGANISMS WITH SPECIAL REFERENCE TO SELENIUM COMPOUNDS, Journal of Bacteriology. 10 (1925) 217–263. https://doi.org/10.1128/JB.10.3.217-263.1925.

[38] R. Roth, J. Waring, Synthesis and stability of bismutotantalite, stibiotantalite and chemically similar ABO4 compounds, The American Mineralogist. 18 (1963) 1348–1356. http://scholar.google.com/scholar?hl=en&btnG=Search&q=intitle:SYNTHESIS+AND+STABILITY+OF+BISMUTOTANTALITE,+STIBIOTANTALITE+AND+CHEMICALLY+SIMILAR+ABO4+COMPOUNDS#0 (accessed September 22, 2022).

[39] J.D. Bierlein, A.W. Sleight, Ferroelasticity in BiVO4, Solid State Communications. 16 (1975) 69–70. https://doi.org/10.1016/0038-1098(75)90791-7.

[40] C. Manolikas, S. Amelinckx, Ferroelastic domains in BiVO4, Physica Status Solidi (A). 60 (1980) 167–172. https://doi.org/10.1002/pssa.2210600120.

[41] T. Lu, B.C.H. Steele, Electrical conductivity of polycrystalline BiVO4 samples having the scheelite structure, Solid State Ionics. 21 (1986) 339–342. https://doi.org/10.1016/0167-2738(86)90196-7.

[42] D. Savastano, High performance pigments, Ink World. 10 (2004). https://books.google.com/books?hl=en&lr=&id=ecD6AuaJyFwC&oi=fnd&pg=PR5&dq=E.B.+Faulkner,+R.J.+Schwartz,+High+Performance+Pigments,+9+WILEY-VC,+WILEYVCH+Verlag+GmbH+%26+Co.+KGaA,+2009.&ots=J7wOFA3pw1&sig=TXOedzZpETfDwMVsrP9gDK1IRpU (accessed September 24, 2022).

[43] A. Kudo, K. Ueda, H. Kato, I. Mikami, Photocatalytic O2 evolution under visible light irradiation on BiVO4 in aqueous AgNO3 solution, Catalysis Letters. 53 (1998) 229–230. https://doi.org/10.1023/A:1019034728816.

[44] A. Kudo, K. Omori, H. Kato, A novel aqueous process for preparation of crystal form-controlled and highly crystalline BiVO4 powder from layered vanadates at room temperature and its photocatalytic and photophysical properties, Journal of the American Chemical Society. 121 (1999) 11459–11467. https://doi.org/10.1021/JA992541Y.

[45] A.R. Lim, S.H. Choh, Min Su Jang, Prominent ferroelastic domain walls in BiVO4 crystal, Journal of Physics: Condensed Matter. 7 (1995) 7309–7323. https://doi.org/10.1088/0953-8984/7/37/005.

[46] A.K. Bhattacharya, K.K. Mallick, A. Hartridge, Phase transition in BiVO4, Materials Letters. 30 (1997) 7–13. https://doi.org/10.1016/S0167-577X(96)00162-0.

[47] Y.H. Ng, A. Iwase, A. Kudo, R. Amal, Reducing graphene oxide on a visible-light BiVO4 photocatalyst for an enhanced photoelectrochemical water splitting, Journal of Physical Chemistry Letters. 1 (2010) 2607–2612. https://doi.org/10.1021/JZ100978U.

[48] H.L. Tan, R. Amal, Y.H. Ng, Alternative strategies in improving the photocatalytic and photoelectrochemical activities of visible light-driven BiVO4: A review, Journal of Materials Chemistry A. 5 (2017) 16498–16521. https://doi.org/10.1039/c7ta04441k.

[49] P. Luan, J. Zhang, Stepping towards Solar Water Splitting: Recent Progress in Bismuth Vanadate Photoanodes, ChemElectroChem. 6 (2019) 3227–3243.

https://doi.org/10.1002/CELC.201900398.

[50] J.K. Cooper, S. Gul, F.M. Toma, L. Chen, Y.S. Liu, J. Guo, J.W. Ager, J. Yano, I.D. Sharp, Indirect bandgap and optical properties of monoclinic bismuth vanadate, Journal of Physical Chemistry C. 119 (2015) 2969–2974. https://doi.org/10.1021/JP512169W.

[51] Z. Zhao, Z. Li, Z. Zou, Electronic structure and optical properties of monoclinic clinobisvanite BiVO4, Physical Chemistry Chemical Physics. 13 (2011) 4746–4753. https://doi.org/10.1039/c0cp01871f.

[52] Y. Liu, B. Huang, Y. Dai, X. Zhang, X. Qin, M. Jiang, M.-H. Whangbo, Selective ethanol formation from photocatalytic reduction of carbon dioxide in water with BiVO4 photocatalyst, Catalysis Communications. 11 (2009) 210–213. https://doi.org/10.1016/j.catcom.2009.10.010.

[53] K. Tolod, S. Hernández, N.R.- Catalysts, undefined 2017, Recent advances in the BiVO4 photocatalyst for sun-driven water oxidation: top-performing photoanodes and scale-up challenges, Mdpi.Com. (n.d.). https://www.mdpi.com/173388 (accessed December 10, 2021).

[54] S.J. Hong, S. Lee, J.S. Jang, J.S. Lee, Heterojunction BiVO4/WO3 electrodes for enhanced photoactivity of water oxidation, Energy and Environmental Science. 4 (2011) 1781–1787. https://doi.org/10.1039/c0ee00743a.

[55] W. Yao, H. Iwai, J. Ye, Effects of molybdenum substitution on the photocatalytic behavior of BiVO4, Journal of the Chemical Society. Dalton Transactions. (2008) 1426–1430. https://doi.org/10.1039/b713338c.

[56] F.F. Abdi, L. Han, A.H.M. Smets, M. Zeman, B. Dam, R. Van De Krol, Efficient solar water splitting by enhanced charge separation in a bismuth vanadate-silicon tandem photoelectrode, Nature.Com. (2013). https://doi.org/10.1038/ncomms3195.

[57] M.R. Hoffmann, S.T. Martin, W. Choi, D.W. Bahnemann, Environmental Applications of Semiconductor Photocatalysis, Chemical Reviews. 95 (1995) 69–96. https://doi.org/10.1021/CR00033A004.

[58] W.J. Jo, J.-W. Jang, K. Kong, H.J. Kang, J.Y. Kim, H. Jun, K.P.S. Parmar, J.S. Lee, Phosphate Doping into Monoclinic BiVO4 for Enhanced Photoelectrochemical Water Oxidation Activity, Angewandte Chemie. 124 (2012) 3201–3205. https://doi.org/10.1002/ANGE.201108276.

[59] Z. Zhao, H. Dai, J. Deng, Y. Liu, C.T. Au, Effect of sulfur doping on the photocatalytic performance of BiVO4 under visible light illumination, Cuihua Xuebao/Chinese Journal of Catalysis. 34 (2013) 1617–1626. https://doi.org/10.1016/S1872-2067(12)60632-9.

[60] H. Jiang, H. Dai, J. Deng, Y. Liu, L. Zhang, K. Ji, Porous F-doped BiVO4: Synthesis and enhanced photocatalytic performance for the degradation of phenol under visible-light illumination, Solid State Sciences. 17 (2013) 21–27. https://doi.org/10.1016/j.solidstatesciences.2012.12.009.

[61] S. Usai, S. Obregón, A.I. Becerro, G. Colón, Monoclinic-tetragonal heterostructured BiVO4 by yttrium doping with improved photocatalytic activity, Journal of Physical

Chemistry C. 117 (2013) 24479–24484. https://doi.org/10.1021/JP409170Y.

[62] C. Karunakaran, S. Kalaivani, P. Vinayagamoorthy, S. Dash, Optical, electrical and visible light-photocatalytic properties of yttrium-substituted BiVO4 nanoparticles, Materials Science and Engineering B: Solid-State Materials for Advanced Technology. 187 (2014) 53–60. https://doi.org/10.1016/j.mseb.2014.05.001.

[63] A. Zhang, J. Zhang, Effects of europium doping on the photocatalytic behavior of BiVO4, Journal of Hazardous Materials. 173 (2010) 265–272. https://doi.org/10.1016/j.jhazmat.2009.08.079.

[64] Z. Huang, L. Pan, J. Zou, X. Zhang, L.W.- Nanoscale, undefined 2014, Nanostructured bismuth vanadate-based materials for solar-energy-driven water oxidation: a review on recent progress, Pubs.Rsc.Org. (n.d.). https://pubs.rsc.org/en/content/articlehtml/2015/nr/c4nr05245e (accessed December 21, 2022).

[65] S.M. Thalluri, S. Hernández, S. Bensaid, G. Saracco, N. Russo, Green-synthesized W- and Mo-doped BiVO4 oriented along the {040} facet with enhanced activity for the sun-driven water oxidation, Applied Catalysis B: Environmental. 180 (2016) 630–636. https://doi.org/10.1016/j.apcatb.2015.07.029.

[66] Z. Zhao, W. Luo, Z. Li, Z. Zou, Density functional theory study of doping effects in monoclinic clinobisvanite BiVO4, Physics Letters, Section A: General, Atomic and Solid State Physics. 374 (2010) 4919–4927. https://doi.org/10.1016/j.physleta.2010.10.014.

[67] K. Ding, B. Chen, Z. Fang, Y. Zhang, Z. Chen, Why the photocatalytic activity of Mo-doped BiVO4 is enhanced: A comprehensive density functional study, Physical Chemistry Chemical Physics. 16 (2014) 13465–13476. https://doi.org/10.1039/c4cp01350f.

[68] S.P. Berglund, A.J.E. Rettie, S. Hoang, C.B. Mullins, Incorporation of Mo and W into nanostructured BiVO 4 films for efficient photoelectrochemical water oxidation, Physical Chemistry Chemical Physics. 14 (2012) 7065–7075. https://doi.org/10.1039/c2cp40807d.

[69] R.P. Antony, P.S. Bassi, F.F. Abdi, S.Y. Chiam, Y. Ren, J. Barber, J.S.C. Loo, L.H. Wong, Electrospun Mo-BiVO4 for Efficient Photoelectrochemical Water Oxidation: Direct Evidence of Improved Hole Diffusion Length and Charge separation, Electrochimica Acta. 211 (2016) 173–182. https://doi.org/10.1016/j.electacta.2016.06.008.

[70] M. Wang, Q. Liu, Y. Che, L. Zhang, D.Z.-J. of A. and, undefined 2013, Characterization and photocatalytic properties of N-doped BiVO4 synthesized via a sol–gel method, Elsevier. (n.d.). https://www.sciencedirect.com/science/article/pii/S092583881201571X (accessed September 26, 2022).

[71] T. oJ ing, Y. Liu, B. Huang, Y. Dai, X. Zhang, X. Qin, andMyung-H. Whangbo, Enhancing the Efficiency of Water Oxidation by Boron-Doped BiVO4 under Visible Light: Hole Trapping by BO4 Tetrahedra, Wiley Online Library. 80 (2015) 1113–1118. https://doi.org/10.1002/cplu.201500110.

[72] V. Merupo, Synthesis and characterization of metal doped BiVO4 nanostructured materials for photocatalytic applications, (2016). https://tel.archives-ouvertes.fr/tel-

01346611/ (accessed December 27, 2022).

[73] K. Watanabe, A. Iwase, S. Nozawa, S.I. Adachi, A. Kudo, Effects of Coapplication of Rh-Doping and Ag-Substitution on the Band Structure of Li2TiO3 and the Photocatalytic Property, ACS Sustainable Chemistry and Engineering. 7 (2019) 9881–9887. https://doi.org/10.1021/ACSSUSCHEMENG.9B00513/ASSET/IMAGES/LARGE/SC-2019-00513V_0006.JPEG.

[74] G.S.-P.B.C. Matter, undefined 2021, Site selective Ag doping in Cu3N and its consequences on structural and electronic properties: A DFT study, Elsevier. (n.d.). https://www.sciencedirect.com/science/article/pii/S0921452621004142 (accessed December 21, 2022).

[75] K. Ding, B. Chen, Z. Fang, Y. Zhang, Z. Chen, Why the photocatalytic activity of Mo-doped BiVO4 is enhanced: A comprehensive density functional study, Physical Chemistry Chemical Physics. 16 (2014) 13465–13476. https://doi.org/10.1039/c4cp01350f.

[76] S.J.A. Moniz, S.A. Shevlin, D.J. Martin, Z.-X. Guo, J. Tang, Visible-light driven heterojunction photocatalysts for water splitting – a critical review, Energy & Environmental Science. 8 (2015) 731–759. https://doi.org/10.1039/C4EE03271C.

[77] F. Stelo, N. Kublik, S. Ullah, H. Wender, Recent advances in Bi2MoO6 based Z-scheme heterojunctions for photocatalytic degradation of pollutants, Journal of Alloys and Compounds. 829 (2020) 154591. https://doi.org/10.1016/j.jallcom.2020.154591.

[78] J. Low, J. Yu, M. Jaroniec, S. Wageh, A.A. Al-Ghamdi J X Low, J.G. Yu, S. Wageh, A.A. Al-Ghamdi, M. Jaroniec, Heterojunction photocatalysts, Wiley Online Library. 29 (2017). https://doi.org/10.1002/adma.201601694.

[79] H. Wang, L. Zhang, Z. Chen, J. Hu, S. Li, Z. Wang, J. Liu, X. Wang, Semiconductor heterojunction photocatalysts: design, construction, and photocatalytic performances, Chemical Society Reviews. 43 (2014) 5234. https://doi.org/10.1039/C4CS00126E.

[80] R. Yanagi, T. Zhao, D. Solanki, Z. Pan, S. Hu, Charge Separation in Photocatalysts: Mechanisms, Physical Parameters, and Design Principles, ACS Energy Letters. 7 (2022) 432–452. https://doi.org/10.1021/ACSENERGYLETT.1C02516.

[81] T. Zhao, R. Yanagi, Y. Xu, Y. He, Y. Song, M. Yang, S. Hu, A coating strategy to achieve effective local charge separation for photocatalytic coevolution, Proceedings of the National Academy of Sciences of the United States of America. 118 (2021). https://doi.org/10.1073/PNAS.2023552118.

[82] H. Xu, C. Wu, H. Li, J. Chu, G. Sun, Y. Xu, Y. Yan, Synthesis, characterization and photocatalytic activities of rare earth-loaded BiVO 4 catalysts, Applied Surface Science. 256 (2009) 597–602. https://doi.org/10.1016/j.apsusc.2009.05.102.

[83] E.A. Mohamed, Z.N. Zahran, Y. Naruta, Simple preparation of highly active water splitting FTO/BiVO4 photoanode modified with tri-layer water oxidation catalysts, Journal of Materials Chemistry A. 5 (2017) 6825–6831. https://doi.org/10.1039/c7ta00156h.

[84] S. Wang, T. He, J. Yun, Y. Hu, M. Xiao, A. Du, L. Wang, New Iron-Cobalt Oxide Catalysts Promoting BiVO 4 Films for Photoelectrochemical Water Splitting, Advanced Functional Materials. 28 (2018) 1802685. https://doi.org/10.1002/adfm.201802685.

[85] E.C. Kohlrausch, H.A. Centurion, R.W. Lodge, X. Luo, T. Slater, M.J.L. Santos, S. Ling, V.R. Mastelaro, M.J. Cliffe, R.V. Goncalves, J. Alves Fernandes, A high-throughput, solvent free method for dispersing metal atoms directly onto supports, Journal of Materials Chemistry A. 9 (2021) 26676–26679. https://doi.org/10.1039/d1ta08372d.

[86] Y. Ishida, R.D. Corpuz, T. Yonezawa, Matrix Sputtering Method: A Novel Physical Approach for Photoluminescent Noble Metal Nanoclusters, Accounts of Chemical Research. 50 (2017) 2986–2995. https://doi.org/10.1021/acs.accounts.7b00470.

[87] R. V. Gonçalves, H. Wender, P. Migowski, A.F. Feil, D. Eberhardt, J. Boita, S. Khan, G. Machado, J. Dupont, S.R. Teixeira, Photochemical Hydrogen Production of Ta 2 O 5 Nanotubes Decorated with NiO Nanoparticles by Modified Sputtering Deposition , The Journal of Physical Chemistry C. 121 (2017) 5855–5863. https://doi.org/10.1021/ACS.JPCC.6B10540.

[88] Q. Wu, S. Bao, B. Tian, Y. Xiao, J.Z.-C. Communications, undefined 2016, Double-diffusion-based synthesis of BiVO 4 mesoporous single crystals with enhanced photocatalytic activity for oxygen evolution, Pubs.Rsc.Org. (n.d.). https://pubs.rsc.org/en/content/articlehtml/2016/cc/c6cc02737g (accessed January 25, 2023).

[89] Y.K. Kho, W.Y. Teoh, A. Iwase, L. Mädler, A. Kudo, R. Amal, Flame preparation of visible-light-responsive BiVO 4 oxygen evolution photocatalysts with subsequent activation via aqueous route, ACS Applied Materials and Interfaces. 3 (2011) 1997–2004. https://doi.org/10.1021/AM200247Y.

[90] Z. Jiang, Y. Liu, T. Jing, B. Huang, X. Zhang, X. Qin, Y. Dai, M.H. Whangbo, Enhancing the Photocatalytic Activity of BiVO4 for Oxygen Evolution by Ce Doping: Ce3+ Ions as Hole Traps, Journal of Physical Chemistry C. 120 (2016) 2058–2063. https://doi.org/10.1021/ACS.JPCC.5B10856.

[91] H.L. Tan, R. Amal, Y.H. Ng, Exploring the Different Roles of Particle Size in Photoelectrochemical and Photocatalytic Water Oxidation on BiVO4, ACS Applied Materials and Interfaces. 8 (2016) 28607–28614. https://doi.org/10.1021/ACSAMI.6B09076.

[92] P. Stathi, M. Solakidou, Y. Deligiannakis, Lattice Defects Engineering in W-, Zr-doped BiVO4 by Flame Spray Pyrolysis: Enhancing Photocatalytic O2 Evolution, Nanomaterials. 11 (2021) 501. https://doi.org/10.3390/nano11020501.

[93] S. Ikeda, T. Kawaguchi, Y. Higuchi, N. Kawasaki, T. Harada, M. Remeika, M.M. Islam, T. Sakurai, Effects of zirconium doping into a monoclinic scheelite BiVO4 crystal on its structural, photocatalytic, and photoelectrochemical properties, Frontiers in Chemistry. 6 (2018). https://doi.org/10.3389/FCHEM.2018.00266/FULL.

[94] B. He, Z. Li, D. Zhao, H. Liu, Y. Zhong, J. Ning, Z. Zhang, Y. Wang, Y. Hu, Fabrication of porous cu-doped bivo4 nanotubes as efficient oxygen-evolving photocatalysts, ACS

Applied Nano Materials. 1 (2018) 2589–2599. https://doi.org/10.1021/ACSANM.8B00281.

[95] Y. Hermans, C. Olivier, H. Junge, A. Klein, W. Jaegermann, T. Toupance, Sunlight Selective Photodeposition of CoOx(OH)yand NiOx(OH)yon Truncated Bipyramidal BiVO4for Highly Efficient Photocatalysis, ACS Applied Materials and Interfaces. 12 (2020) 53910–53920. https://doi.org/10.1021/ACSAMI.0C14624.

[96] Z. Xie, H. Tan, H. Wu, R. Amal, J. Scott, Y.N.-M.T. Energy, undefined 2022, Facet-dependent spatial charge separation with rational cocatalyst deposition on BiVO4, Elsevier. (n.d.). https://www.sciencedirect.com/science/article/pii/S2468606922000442 (accessed January 25, 2023).

[97] Y. Zou, M. Lu, Z. Jiang, L. Xu, C. Liu, L. Zhang, Y. Chen, Hydrothermal synthesis of Zn-doped BiVO4 with mixed crystal phase for enhanced photocatalytic activity, Optical Materials. 119 (2021) 111398. https://doi.org/10.1016/j.optmat.2021.111398.

[98] N. Khan, R. Rio, N. Wolff, H. Ullah, G.J. Chacó, W.S. Rosa, J. Dupont, R.V. Gonçalves, S. Khan, Ionic liquid based dopant-free band edge shift in BiVO4 particles for photocatalysis under simulated sunlight irradiation, Pubs.Rsc.Org. (2022). https://doi.org/10.1039/d2ma00259k.

[99] A. Hankin, F.E. Bedoya-Lora, J.C. Alexander, A. Regoutz, G.H. Kelsall, Flat band potential determination: avoiding the pitfalls, Journal of Materials Chemistry A. 7 (2019) 26162–26176. https://doi.org/10.1039/C9TA09569A.

[100] F. Cardon, W.P. Gomes, On the determination of the flat-band potential of a semiconductor in contact with a metal or an electrolyte from the Mott-Schottky plot, Journal of Physics D: Applied Physics. 11 (1978) L63. https://doi.org/10.1088/0022-3727/11/4/003.

[101] M. Valant, D. Suvorov, Chemical Compatibility between Silver Electrodes and Low-Firing Binary-Oxide Compounds: Conceptual Study, Journal of the American Ceramic Society. 83 (2000) 2721–2729. https://doi.org/10.1111/J.1151-2916.2000.TB01623.X.

[102] A. Manohar, V. Vijayakanth, R. Hong, Solvothermal reflux synthesis of NiFe2O4 nanocrystals dielectric and magnetic hyperthermia properties, Journal of Materials Science: Materials in Electronics. 31 (2020) 799–806. https://doi.org/10.1007/S10854-019-02588-Z/FIGURES/10.

[103] M.V. Nikolic, M.D. Lukovic, N.J. Labus, Influence of humidity on complex impedance and dielectric properties of iron manganite (FeMnO3), Journal of Materials Science: Materials in Electronics. 30 (2019) 12399–12405. https://doi.org/10.1007/S10854-019-01598-1/FIGURES/9.

[104] R.L. Anderson, Experiments on Ge-GaAs heterojunctions, Solid-State Electronics. 5 (1962) 341–351. https://doi.org/10.1016/0038-1101(62)90115-6.

[105] W.S. Rosa, L.G. Rabelo, L.G. Tiveron Zampaulo, R. V. Gonçalves, Ternary Oxide CuWO4/BiVO4/FeCoOxFilms for Photoelectrochemical Water Oxidation: Insights into the Electronic Structure and Interfacial Band Alignment, ACS Applied Materials and

Interfaces. (2021). https://doi.org/10.1021/ACSAMI.1C21001/SUPPL_FILE/AM1C21001_SI_001.PDF.

[106] C.R. i Bellés, S. Selim, N.M. Harrison, E.A. Ahmad, A. Kafizas, Beyond band bending in the WO3/BiVO4 heterojunction: insight from DFT and experiment, Sustainable Energy & Fuels. 3 (2018) 264–271. https://doi.org/10.1039/C8SE00420J.

[107] S.M. Sze, K.K. Ng, Physics of Semiconductor Devices, Physics of Semiconductor Devices. (2006). https://doi.org/10.1002/0470068329.

[108] R. Badam, Y. Asai, A. Gupta, al -, S. Beck, A. Hampel, P. Giannozzi, S. Baroni, N. Bonini, M. Calandra, R. Car, C. Cavazzoni, D. Ceresoli, G.L. Chiarotti, M. Cococcioni, I. Dabo, A. Dal Corso, S. de Gironcoli, S. Fabris, G. Fratesi, R. Gebauer, U. Gerstmann, C. Gougoussis, A. Kokalj, M. Lazzeri, L. Martin-Samos, N. Marzari, F. Mauri, R. Mazzarello, S. Paolini, A. Pasquarello, L. Paulatto, C. Sbraccia, S. Scandolo, G. Sclauzero, A.P. Seitsonen, A. Smogunov, P. Umari, R.M. Wentzcovitch, QUANTUM ESPRESSO: a modular and open-source software project for quantum simulations of materials, Iopscience.Iop.Org. 21 (2009) 395502. https://doi.org/10.1088/0953-8984/21/39/395502.

[109] A. Sleight, H. Chen, A. Ferretti, D.C.-M.R. Bulletin, undefined 1979, Crystal growth and structure of BiVO4, Elsevier. (n.d.). https://www.sciencedirect.com/science/article/abs/pii/0025540872902279 (accessed November 9, 2022).

[110] J. Shi, W. Zhang, Q.G.-T.J. of P.C. C, undefined 2022, Ab Initio Calculation of Surface-Controlled Photocatalysis in Multiple-Phase BiVO4, ACS Publications. (n.d.). https://pubs.acs.org/doi/abs/10.1021/acs.jpcc.2c01936 (accessed November 9, 2022).

[111] I. Laraib, M.A. Carneiro, A. Janotti, Effects of Doping on the Crystal Structure of BiVO4, Journal of Physical Chemistry C. 123 (2019) 26752–26757. https://doi.org/10.1021/ACS.JPCC.9B05858.

[112] A.H. Larsen, M. Vanin, J.J. Mortensen, K.S. Thygesen, K.W. Jacobsen, Localized atomic basis set in the projector augmented wave method, Physical Review B - Condensed Matter and Materials Physics. 80 (2009). https://doi.org/10.1103/PHYSREVB.80.195112.

[113] S. Li, M. Zhou, M. Li, G. Lu, X. Wang, F. Zheng, P. Zhang, Adsorption of 3 d, 4 d, and 5 d transition-metal atoms on single-layer boron nitride, Journal of Applied Physics. 123 (2018). https://doi.org/10.1063/1.5012549.

[114] J.B. Liu, H. Wang, S. Wang, H. Yan, Hydrothermal preparation of BiVO4 powders, Materials Science and Engineering B: Solid-State Materials for Advanced Technology. 104 (2003) 36–39. https://doi.org/10.1016/S0921-5107(03)00264-2.

[115] S.M. Thalluri, C. Martinez Suarez, S. Hernández, S. Bensaid, G. Saracco, N. Russo, Elucidation of important parameters of BiVO4 responsible for photo-catalytic O2 evolution and insights about the rate of the catalytic process, Chemical Engineering Journal. 245 (2014) 124–132. https://doi.org/10.1016/j.cej.2014.02.017.

[116] S.M. Thalluri, M. Hussain, G. Saracco, J. Barber, N. Russo, Green-Synthesized BiVO4

Oriented along {040} Facets for Visible-Light-Driven Ethylene Degradation, ACS Publications. 53 (2014) 2640–2646. https://doi.org/10.1021/ie403999g.

[117] S. Thalluri, C. Suarez, … S.H.-C.E., U. 2014, Elucidation of important parameters of BiVO4 responsible for photo-catalytic O2 evolution and insights about the rate of the catalytic process, Elsevier. (n.d.). https://www.sciencedirect.com/science/article/pii/S1385894714001545?casa_token=UJZgJI_MuXwAAAAA:r8iJvbcYmMgU32fzJ6ELcdeo_W7cUsp7_cC_sn2h8euqUxbx4PQELXQvl5CAKh2OQqT2QRkIHXbV (accessed December 23, 2021).

[118] X. Wan, F. Niu, J. Su, L. Guo, Enhanced photoelectrochemical water oxidation of bismuth vanadate via a combined strategy of W doping and surface RGO modification, Physical Chemistry Chemical Physics. 18 (2016) 31803–31810. https://doi.org/10.1039/C6CP06233D.

[119] J.I. Langford, A.J.C. Wilson, Scherrer after sixty years: A survey and some new results in the determination of crystallite size, Journal of Applied Crystallography. 11 (1978) 102–113. https://doi.org/10.1107/S0021889878012844.

[120] A. Sami, E. David, M. Fréchette, Procedure for evaluating the crystallinity from X-ray diffraction scans of high and low density polyethylene/SiO2 composites, Annual Report - Conference on Electrical Insulation and Dielectric Phenomena, CEIDP. (2010). https://doi.org/10.1109/CEIDP.2010.5724069.

[121] G.A.S. Alves, H.A. Centurion, J.R. Sambrano, M.M. Ferrer, R. V Gonç, Band Gap Narrowing of Bi-Doped NaTaO3 for Photocatalytic Hydrogen Evolution under Simulated Sunlight: A Pseudocubic Phase Induced by Doping, ACS Publications. 4 (2021) 671–679. https://doi.org/10.1021/acsaem.0c02547.

[122] R. Li, F. Zhang, D. Wang, J. Yang, M. Li, J. Zhu, X. Zhou, H. Han, C. Li, Spatial separation of photogenerated electrons and holes among {010} and {110} crystal facets of BiVO4, Nature Communications. 4 (2013) 1432. https://doi.org/10.1038/ncomms2401.

[123] S.M. Thalluri, S. Hernández, S. Bensaid, G. Saracco, N. Russo, Green-synthesized W- and Mo-doped BiVO4 oriented along the {0 4 0} facet with enhanced activity for the sun-driven water oxidation, Applied Catalysis B: Environmental. 180 (2016) 630–636. https://doi.org/10.1016/j.apcatb.2015.07.029.

[124] Y. Hou, H. Yuan, H. Chen, J. Feng, Y. Ding, L. Li, Preparation of La3+/Zn2+-doped BiVO4 nanoparticles and its enhanced visible photocatalytic activity, Applied Physics A: Materials Science and Processing. 123 (2017). https://doi.org/10.1007/S00339-017-1228-3.

[125] M.A. Melo, H.A. Centurion, G. Machado, F.L. Souza, R. V. Gonçalves, Binary Transition Metal NiFeO x and CoFeO x Cocatalysts Boost the Photodriven Water Oxidation over Fe 2 TiO 5 Nanoparticles , ChemNanoMat. (2022). https://doi.org/10.1002/CNMA.202100510.

[126] J. Su, X.X. Zou, G.D. Li, X. Wei, C. Yan, Y.N. Wang, J. Zhao, L.J. Zhou, J.S. Chen, Macroporous V2O5-BiVO4 composites: Effect of heterojunction on the behavior of photogenerated charges, Journal of Physical Chemistry C. 115 (2011) 8064–8071.

https://doi.org/10.1021/JP200274K.

[127] A.P. Singh, N. Kodan, A. Dey, S. Krishnamurthy, B.R. Mehta, Improvement in the structural, optical, electronic and photoelectrochemical properties of hydrogen treated bismuth vanadate thin films, International Journal of Hydrogen Energy. 40 (2015) 4311–4319. https://doi.org/10.1016/j.ijhydene.2015.01.085.

[128] S. Ju, J. Jun, S. Son, J. Park, H. Lim, W. Kim, D. Chae, H. Lee, Structured BiVO4Photoanode Fabricated via Sputtering for Large Areas and Enhanced Photoelectrochemical Performance, ACS Sustainable Chemistry and Engineering. 8 (2020) 17923–17932. https://doi.org/10.1021/ACSSUSCHEMENG.0C05225.

[129] Y. Guo, Y. Wu, Z. Wang, D. Dai, X. Liu, Q. Zhang, Z. Wang, Y. Liu, Z. Zheng, H. Cheng, B. Huang, Y. Dai, P. Wang, Multi-strategy preparation of BiVO4 photoanode with abundant oxygen vacancies for efficient water oxidation, Applied Surface Science. 614 (2023) 156164. https://doi.org/10.1016/j.apsusc.2022.156164.

[130] Y. Yang, Y. Zhao, W. Fan, H. Shen, W. Shi, A simple flame strategy for constructing W-doped BiVO4 photoanodes with enhanced photoelectrochemical water splitting, International Journal of Energy Research. 44 (2020) 10821–10831. https://doi.org/10.1002/ER.5736.

[131] L. Zhao, J. Wei, Y. Li, C. Han, L. Pan, Z. Liu, Photoelectrochemical performance of W-doped BiVO4 photoanode, Journal of Materials Science: Materials in Electronics. 30 (2019) 21425–21434. https://doi.org/10.1007/s10854-019-02521-4.

[132] M. Zhong, T. Hisatomi, Y. Kuang, J. Zhao, M. Liu, A. Iwase, Q. Jia, H. Nishiyama, T. Minegishi, M. Nakabayashi, N. Shibata, R. Niishiro, C. Katayama, H. Shibano, M. Katayama, A. Kudo, T. Yamada, K. Domen, Surface modification of CoOx loaded BiVO4 photoanodes with ultrathin p-type NiO layers for improved solar water oxidation, Journal of the American Chemical Society. 137 (2015) 5053–5060. https://doi.org/10.1021/JACS.5B00256.

[133] Y. Hermans, A. Klein, K. Ellmer, R. Van De Krol, T. Toupance, W. Jaegermann, Energy-Band Alignment of BiVO4 from Photoelectron Spectroscopy of Solid-State Interfaces, Journal of Physical Chemistry C. 122 (2018) 20861–20870. https://doi.org/10.1021/ACS.JPCC.8B06241.

[134] J. Zhang, S. Han, M. Cui, X. Xu, W. Li, H. Xu, C. Jin, M. Gu, L. Chen, K.H.L. Zhang, Fabrication and Interfacial Electronic Structure of Wide Bandgap NiO and Ga2O3p-n Heterojunction, ACS Applied Electronic Materials. 2 (2020) 456–463. https://doi.org/10.1021/ACSAELM.9B00704.

[135] H. Wang, Q. Yao, C. Wang, Z. Ma, Q. Sun, B. Fan, C. Jin, Y. Chen, Hydrothermal synthesis of nanooctahedra MnFe2O4 onto the wood surface with soft magnetism, fire resistance and electromagnetic wave absorption, Nanomaterials. 7 (2017). https://doi.org/10.3390/nano7060118.

[136] H. Ali-Löytty, M.W. Louie, M.R. Singh, L. Li, H.G. Sanchez Casalongue, H. Ogasawara, E.J. Crumlin, Z. Liu, A.T. Bell, A. Nilsson, D. Friebel, Ambient-Pressure XPS Study of a Ni-Fe Electrocatalyst for the Oxygen Evolution Reaction, Journal of Physical Chemistry

C. 120 (2016) 2247–2253. https://doi.org/10.1021/ACS.JPCC.5B10931.

[137] H. Du, Z. Han, X. Wu, C. Li, Y. Gao, S. Yang, L. Song, J. Dong, X. Pan, Insight into the promoting role of er modification on so2 resistance for nh3-scr at low temperature over femn/tio2 catalysts, Catalysts. 11 (2021). https://doi.org/10.3390/CATAL11050618.

[138] M.A. Melo, H.A. Centurion, T.T.A. Lucas, D.N.F. Muche, F.L. Souza, R. V. Gonçalves, Pseudobrookite Fe2TiO5Nanoparticles Loaded with Earth-Abundant Nanosized NiO and Co3O4Cocatalysts for Photocatalytic O2Evolution via Solar Water Splitting, ACS Applied Nano Materials. 3 (2020) 9303–9317. https://doi.org/10.1021/ACSANM.0C01957.

[139] S. Saxena, A. Verma, N.K. Biswas, S.A. Khan, V.R. Satsangi, R. Shrivastav, S. Dass, Zr–W Co-doping in BiVO4 – Synergistic effect in photoelectrochemical water splitting, Materials Chemistry and Physics. 267 (2021) 124675. https://doi.org/10.1016/j.matchemphys.2021.124675.

[140] K.P.S. Parmar, H.J. Kang, A. Bist, P. Dua, J.S. Jang, J.S. Lee, Photocatalytic and photoelectrochemical water oxidation over metal-doped monoclinic BiVO4 photoanodes, ChemSusChem. 5 (2012) 1926–1934. https://doi.org/10.1002/CSSC.201200254.

[141] B. Wang, P. Li, C. Du, Y. Wang, D. Gao, S. Li, L. Zhang, F. Wen, Synergetic effect of dual co-catalysts on the activity of BiVO 4 for photocatalytic carbamazepine degradation, RSC Advances. 9 (2019) 41977–41983. https://doi.org/10.1039/C9RA07152K.

[142] L. Gao, F. Li, H. Hu, X. Long, N. Xu, Y. Hu, S. Wei, C. Wang, J. Ma, J. Jin, Dual Modification of a BiVO4 Photoanode for Enhanced Photoelectrochemical Performance, ChemSusChem. 11 (2018) 2502–2509. https://doi.org/10.1002/CSSC.201800999.

[143] H. Li, H. Yu, X. Quan, S. Chen, Y. Zhang, Uncovering the Key Role of the Fermi Level of the Electron Mediator in a Z-Scheme Photocatalyst by Detecting the Charge Transfer Process of WO3-metal-gC3N4 (Metal = Cu, Ag, Au), ACS Applied Materials and Interfaces. 8 (2016) 2111–2119. https://doi.org/10.1021/ACSAMI.5B10613/SUPPL_FILE/AM5B10613_SI_001.PDF.

[144] Y. Matsumoto, Energy Positions of Oxide Semiconductors and Photocatalysis with Iron Complex Oxides, Journal of Solid State Chemistry. 126 (1996) 227–234. https://doi.org/10.1006/JSSC.1996.0333.

[145] S. Wang, T. He, J.H. Yun, Y. Hu, M. Xiao, A. Du, L. Wang, New Iron-Cobalt Oxide Catalysts Promoting BiVO4 Films for Photoelectrochemical Water Splitting, Advanced Functional Materials. 28 (2018). https://doi.org/10.1002/ADFM.201802685.

[146] Y. Gong, Z. Yang, L. Lari, I. Azaceta, V.K. Lazarov, J. Zhang, X. Xu, Q. Cheng, K.H.L. Zhang, Optimizing the Electronic Structure of In2O3through Mg Doping for NiO/In2O3p-n Heterojunction Diodes, ACS Applied Materials and Interfaces. 12 (2020) 53446–53453. https://doi.org/10.1021/ACSAMI.0C14348/ASSET/IMAGES/MEDIUM/AM0C14348_M005.GIF.

[147] A. Iqbal, A. Kafizas, C. Sotelo-Vazquez, R. Wilson, M. Ling, A. Taylor, C. Blackman, K. Bevan, I. Parkin, R. Quesada-Cabrera, Charge Transport Phenomena in Heterojunction

Photocatalysts: The WO3/TiO2System as an Archetypical Model, ACS Applied Materials and Interfaces. 13 (2021) 9781–9793. https://doi.org/10.1021/ACSAMI.0C19692/SUPPL_FILE/AM0C19692_SI_001.PDF.

[148] P. Cendula, S. David Tilley, S. Gimenez, J. Bisquert, M. Schmid, M. Grätzel, J.O. Schumacher, Calculation of the energy band diagram of a photoelectrochemical water splitting cell, Journal of Physical Chemistry C. 118 (2014) 29599–29607. https://doi.org/10.1021/JP509719D/SUPPL_FILE/JP509719D_SI_001.PDF.

[149] L.M. Peter, Photoelectrochemical Water Splitting. A Status Assessment, Electroanalysis. 27 (2015) 864–871. https://doi.org/10.1002/ELAN.201400587.

[150] G. V. Govindaraju, J.M. Morbec, G.A. Galli, K.S. Choi, Experimental and computational investigation of lanthanide ion doping on BiVO4 Photoanodes for Solar Water Splitting, Journal of Physical Chemistry C. 122 (2018) 19416–19424. https://doi.org/10.1021/ACS.JPCC.8B05503.

[151] Q. Pan, K. Yang, G. Wang, D. Li, J. Sun, B. Yang, Z. Zou, W. Hu, K. Wen, H. Yang, BiVO4 nanocrystals with controllable oxygen vacancies induced by Zn-doping coupled with graphene quantum dots for enhanced photoelectrochemical water splitting, Chemical Engineering Journal. 372 (2019) 399–407. https://doi.org/10.1016/j.cej.2019.04.161.

[152] Y.K. Kho, W.Y. Teoh, A. Iwase, L. Mädler, A. Kudo, R. Amal, Flame preparation of visible-light-responsive BiVO 4 oxygen evolution photocatalysts with subsequent activation via aqueous route, ACS Applied Materials and Interfaces. 3 (2011) 1997–2004. https://doi.org/10.1021/am200247y.

[153] S.H. Chen, Y.S. Jiang, H.Y. Lin, Easy Synthesis of BiVO4 for Photocatalytic Overall Water Splitting, ACS Omega. 5 (2020) 8927–8933. https://doi.org/10.1021/ACSOMEGA.0C00699.

[154] S. Wang, P. Chen, J.-H. Yun, Y. Hu, L. Wang, An Electrochemically Treated BiVO 4 Photoanode for Efficient Photoelectrochemical Water Splitting , Angewandte Chemie. 129 (2017) 8620–8624. https://doi.org/10.1002/ANGE.201703491.

[155] N. Wolff, H. Ullah, G.J. Chacon, W. Santa Rosa, J. Dupont, R.V. Goncalves, S. Khan, N. Khan, R.N. Wolff, H. Ullah, G.J. Chacón, W.S. Rosa, J. Dupont, R.V. Gonçalves, S. Khan, Ionic liquid based dopant-free band edge shift in BiVO4 particles for photocatalysis under simulated sunlight irradiation, Pubs.Rsc.Org. (2022). https://doi.org/10.1039/D2MA00259K.

[156] X. Shi, S. Chen, M. Luo, B. Huang, G. Zhang, R.C.-N. Research, undefined 2020, Zn-doping enhances the photoluminescence and stability of PbS quantum dots for in vivo high-resolution imaging in the NIR-II window, Springer. 13 (2020) 2239–2245. https://doi.org/10.1007/s12274-020-2843-4.

[157] P. Karuppasamy, N. Ramzan Nilofar Nisha, A. Pugazhendhi, S. Kandasamy, S. Pitchaimuthu, An investigation of transition metal doped TiO2photocatalysts for the enhanced photocatalytic decoloration of methylene blue dye under visible light irradiation, Journal of Environmental Chemical Engineering. 9 (2021). https://doi.org/10.1016/j.jece.2021.105254.

[158] M. Wang, Y. Che, C. Niu, M. Dang, D. Dong, Effective visible light-active boron and europium co-doped BiVO4 synthesized by sol-gel method for photodegradion of methyl orange., Journal of Hazardous Materials. 262 (2013) 447–55. https://doi.org/10.1016/j.jhazmat.2013.08.063.

[159] T. Tokmakci, A. Ozturk, J. Park, Boron and zirconium co-doped TiO2 powders prepared through mechanical ball milling, Ceramics International. 39 (2013) 5893–5899. https://doi.org/10.1016/j.ceramint.2013.01.009.

[160] S. Singh, R. Sharma, B.M.-A.S. Science, undefined 2017, Enhanced surface area, high Zn interstitial defects and band gap reduction in N-doped ZnO nanosheets coupled with BiVO4 leads to improved photocatalytic, Elsevier. (n.d.). https://www.sciencedirect.com/science/article/pii/S0169433217308711 (accessed November 17, 2022).

[161] J. Li, L. Guo, N. Lei, Q. Song, Z. Liang, Metallic Bi Nanocrystal-Modified Defective BiVO4 Photoanodes with Exposed (040) Facets for Photoelectrochemical Water Splitting, ChemElectroChem. 4 (2017) 2852–2861. https://doi.org/10.1002/CELC.201700680.

[162] J. Lin, X. Han, S. Liu, Y. Lv, X. Li, Y. Zhao, Y. Li, L. Wang, S. Zhu, Nitrogen-doped cobalt-iron oxide cocatalyst boosting photoelectrochemical water splitting of BiVO4 photoanodes, Applied Catalysis B: Environmental. 320 (2023) 121947. https://doi.org/10.1016/j.apcatb.2022.121947.

[163] S.M. Thalluri, C. Martinez Suarez, M. Hussain, S. Hernandez, A. Virga, G. Saracco, N. Russo, Evaluation of the Parameters Affecting the Visible-Light-Induced Photocatalytic Activity of Monoclinic BiVO 4 for Water Oxidation, Industrial & Engineering Chemistry Research. 52 (2013) 17414–17418. https://doi.org/10.1021/ie402930x.

[164] S.S. Kalanur, H. Seo, An experimental and density functional theory studies of Nb-doped BiVO4 photoanodes for enhanced solar water splitting, Journal of Catalysis. 410 (2022) 144–155. https://doi.org/10.1016/j.jcat.2022.04.019.

[165] H. Ullah, A.A. Tahir, T.K. Mallick, Structural and electronic properties of oxygen defective and Se-doped p-type BiVO4(001) thin film for the applications of photocatalysis, Applied Catalysis B: Environmental. 224 (2018) 895–903. https://doi.org/10.1016/j.apcatb.2017.11.034.

[166] S.N.F.M. Nasir, H. Ullah, M. Ebadi, A.A. Tahir, J.S. Sagu, M.A.M. Teridi, New insights into Se/BiVO4 heterostructure for photoelectrochemical water splitting: A combined experimental and DFT study, Journal of Physical Chemistry C. 121 (2017) 6218–6228. https://doi.org/10.1021/ACS.JPCC.7B01149.

[167] Y. Xi, H. Jiang, B. Jin, J. Shi, … T.L.-A.M., undefined 2014, First-principle study on the photocatalystic properties of tungsten doped monoclinic BiVO4 crystallites, Trans Tech Publ. Online (2014) 845–849. https://doi.org/10.4028/www.scientific.net/AMR.873.845.

[168] W.J. Yin, S.H. Wei, M.M. Al-Jassim, J. Turner, Y. Yan, Doping properties of monoclinic BiVO4 studied by first-principles density-functional theory, Physical Review B - Condensed Matter and Materials Physics. 83 (2011). https://doi.org/10.1103/PHYSREVB.83.155102.

[169] R.T. Gao, S. Liu, X. Guo, R. Zhang, J. He, X. Liu, T. Nakajima, X. Zhang, L. Wang, Pt-Induced Defects Curing on BiVO4 Photoanodes for Near-Threshold Charge Separation, Advanced Energy Materials. 11 (2021). https://doi.org/10.1002/AENM.202102384.

[170] X. Gu, Y. Luo, Q. Li, R. Wang, S. Fu, X. Lv, Q. He, Y. Zhang, Q. Yan, X. Xu, F. Ji, Y. Qiu, First-Principle Insight Into the Effects of Oxygen Vacancies on the Electronic, Photocatalytic, and Optical Properties of Monoclinic BiVO4(001), Frontiers in Chemistry. 8 (2020). https://doi.org/10.3389/FCHEM.2020.601983/FULL.